ABSTRACT

Title of Dissertation: FABRICATION AND CHARACTERIZATON OF POLYPYRROLE/GOLD BILAYER MICROACTUATORS FOR BIO-MEMS APPLICATIONS

Yingkai Liu, Ph.D., 2005

Directed By: Professor Elisabeth Smela
Department of Mechanical Engineering

The proof of concept for conjugated polymer bilayer microactuators had been demonstrated prior to this dissertation with numerous devices, and their advantages in biomedical applications had been recognized. The next step for this technology was implementation in real systems, which required knowledge of the main performance metrics and limitations. In this dissertation, work focused on measuring these metrics for the first time to facilitate the development of cell-clinics, which are microsystems for cell study and for cell-based sensing. The conjugated polymer used throughout the dissertation was polypyrrole doped with dodecylbenzenesulfonate, PPy(DBS), and the second layer in the bilayer was gold.

Device fabrication challenges were first identified and addressed, focusing particularly on methods to produce PPy/Au bilayers that did not suffer from delamination. By electroplating Au onto the electrodes or by wet etching them to increase mechanical interlocking, this problem, which had plagued the field for the last decade, was solved. Another important contributor to lifetime, which is a key

actuator metric, is loss of electro-activity with extended cycling. This metric was quantified through measurements of the total exchanged charge of PPy(DBS) with cycles of electromechanical redox. This result impacts how these actuators can be used.

Two other key metrics on which this work focused were bending angle, analogous to stroke in a linear actuator, and force. It was necessary to determine bending angle as a function of film thickness experimentally because the traditional bilayer beam models could not account for microfabricated bilayer radius of curvature data. Through experimental testing over a wide range of PPy and Au thicknesses, the relationship between PPy:Au thickness ratio and curvature was mapped out. The experimental results demonstrated the existence of strain gradients within the conjugated polymer films, with the material at the surface having greater actuation strain than that at the gold interface. Finally, accurate force measurements had not been done prior to this dissertation research because of the significant challenges involved in developing a method for measuring force in microactuators. This dissertation described the development of such a methodology and provides data for the blocked force as a function of polypyrrole thickness.

FABRICATION AND CHARACTERIZATON OF POLYPYRROLE/GOLD BILAYER MICROACTUATORS FOR BIO-MEMS APPLICATIONS

By

Yingkai Liu

Dissertation submitted to the Faculty of the Graduate School of the
University of Maryland, College Park, in partial fulfillment
of the requirements for the degree of
Doctor of Philosophy
2005

Advisory Committee:

Professor Elisabeth Smela, Chair
Professor Amr Baz
Professor Hugh Bruck
Professor John Melngailis
Professor Benjamin Shapiro

Dedication

This dissertation is dedicated to my grandmother (my mother's mother), *Laolao* in Chinese pronunciation. She raised me up with all of her love. After I came to U.S.A in 1999, she became very sick, mostly because of missing me. On June 16, 2000, she passed away. Due to poorness of her family, she did not have a chance to go to school during her childhood. However, she taught me how to be a man, a man who is nice to the other people, who loves and takes care of the other people more than love and take care of himself. She taught me the most precious lessons in my life.

"You raise me up, so I can stand on mountains." Dear *laolao*, if the heaven exists, you must be there at this moment, smiling and looking at your little grandson.

Acknowledgements

First of all, I give my special thanks to my advisor, Prof. Elisabeth Smela, for her four years' instruction and guidance during my Ph.D. study. She not only taught me the knowledge and capabilities of doing projects, but also trained me to be an independent researcher. I also thank her for providing me a better and better experimental environment.

I feel very grateful to all my groupmates, Dr. Christophersen, Dr. Jian, X. Wang, M. Urdaneta, L. Oh, S. Fanning, S. Moseley, R. Delille, M. Dandin, N. Reeves, A. Daiub, Q. Gan, S. Baig, M. Duerkop, and P. Chin. All of you helped me on experiments and discussed research with me, shared my joy and happiness, and encouraged me when I felt depressed.

I also want to thank Prof. Abshire and her group for the collaboration on the cell-clinics project, Prof. Shapiro and his group for the collaboration on the bending characterization project, T. Loughran and N. Ballew for helping in the cleanroom, T. Maugel for SEM, and S. Li for patterning SU8.

Finally, I wish to give special thanks to my wife Yue Wang, my family, and all my friends for their love and support during the long-time study.

Table of Contents

List of Tables

List of Figures

Chapter 1 Dissertation Goals and Overview

Polypyrrole (PPy) is a conjugated polymer that undergoes a volume change when its doping level is varied through the application of a voltage (see section 2.1). Bilayer microactuators of PPy and gold were first developed to exploit this phenomenon in the early 1990s [1, 2]. In recent years, commercialization efforts have begun and there is increased interest in these devices for biomedical applications [3] because they work in biofluids, are biocompatible, and require only small voltages to actuate (see section 2.2). However, when the research in this dissertation was begun, there were significant challenges standing in the way of implementing the technology, with failure due to delamination and unpredictable lifetime, curvature, and force being the most critical. As a result of the work presented here, which identifies a fabrication process that ensures reproducible actuation and which characterizes the performance, our understanding of these actuators has reached the stage where designers can incorporate them into their own microsystems.

The dissertation begins with an introduction to conjugated polymers, their use as actuators, and the prior work in the field (section 2.2). The motivation for further developing the actuator-based microsystem, cell-clinics, is then reviewed (section 2.3), followed by a discussion of the role of the bilayer actuators in the cell clinics (section

2.4). The chapter ends with a general discussion of actuator metrics, with an identification of the key metrics for these particular actuators (section 2.5) to set the stage for the work on developing a more fundamental understanding of the device performance.

The purpose of the research in this dissertation was to build on prior work to take it beyond proof-of-concept to a solid foundation. My contributions begin in Chapter 3 with development of a process sequence to fabricate bilayer microactuators and microstructures on CMOS chips. The primary difficulties of handling the chips during microfabrication were solved, and a lid rotated by a bilayer hinge was fabricated on the chip. At the same time, problems were encountered, which therefore motivated the work in Chapters 4-6.

Chapter 4 focuses on preventing PPy delamination from the Au electrode. Without mechanical integrity, these bilayers would never be more than curiosities. Surfaces were developed that effectively interlock the two layers, as determined by tape testing PPy films on Au-coated substrates during extended cycling. This chapter also includes measurement of the electrochemical degradation of the PPy, which fundamentally limits device lifetime in aqueous solutions. The quantification of the loss of electro-activity with cycle number is needed for determining the biomedical applications for which the actuators are and are not appropriate.

Chapter 5 describes bending angle studies, starting with a description of the experimental methods, continuing with the results, and concluding with some simple modeling. Prior work had shown that simple bilayer models did not account for microactuator bending results, because, it was postulated, of either actuation strain gradients or Young’s modulus gradients in the film. It was therefore necessary to determine bending angle as a function of film thickness experimentally, and from these data to back out the gradients.

Chapter 6 follows the same pattern for force studies. These experiments were particularly challenging because the microsystem had to be mechanically interfaced to a macro-system, and a new experimental methodology had to be developed.

Additional original research contributions indirectly related to these topics are included in the appendices. Appendix A and Appendix C describe PPy deposition and device fabrication challenges that were identified together with their solutions. Appendix D is a description of actuators fabricated on a Kapton substrate, which may one day lead to “micro-origami”.

Chapter 2 Introduction and Background

2.1 Conjugated Polymers

Conjugated polymers are characterized by alternating single and double bonds along the polymer backbone. Polypyrrole (PPy) is one of the most stable conjugated polymers (Figure 1) [4]. Conjugated polymers are organic semiconductors. When the polymer is oxidized, electrons are removed; delocalized positive charges appear on the backbone. As a result, the polymer becomes electrically conducting, or doped [5]. The conductivity of doped PPy is typically in the range of 10-100 $(\Omega\cdot\text{cm})^{-1}$ [6]. (The conductivity of copper is 6×10^5 $(\Omega\cdot\text{cm})^{-1}$; p-doped Si with $10^{17}/\text{cm}^3$ aluminum is about 80 $(\Omega\cdot\text{cm})^{-1}$ [7].) In order to maintain charge neutrality, anions (negatively charged ions, A^-) enter the polymer from the electrolyte (Figure 2). Since the doping results from the electrochemical oxidation and the charges are positive, the polymer is p-doped; the anions are called dopants. The doping level is controlled by the oxidation level.

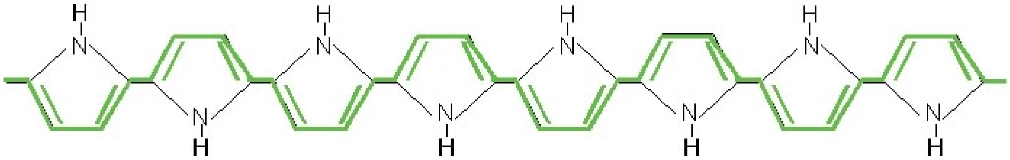

Figure 1. Schematic of PPy molecular structures. Alternating single and double bonds are along the polymer backbone. (Courtesy of Smela.)

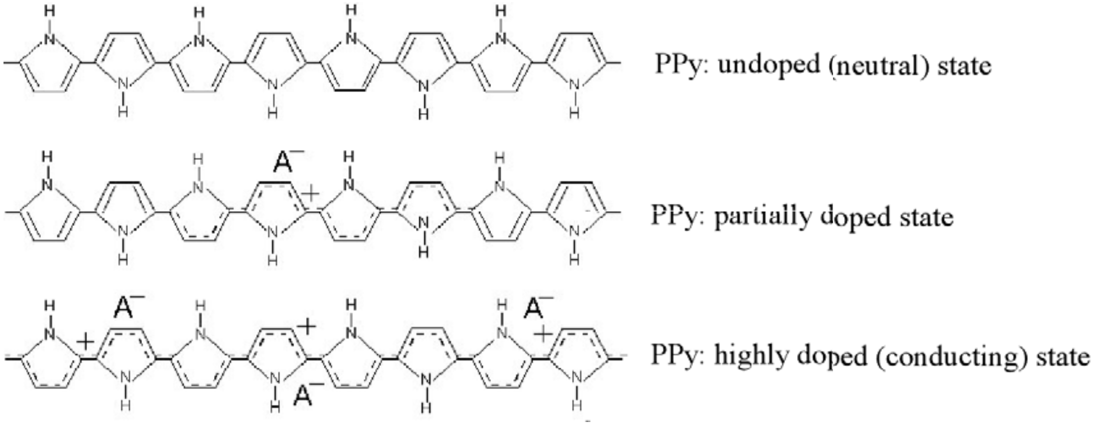

Figure 2. Schematic of doping PPy. Electrons are removed from the PPy backbone by an applied voltage, which oxidizes the polymer. In order to maintain charge neutrality, anions A^- enter the polymer from the surrounding solution (electrolyte). (Courtesy of Smela.)

2.2 Introduction to Polypyrrole Bilayer Actuators

2.2.1 Deposition of PPy

Polypyrrole (PPy) is electrochemically deposited from an aqueous electrolyte containing the pyrrole monomer. The deposition mechanism is briefly described here; see [8] for further details. When a sufficiently positive potential is applied to the electrolyte, the monomers at the working electrode surface are oxidized and become reactive radical cations. When two radical cations meet, they react to form a dimer. As more pyrroles are add to the growing chain, the oxidation potential of the oligomer drops, allowing polymerization at slightly lower potentials, and at some point, depending on the solvent, the oligomer becomes insoluble and precipitates onto the working electrode. The PPy continues to grow on the electrode by addition of monomers and oligomers from solution. The monomers polymerize primarily at the positions adjacent to the nitrogen (as shown in Figure 1), but the other two positions are also reactive, and reactions at these sites produce crosslinking (and electronic defects). To maintain overall charge neutrality, one anion for every positive charge is incorporated during deposition [9]. Our group use dodecylbenzenesulfonate (DBS^-) as the anion [1, 2, 10]. Since DBS^- anions are large, once they are incorporated into the film it is essentially impossible for them to leave during later actuation [11].

The deposition procedure is briefly introduced here; see Appendix A for details. Deposition of PPy was performed in an electrochemical cell with three electrodes connected to a potentiostat, as shown in Figure 3. All three electrodes were immersed in a solution containing pyrrole and NaDBS. An Au-coated silicon substrate was connected to the working electrode (WE) lead. PPy was deposited on the Au. The reference electrode (RE) was Ag/AgCl. A reversible redox reaction (equation 1) takes place and reaches equilibrium at the RE. Thus, no current flows through the RE. This reaction provides a reference potential (0 V) [12]. All electrochemical potentials given in this dissertation are voltages applied between the WE and the RE (i.e. vs. Ag/AgCl). The counter electrode (CE) was either a piece of platinum foil, an Au-covered silicon substrate, or a piece of graphite. The CE should be much larger than the WE to ensure that the reactions on the CE do not limit the speed of the reactions at the WE [10]. The

WE, the aqueous NaDBS solution, the CE, and the potentiostat comprise a complete current loop.

$$(1) \qquad \mathbf{AgCl(s) + e \leftrightarrow Ag(s) + Cl^{-}\ (aq)}$$

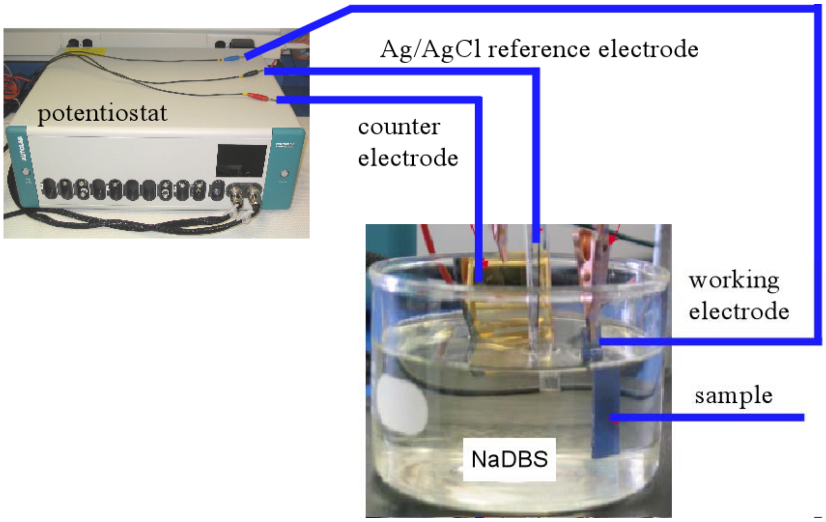

Figure 3. An experimental setup to electrodeposit PPy(DBS). The deposition was powered and controlled with a potentiostat. An Au-coated silicon substrate was the working electrode onto which PPy(DBS) was deposited. The reference electrode was Ag/AgCl. The counter electrode was another, larger Au-coated silicon substrate.

2.2.2 Actuation of PPy

The experimental configuration shown in Figure 3 was also used to actuate the PPy; the aqueous electrolyte was NaDBS. When a sufficiently negative electrochemical potential is applied (for PPy(DBS) in NaDBS, –1 V vs. Ag/AgCl), PPy is reduced, meaning that electrons are added to the polymer. When the polymer is completely reduced, the net positive charge on the backbone is completely neutralized. In order to maintain charge neutrality, cations in the solution, Na^+ in all experiments described in this dissertation, enter the PPy [13]. This results in a volume expansion [14, 15]. The cations are surrounded by water molecules, which increases the actuation strain [16].

When the voltage is increased from –1 to 0 V vs. Ag/AgCl, PPy is oxidized again. This reaction is completely reversible, but competes with degradation reactions, as will be described in Chapter 4 . Because the DBS^- anions are immobile [11], the Na^+ cations are expelled and PPy volume contracts.

In summary, the reduction/oxidation (redox) reaction in PPy is:

$$\mathbf{PPy^+(DBS^-) + Na^+ + e^- \leftrightarrow PPy^0(NaDBS)} \qquad \mathbf{(2)}$$

PPy is reduced when the reaction goes from the left to the right side, and oxidized from the right to the left side. The in-plane strain of PPy(DBS) was reported ranging from 0.35% [17] to 2% [18].

In general, when the anions are mobile, such as chloride (Cl^-) [11] or perchlorate (ClO_4^-) [19-21], they are expelled upon reduction and the volume of the PPy decreases. If the anions are medium-sized, such as p-toluene sulfonate (pTS) [22], they move with difficulty through the PPy. Therefore, the total volume expansion is lowered due to the opposite ion transport [23]. Moreover, a “twitching” behavior has been observed under these conditions instead of the desired smooth actuation [11]. Since PPy doped with large anions has better chemical stability [23] than PPy doped with small anions, as well as high strain and smooth movement, we use PPy(DBS) in our group.

Voltage-current curves called cyclic voltammograms (CVs) are used to characterize PPy during electrochemical oxidation and reduction (redox). CVs are carried out by applying triangular voltage ramps (Figure 4) and monitoring the current. There are two current peaks in Figure 5a. The one at -0.35 V is due to oxidation, and the one at -0.67 V to reduction. The shape of the CVs changes with scan rate [24] and in electrolytes with different pH or ions [25, 26]. These features help researchers to understand the redox mechanism [27, 28].

The reason that the current does not go to zero when the voltage reaches zero has been the subject of much discussion in the literature, and is still controversial. Feldberg proposed that the current is capactive and that the PPy acts as a porous electrode [29]. If the polymer is porous, the polymer/electrolyte interface is large, and a change in the double layer at the interface generates a large capacitive current.

Figure 5b shows 5 sequential scans. The currents stabilize after a few scans, and the curves start to trace over each other. (The polymer does not “charge up” with cycling: the oxidation charge is balanced by the reduction charge except for that drawn due to irreversible parasitic reactions such as hydrolysis.)

Integrating the current gives the total charge exchanged during redox switching. If the

PPy loses electroactivity, the current decreases. Thus, CVs were used to characterize PPy degradation in this dissertation (see section 4.6).

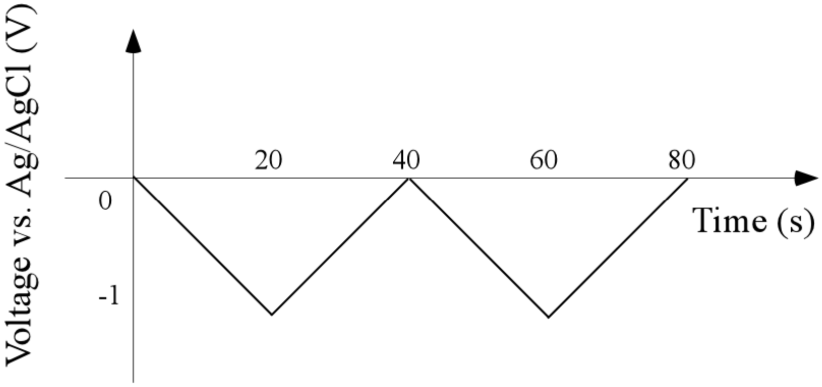

Figure 4. A voltage cycle between 0 and –1 V vs. Ag/AgCl is applied to actuate PPy/Au bilayers.

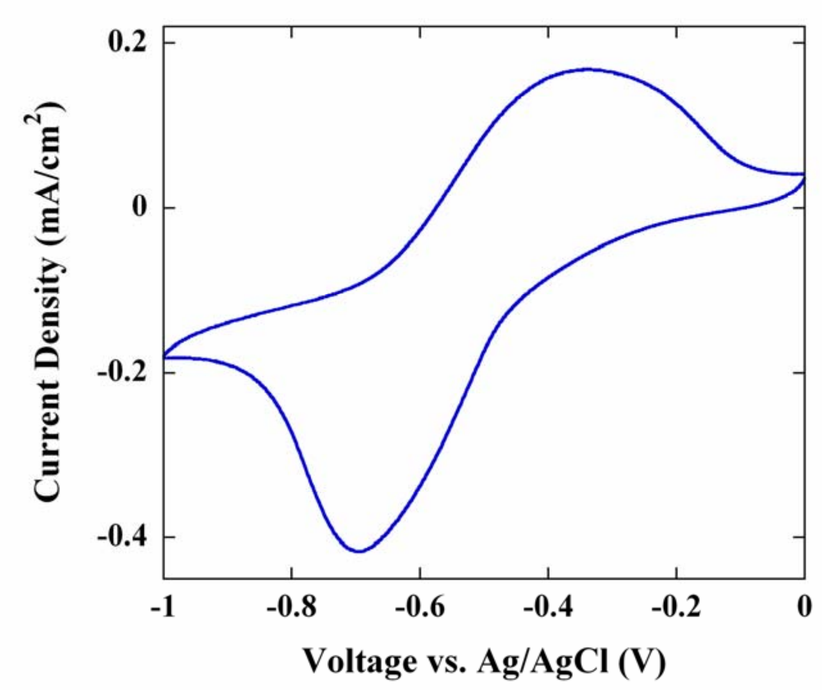

a) CV of a 3000 Å thick PPy film scanned at 50 mV/sec. The oxidation peak is at –0.35 V and the reduction peak at –0.7 V.

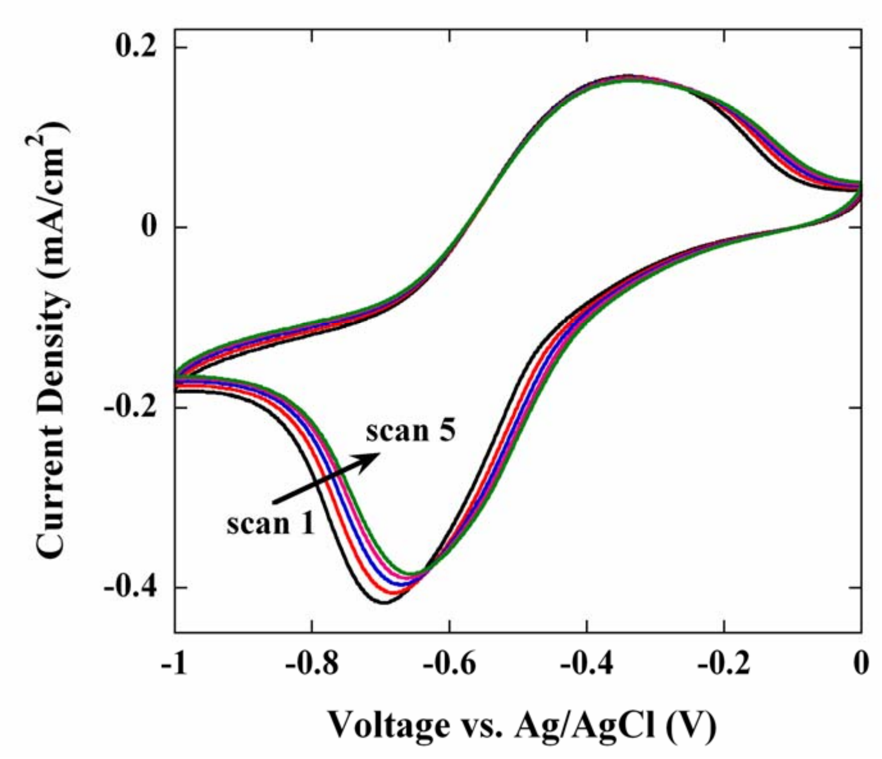

b) CVs of five continuous scannings. The current at 0 V becomes stable after a few scans, which shows PPy is not "charged up".

Figure 5. CV at 50 mV/sec of a 3000 Å thick PPy film scanned in 0.1 M NaDBS solution.

2.2.3 PPy/Au Bilayer Actuators

Based on the electrically controllable volume change, PPy actuators have been developed in the forms of hollow tubes [30], helix tubes [31], zigzag wires [32], and flat films [33]. The tubes moved in its axial direction [30, 31]. The zigzag wires of Au or Ti formed a framework onto which PPy was deposited; the resulting film actuated like an accordion [32]. The flat-film actuator took advantage of the out-of-plane volume change of PPy; a controllable valve was designed and tested [33]. The common feature of these actuators is that they moved along one direction (one-dimensional actuation).

Another configuration is the polymer/metal bilayer (Figure 6) that converts in-plane strain into bending, which realizes two-dimensional actuation. PPy/Au bilayer actuators have been developed since the early 1990s [20, 34-37]. In 1992, Otero [20] and Pei [37] both independently demonstrated macro-scale actuators, e.g. 3 cm × 1 cm × 15 μm (L × W × T) [20]. The mechanism of bending is illustrated in Figure 6. During electrochemical redox, PPy changes volume. Since the Au layer does not change volume, the bilayer bends. The Au serves not only this mechanical function, but also as the electrode to the polymer.

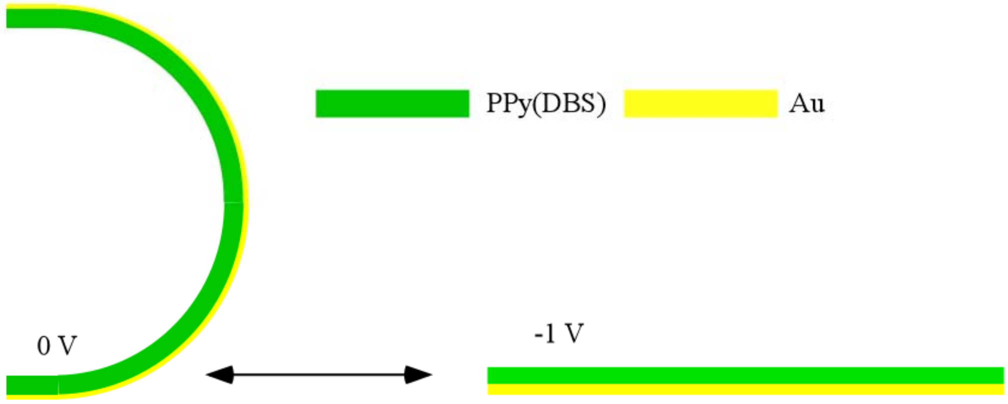

Figure 6. Schematic of PPy(DBS)/Au bilayer bending. At 0 V, PPy is oxidized; its volume contracts. Because Au does not change volume, the bilayer bends. At -1 V, PPy is reduced, which causes a volume expansion. As a result, the bilayer returns to the flat state. (Courtesy of Smela.)

Free-standing PPy films [38, 39] and triple layers [40-42] were also demonstrated as actuators. The former bent when a tissue soaked with water or organic molecules was placed close to the polymer. The actuation was due to the differential absorption of molecules on both sides of the PPy film [38]. Otero's group developed triple-layer actuators with tactile sensitivity [42]. Such an actuator is composed of a non-conducting, flexible tape with PPy films glued on both sides. The current flows between the two layers of PPy films so that when one layer is oxidized to expand, the other is reduced to contract. As a result, the triple-layer beam bends.

Smela et al. reported a MEMS process to fabricate bilayer microactuators in 1993 [1]. A box of 30 × 30 μm^2 folded using bilayer hinges was demonstrated [2]. The principal mechanism of these devices is that the bilayer bends out of plane and rotates a connected rigid plate (Figure 7). The importance of Smela's approach is that it opened a door to the development of PPy-based microsystems, especially in the field of biomedical applications where PPy is advantageous over other actuator materials [3]; see section 2.4.2 for an example. Since then, a microrobot for cell handling [43, 44], cell-clinics for cell study and cell-based sensing [45-47], microvalves for treating urinary incontinence [48], a cell isolator [49], and microvalves for drug delivery system [50] have been developed by our and other groups.

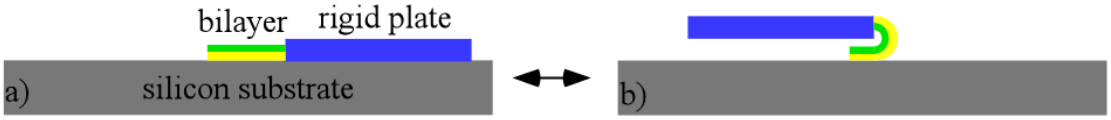

Figure 7. Schematic of a bilayer microactuator. a) The bilayer was fabricated on top of a silicon substrate. A rigid plate was connected to the bilayer. b) When voltages were applied, PPy changed volume; the bilayer bent to actuate the rigid plate. (Courtesy of Smela.)

2.3 Motivation for Dissertation Research from Potential Applications

The proof of concept for conjugated polymer bilayer microactuators had been demonstrated according to the review and discussion above. The next step for this technology is implementation in real systems. The bilayer actuation studies described in this dissertation were part of a larger effort to develop a new chip-based technology to monitor cells over the long term for applications ranging from cell-based sensors to the study of basic cell biology. This research effort, dubbed “cell-clinics,” combines MEMS with CMOS to create microenvironments for culturing cells while measuring various parameters, including voltage, capacitance, and fluorescence (Figure 8).

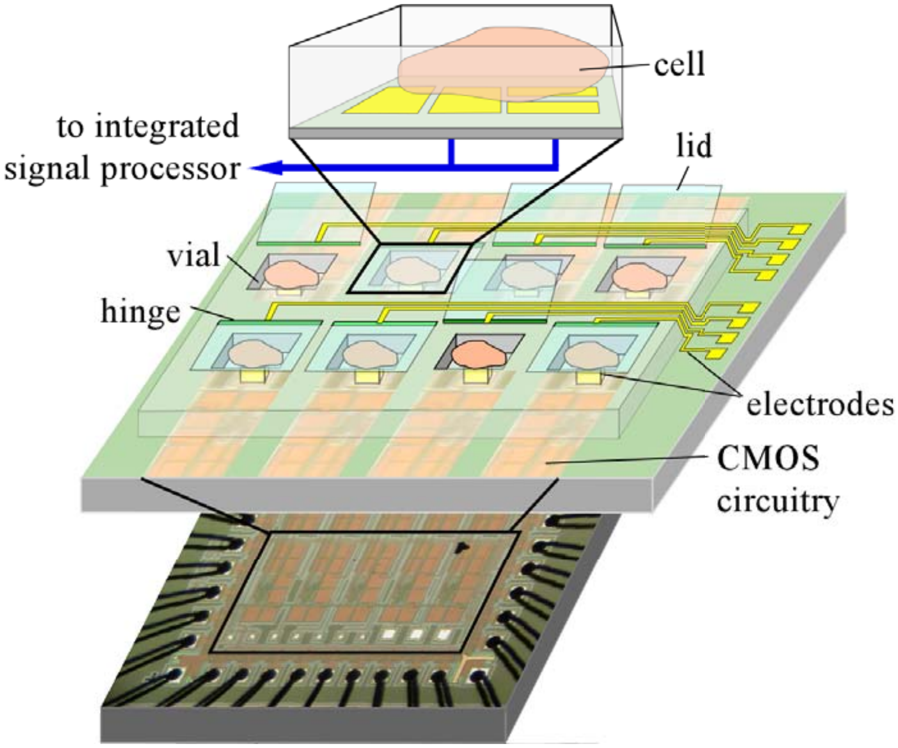

Figure 8. Conceptual illustration of cell-clinics under development, showing MEMS vials for holding cells and underlying CMOS circuitry. (Courtesy of Abshire and Smela.)

2.3.1 Overview of Cell-Clinics Research Effort

Since cells are the fundamental units of living things, there is a growing interest in studying cells with microsystems [51, 52], whose feature sizes are comparable with those of cells, which is helpful in creating an in-vivo-like environment [52, 53]. Since 2002, a team comprising Prof. Abshire (ECE) and her students, focusing on CMOS sensing and circuitry, and Prof. Smela and her group, focusing on MEMS, has been working on the cell-clinics. The MEMS structures are designed to form an in-vivo-like environment for containing single cells or small groups of cells. The sensors will record electrical, optical, and chemical signals generated by cells. Furthermore, the project goals are to use olfactory neural cells as sensing elements to transduce chemical stimuli to electrical outputs. This microsystem (Figure 9) will also benefit studies of basic properties and activities of cells, such as cell life cycle, as well as the development of drug screening and environmental monitoring systems.

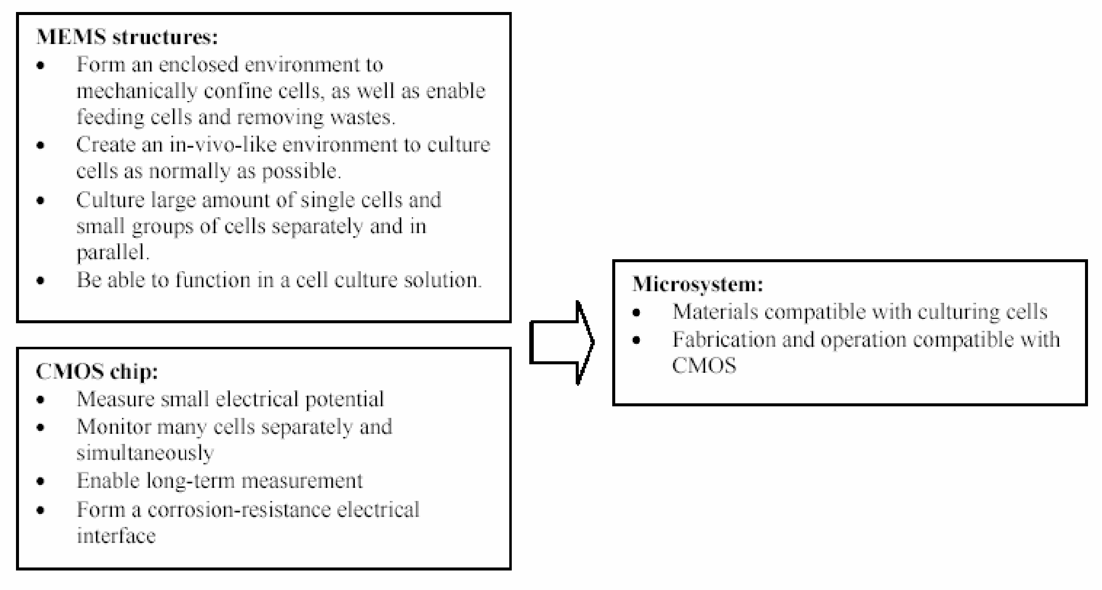

MEMS structures:

- Form an enclosed environment to mechanically confine cells, as well as enable feeding cells and removing wastes.
- Create an in-vivo-like environment to culture cells as normally as possible.
- Culture large amount of single cells and small groups of cells separately and in parallel.
- Be able to function in a cell culture solution.

CMOS chip:

- Measure small electrical potential
- Monitor many cells separately and simultaneously
- Enable long-term measurement
- Form a corrosion-resistance electrical interface

Microsystem:

- Materials compatible with culturing cells
- Fabrication and operation compatible with CMOS

Figure 9. Summary of cell-clinics design in terms of MEMS structures, CMOS chip, and the microsystem.

Cell-clinics are an example of lab-on-a-chip technology (or micro-total-analysis systems, μTAS). The μTAS concept was first proposed by Manz et al. in 1990 [54]. In order to continuously monitor the concentration of reagents, they proposed to minimize and integrate existing sample pretreatment, separation, and sensing mechanisms to form a microsystem [55]. Their theoretical analysis showed that such a microsystem would benefit analytical work in terms of sensitivity, sensor lifetime, speed, and cost [55]. Since then, μTAS has become a more and more popular and interdisciplinary research field. An international conference (MicroTAS) has been hosted eight times since 1994, and the journal *Lab on a Chip* was launched in 2001.

Compared to traditional apparatus, µTAS for cell study are advantageous for creating an in-vivo-like environment [52]. In vivo, cells are close-packed with each other and with the extracellular matrix [52]. Because the feature size of MEMS structures is comparable with the size of cells, i.e. from 10 to 100 µm, such a closely packed environment can be easily formed in µTAS. Cells cultured in traditional dishes have to comply with the two-dimensional rigid surface [56], whereas a three-dimensional environment can be formed by MEMS technologies. The three-dimension environment can mimic the extracellular matrix in which a cell community exists [57]. By studying single and/or small groups of cells, rather than the average of large number of cells or cell communities, researchers can investigate properties and variations among single cells, as well as understand how single cells communicate with each other to work together as a group [58]. As a result physiological studies of specific mechanisms and statistical studies of cell properties will be enabled, as well as studies of cell performance within a cell community. For a review of µTAS systems, please refer to Appendix B.

Although microsystems for cell study have attracted a lot of interests from µTAS researchers, there are few reports on integrating MEMS, in particular micromachined in-vivo-like environments for culturing cells, with CMOS to enable in-situ, real-time monitoring single and small groups of cells. Our cell-clinics microsystem is being developed toward this direction.

2.3.2 Motivation for Integrating MEMS and CMOS

Integrating CMOS and MEMS technology will not only facilitate fundamental studies of cells, but also create new approaches to problems that are difficult or even impossible to solve by using conventional methods. For example, electronic noses are required to be sensitive, selective, and reversible [59]. Currently, an electronic nose is a system composed of arrays of sensor [60]. Each sensor interacts with a specific odor; signals from various sensors are combined and processed to identify a smell (a mixture of odors) [61]. The difficulty lies that the odors may interfere with each other, which results in a false sensing signal [62]. Human being can solve this problem based on experiences [62]. But it is a challenge to “train” electronic noses to learn and accumulate experiences [62]. In contrast, if olfactory cells can be cultured directly in a sensing system to form a cell-based electronic nose, the problem will be bypassed.

One of the future goals of our cell-clinics is to develop a cell-based olfactory sensing system. In the envisioned system, olfactory neurons are cultured in the in-vivo-like MEMS structures (vials). Signals from neurons corresponding to various smells are recorded and processed by sensing electrodes that locate in the same vial with the neurons. As a result, a library of smells vs. signals is created. When the cell-based electronic nose is used in practice, a target smell is recognized by comparing the collected signals with respect to the signals stored in the library. As the living transducer component, the neuron enables a highly sensitive, selective, and reversible detection [62]. The powerful CMOS technology enables real-time, automatic collecting, storing, processing, and transporting data for long-term monitoring.

In general, the advantages of integrating MEMS and CMOS include (1) the usage of the microsystem will be easy and automatic, which is beneficial to possible applications of home health-care, (2) the final product can be miniaturized for portable usage; furthermore, an implantable system can be created. In addition, various sensors such as temperature [63], pH [64], fluorescence [65], position [66], and electrical properties [67] can be fabricated in or around microstructures by using the CMOS technology. The microsystem can be customized depending on the users' requirements: future users are able to designate a specific sensor to a specific unit of cell-holding microstructures, and obtain various signals from multiple units in the microsystem at the same time. In summary, the combination of MEMS and CMOS makes μTAS flexible and powerful to be used in a broad field.

2.4 Function of Bilayers in Cell-Clinics

Because cells such as neurons are mobile [68], they have to be encaged to enable long-term measurement. Optical tweezers [69] and dielectrophoresis [70] are well established to trap cells suspended in liquid. Many animal and human cells, however, must adhere to a solid surface before they can grow and reproduce [71-73]. Therefore, mechanical structures are employed in the cell-clinics to encage the cells (Figure 10a). An important concern of the mechanical structure design is the microenvironment. Walker et al. cultured cells in micro-channels [74]. Fluid flowed through the channels to supply nutrients and remove wastes; but the flow applied a shear stress on the cells [52] that affected their normal life. In our microsystem, cells will be cultured in vials with movable lids to avoid this problem. On-chip microactuators are employed to open vials for feeding cells and removing wastes. The vials and lids are made of insulating material SU8. When one vial is closed, signals from cells in that vial will be measured; signals from cells in other vials will be blocked by the closed structures. In order to measure many cells independently and simultaneously, arrays of vials are formed on the chip (Figure 10b).

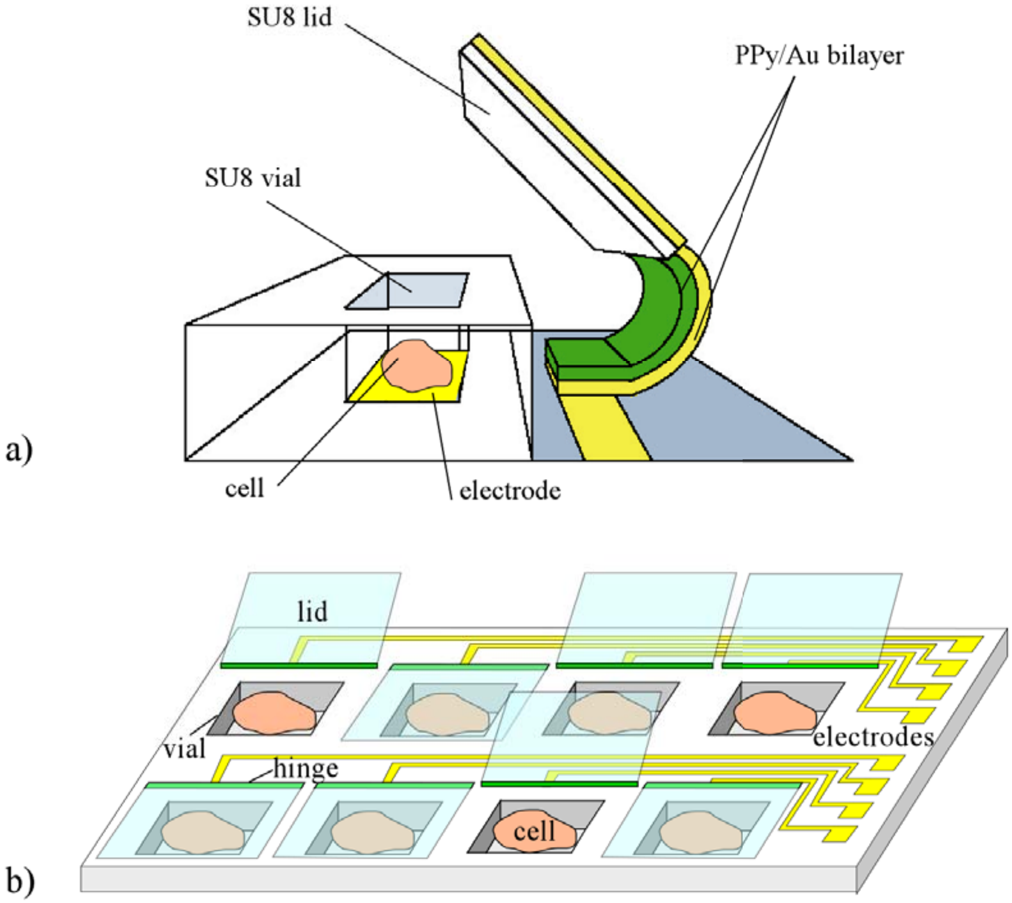

Figure 10. Schematic of the cell-clinics. a) A "lab" is composed of a vial and a movable lid actuated by PPy/Au bilayer to hold single or small group of cells. In the vial, the cell is monitored by an electrode. b) Arrays of labs are placed on one substrate to measure many cells independently and simultaneously. (Courtesy of Smela.)

2.4.1 Requirements for On-Chip Microactuators

In the cell-clinics, the on-chip microactuator is a core component to confine cells over the sensors and to facilitate measurement by electrically isolating the cells. It has to satisfy several requirements.

1. The actuator must operate in a cell culture medium (a salt solution).

2. The materials composing the actuator must be compatible with cells and the cell-culturing environment. The materials must not be toxic to cells, nor corrode and lose function in the cell culture medium.

3. The actuator must implement "two-way" movements.

    - During culturing and measuring the cells, the actuator must continuously keep the lids closed so that the cells are kept in place and electrically isolated from the cells in other vials. The duration is at least a cell cycle, which is typically 24 hours [71, 75].

    - In order to maintain a suitable environment for cell living, the actuator must open the lids for changing the culture medium daily or weekly depending on the type of cells [76]. Currently, the medium changing is conducted manually by using a syringe or a pipette at the Bioprocess Scale-Up Facility, UMCP. During the operation, the actuator needs to keep the lids open, holding at least one minute based on our experience.

4. The fabrication and operation of the actuator must be compatible with the CMOS circuitry and cells. For example, if the actuator is electrically driven, the operation voltage must be smaller than the CMOS breakdown voltage (the

voltage to make the insulator conductive). Depending on the fabrication process, the breakdown voltage is typically 10-20 V [77]. If the actuator is thermally driven, the working temperature cannot be higher than the incubation temperature of cells. To most human and warm-blooded animal cells, the recommended temperature is 37±0.5 °C. The cells will die quickly when it is higher than 40 °C [78].

2.4.2 Microactuator Review and Evaluation

Most of the broadly used actuators in the MEMS field are electrically driven. (1) Electrostatic actuators, such as comb-drive actuators, have been developed based on the attractive force between interdigitated electrodes when a driving voltage is applied (see for example [79]). Typical driving voltages were from 10 to 40 V for a 1.5 - 2.5 μm electrode gap [80], which is higher than the CMOS breakdown voltage. (2) Piezoelectric actuators, in which an external electrical field polarizes and generates a stress, have also been developed (see for example [81]). Piezoelectric actuators require even higher driving voltages, typically more than 100 V [82]. (3) Electro thermal actuators and shape memory alloy (SMA) actuators operate when heated. Because the composed materials are conductive (e.g. polysilicon for thermal actuators [83] and Ni-Ti alloy for SMA actuators [84]), they only require small voltages (< 12 V for thermal actuators [83, 85]) or currents (80 mA for shape memory alloy actuators [86]). In an aqueous environment, however, heat loss will result in small displacements [87, 88]. (4) Electromagnetic microactuators exert large deflections and operate under small currents (<100 mA)

[Fullin, 1998 #268; [89]. An example was a nickel-coated polysilicon (430 μm × 130 μm × 15 μm) plate with one end anchored to a substrate by torsion-beams. The plate was rotated 90° out of the substrate by an external magnetic field [90]. The difficulty of using the actuators in our application is the formation of the rotating structures like the polysilicon torsion-beams. The fabrication process included high-temperature LPCVD deposition (605 °C) and annealing (1000 °C) [89], which would damage CMOS circuitry. There has not reported fabricating the structures by using other materials and methods.

In addition to the conventional actuators, hydrogel actuators have been developed based on a phase transition undergone in the polymer network [91]. Hydrogel actuators operated under a variety of stimuli, such as electrical field [92], light [93], and temperature [94]. In particular, they responded to pH [95], glucose [96], and antigen [97], which enable them for biomedical applications [98]. Hydrogels responding to pH change are most commonly studied [99-101]. They generated volume changes due to significant pH change of 2 - 4 [100-103]. However, cells grow well in an environment with stable physicochemical properties, such as pH 7.4 ± 0.4 [104]. Another disadvantage of hydrogel actuator is the lifetime: it stopped actuating after only a few cycles [103].

Alternately, polypyrrole (PPy)/gold (Au) bilayer actuators have advantages over the other techniques in this application. PPy is a biocompatible material [3]. PPy undergoes reversible volume changes under electrochemical stimulation when immersed in an electrolyte [5, 105]. The Au layer serves not only as the electrode to transport simulation signals, but also to convert the volume change in PPy to a bending motion [2]. The actuation voltages are small, between 0 and -1 V [10], which is compatible with CMOS. In summary, PPy/Au bilayer microactuators satisfied all the requirements for the cell-clinics.

2.5 Dissertation Motivation

A process to fabricate MEMS structures on a CMOS sensing chip (1.5×1.5 mm^2) has been developed; see section 3.2 for details. During testing of bilayer actuation, however, the bilayers stopped bending after from a few cycles to one hundred cycles. The failure causes were reported before as 1) PPy delamination from the Au surface [2, 33, 106-108] and 2) loss of PPy electroactivity (degradation) [104-108]. PPy degrades in aqueous solutions because H_2O and O_2 in the electrolyte attack the N on the polymer [109, 110]. A promising solution for some applications is to use ionic liquids, which are electrolytes without water [111-113]. However, for bioMEMS applications the devices must be used in water, so PPy degradation actually determines the lifetime of the devices. It is thus necessary to quantify the degradation so as to characterize the lifetime, which had not been done before. The former problem, PPy delamination, has troubled the community for a long time. PPy delamination deteriorates the bending performance by resulting in smaller bending angle and force, and even causing a sudden device failure. This problem is dangerous when the bilayer-based device/system is implantable, such as the bio-fluidic microvalve [48, 50]. Solving the delamination problem by using methods compatible with current fabrication processes will not only improve the performance of cell-clinics, but it will also remove the most difficult problem in fabrication that the community faces. This part of work and results will be shown in Chapter 4

In the cell-clinics, the bilayer bending performance determines whether the microsystem can work at all. The bilayers must be able to rotate at least 90° to open the cell-holding vials, and rotate 180° to close the vials (Figure 11). In order to encage and isolate cells for measurement, the bilayers must rotate the lids so that they can lie flat on the vial surface and fully cover the vials. To close properly, the diameter of the bent bilayer should equal the sum of the height of the vial and the thickness of the lid. Hence, the diameter determines the thickness of the vial and the lid, and furthermore the material and fabrication parameters (see Appendix E for details) to be employed. The diameter also affects the design of the microstructures, e.g. determines positions of the vial and the bilayer (Figure 12). In addition, the closed lids might be not tight enough for electrical isolation of vials. Other techniques, such as using a magnetic force, are required to facilitate sealing the vials. In this case, the PPy/Au microactuators need to exert enough force to open the vials. Therefore, the PPy/Au bilayers need to be characterized in terms of the bending curvature and bending force.

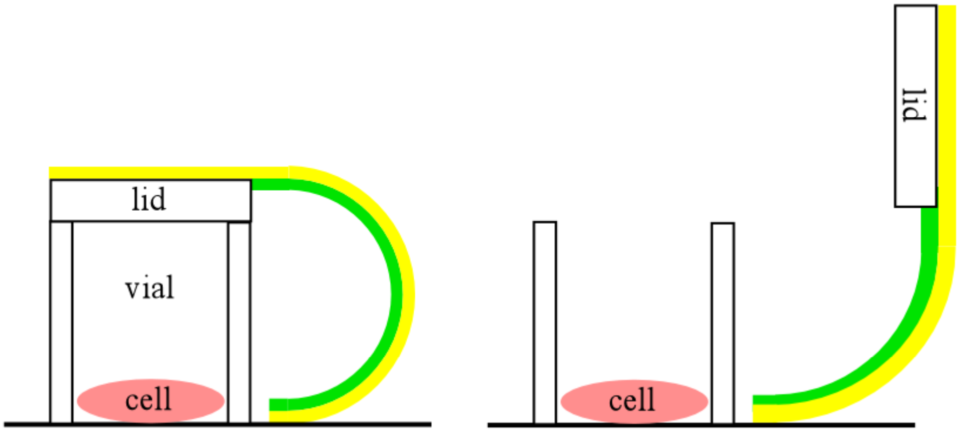

Figure 11. PPy/Au bilayers are required to a) close the cell-holding vials for measuring and b) open the vials for feeding cells and removing waste. In order to fulfill this task, the PPy/Au bilayers have to bend 180° for closing and at least 90° for opening vials.

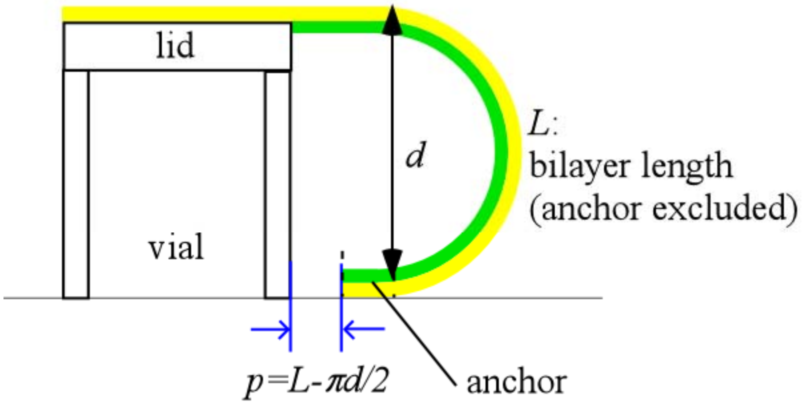

Figure 12. The distance between the bilayer anchor and the cell-holding vial, *p*, is related to the bilayer length *L* and bending diameter *d*, which implies the bending behavior of the bilayers determines the design of the microstructures.

The bilayer bending performance is determined by both bilayer geometric parameters (dimensions, configurations, and layer thicknesses) and component layer mechanical properties. Unfortunately, systematic characterization of the bending performance has only been done on macroactuators [11, 19, 30, 34, 37, 40, 42, 114-119]. On the other hand, existing models [120] fail to predict the correct behavior of microactuators, in part because PPy is a “living” material, its properties vary with the doping state, thickness, and the microfabrication process [18, 23, 121]. Therefore, experimental data are required to characterize the bending performance of the PPy/Au bilayer microactuators. Results of bending curvature characterization will be shown in Chapter 5 , and force in Chapter 6

In summary, the primary purpose of this dissertation was to determine metrics for the PPy/Au bilayer microactuators. Actuator metrics include stress, strain, Young’s modulus, strain rate, speed, operation frequency, efficiency, specific work, specific power, lifetime, etc. [114, 122, 123]. According to the target functions of the cell-clinics, as well as the other devices and systems that have existed and are emerging, the key metrics are identified as follows. 1) Strain. Strain determines the bending curvature of bilayers. Knowing the curvature and the geometry of the bilayers, a designer is aware of their complete moving behavior (e.g. bending angle and path). The curvature was measured directly in this dissertation, and then strain was calculated. 2) Stress. Stress results from strain of PPy during electrochemical redox. When the bending is blocked or restrained, bilayers show a force or moment, which quantifies the extent that micro-scale bilayers interface to the macro-scale world. Therefore, the force or moment is more meaningful than stress for applications. Blocked force was measured in this dissertation. 3) Lifetime. The definition of lifetime in this dissertation is how many cycles a bilayer can bend before bending angle and force deteriorate. As mentioned above, the lifetime is determined by both the mechanical integrity of the bilayer and the chemical stability of

PPy. Without mechanical integrity, it is meaningless to discuss the effects of PPy stability on lifetime. Hence, research focused on creating a no-delamination interface. Then, PPy degradation was quantified. These metrics allow a more fundamental understanding of device performance. Our group is investigating other metrics, such as the strain rate and speed [13, 16]. In addition, the development of fabrication processes for cell-clinics and Kapton bulk-micromachined actuators are also introduced and discussed.

Chapter 3 Bilayers for Cell-Clinics

This chapter describes the process sequence that was developed to form bilayer microactuators and microstructures for cell-clinics, especially to build them on tiny CMOS chips. Biocompatibility and stability of bilayers and microstructures were tested to ensure their suitability for use with cells. Problems encountered during process development were identified, which motivated the work described in coming chapters to improve the design and fabrication of cell-clinics.

3.1 Fabrication of Cell-Clinics

There are two major constraints on the process sequence. First, surface micromachining has to be employed because sensors and circuitry cover the chip surface underneath a passivation layer. Second, low temperature fabrication is required because temperatures above 350 °C damage the CMOS devices.

Smela and her colleagues [124] developed the first-generation processes and demonstrated a prototype of the cell-clinics in 1999 on a silicon substrate. To begin the research on cell clinics, initial devices were created using that process, which used the "differential adhesion" method to release the bilayer hinges. This technique is an alternative to using a sacrificial layer to form a surface micromachined cantilever. It involves depositing an adhesion layer of Cr and Au, and patterning openings in it to the oxide. A second, structural Au layer (structural-Au) is deposited over this. The PPy and SU8 are deposited and patterned over the structural-Au. SU8 is a biocompatible negative photoresist [125] that forms the vials and lids. SU8 has been broadly employed in MEMS to build microstructures with heights ranging from 2 to 100 μm, which covers the size of cells [126, 127]. The structural-Au layer is etched in the final step to release the PPy/Au bilayers; the other areas on the sample are protected by photoresist during the etching. After the bilayers are released, they are able to bend away from the substrate because Au does not adhere to Si or SiO_2. The bilayers are anchored to the substrate over those areas covered by Cr. The process sequence is shown in Appendix C.

These PPy/Au bilayers were actuated to rotate the lids not only in NaDBS solution, but also in cell culture medium (Hank's balanced salt solution, which contains $CaCl_2$, KCl, NaCl and inorganic salts, Invitrogen Corp.) The actuation is shown in Figure 13.

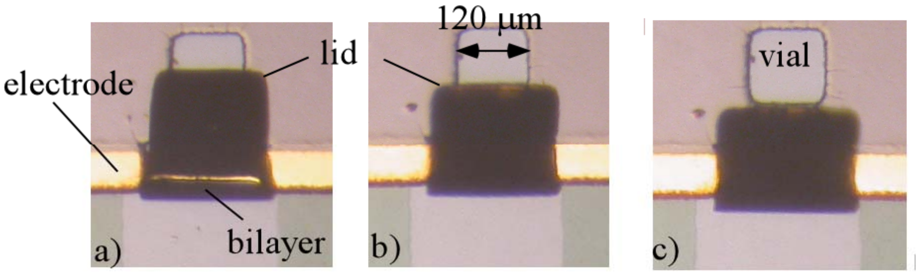

Figure 13. A PPy/Au bilayer actuated in Hank's balanced salt solution (a cell culture medium). From a) to c), a lid was rotated by the bilayer to open a vial.

There was a problem with this process, however. Photoresist pooled at the base of some SU8 structures, which prevented PPy deposition (Figure 14). The problem was caused by the nonplanarity of the surface. At the anchor areas, the pooled photoresist was too thick, so it was not properly exposed and developing did not remove it (Figure 14a).

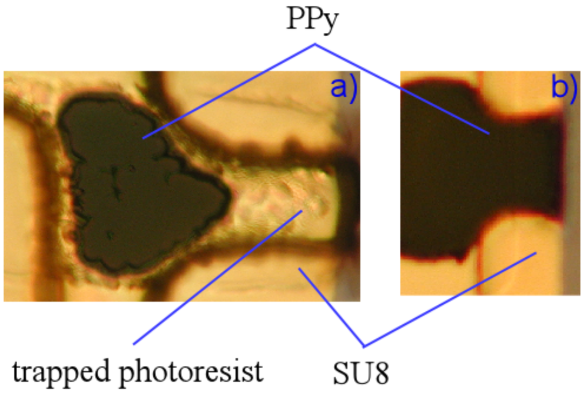

Figure 14. a) A defective bilayer. Photoresist was trapped by thick SU8 structures, which prevented PPy deposition. b) A bilayer with PPy properly filling the area surrounded by SU8.

To solve this problem, several approaches were tested during a process-development period. These details are given in Appendix C. The final result was a method that involved patterning the PPy using a photoresist template first, and then depositing and patterning the SU8. The final fabrication process is shown in Figure 15.

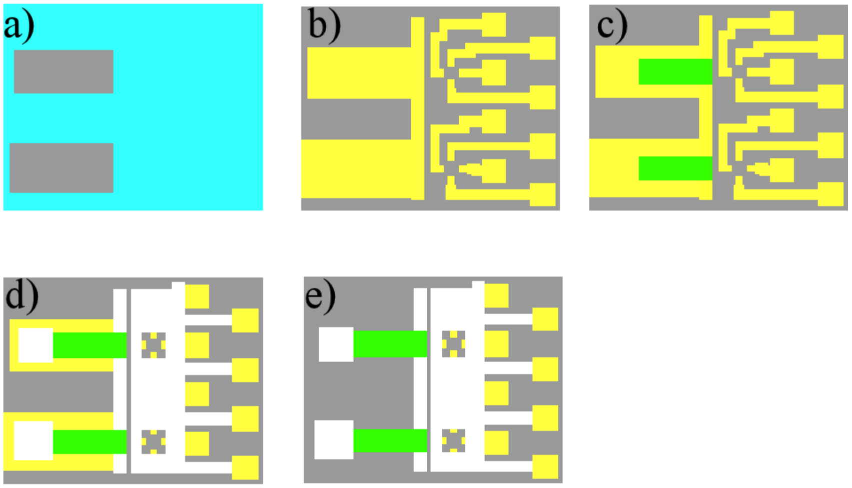

Figure 15. Fabrication process. a) Thermal evaporation and wet etching of Cr/Au to permit differential adhesion of Au structural layer. b) Thermal evaporation of Au structural layer followed by wet etching to define electrodes, bilayers, and wires. c) Patterning photoresist to form a template; PPy was deposited onto the open area of the template. d) Patterning SU8 to form lids, vials, and wire insulation. e) Etching Au to release the bilayers.

3.2 Fabrication on CMOS Chips

After developing the fabrication process successfully on silicon substrates, fabrication of microstructures on CMOS chips was begun. This switch involved treatments of the chips, finding a suitable way to handle the chips through the MEMS procedure, and adjusting the process. Before discussing the fabrication, the CMOS bioamplifier chip onto which the structures were fabricated is described.

3.2.1 The CMOS Chip

Prof. Abshire's group designed the first-generation bio-amplifier chip to sense electrical signals generated by heart muscle cells. The CMOS circuitry is briefly introduced here. The circuit is an operational transconductance amplifier in a capacitive feedback configuration as described in [128], designed for a gain range of 20 to 100 and a tunable bandwidth up to 10 kHz with supply voltages of +/-1.5 V [129]. The weak extra-cellular signals from electrically active cells (up to 500 mV, with 100 – 7,000 Hz frequency [128]) are to be amplified by an amplifier (×10 gain); the noise in the cell medium is processed by a filter (passband 500-5000 Hz, ×10 gain); finally the voltages are output to an oscilloscope (Figure 16).

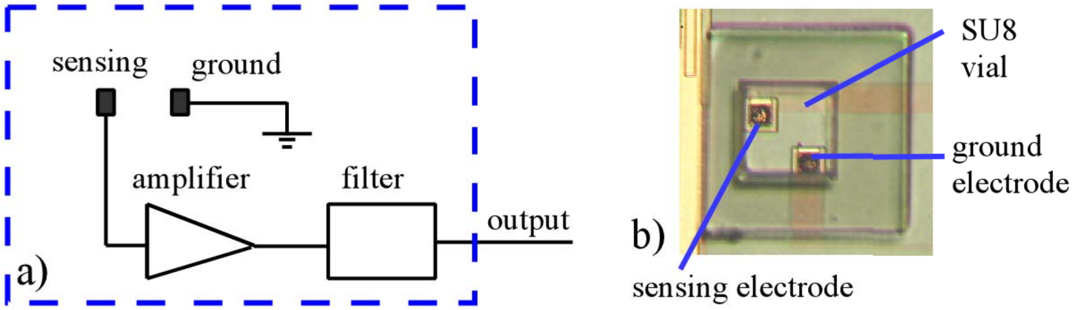

Figure 16. a) Schematic showing the function of the bio-amplifier chip. Cell signals were measured in the form of voltage, amplified by an amplifier, processed by a filter, and then output to an oscilloscope. (Courtesy of Abshire [129].) b) A photograph of the two electrodes in a SU8 vial.

The CMOS chips were the first-generation bio-amplifier chips designed by Prof. Abshire’s group. On the chip surface, there was an array of ten sensing electrodes with two sizes, 25 μm × 25 μm and 50 μm × 50 μm (Figure 17). These electrodes were comparable in size to the lidded vials. The chip surface was a layer of glass (silicon oxide) with glass cuts 2 μm down to the aluminum electrode layer.

The sensing electrode fabricated by the standard CMOS is made of Al, which corrodes in cell culture medium [130]. In order to ensure good electrical measurements, the material at the electrode/solution interface should have good corrosion-resistance. A noble metal such as Au or Pt is normally used.

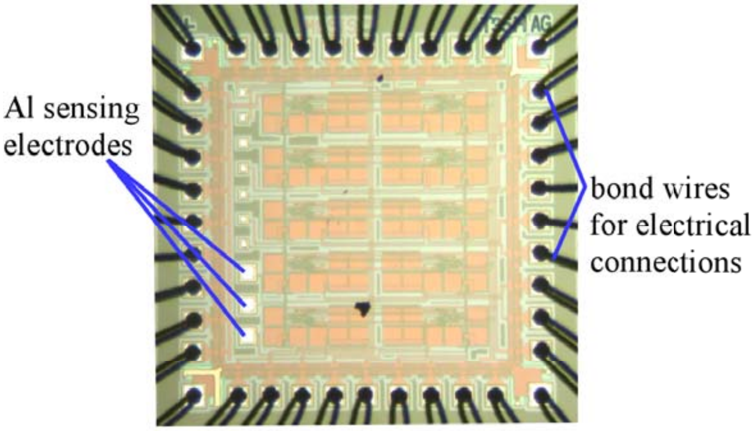

Figure 17. The first-generation bio-amplifier chip designed by Prof. Abshire's group. There is an array of ten electrodes for measurement. The chip was wire-bonded for electrical connections. (Courtesy of Abshire.)

3.2.2 Electroless Plating of Au

Since Al is not a suitable material for use as a sensing electrode in an electrolyte due to its poor corrosion resistance [130], it must be covered with another metal, such as Au. Electroless plating, instead of electroplating, avoids the need for making electrical connections to all the electrodes. Electroless plating, instead of thermal evaporation, avoids the need for patterning. (It also allows the Al on packaged chips without MEMS structures to be covered without unpackaging.) A side benefit of electroless plating is that it results in a rough layer with a higher surface area, which increases sensitivity and decreases noise during measurement.

Electroless plating is a three-step process performed using a series of commercially available solutions (Technic Inc., Cranston, RI). Because Au cannot be directly plated on Al, Zn and Ni are plated as intermediate layers (Figure 18): Zn is first plated on Al (Figure 19), and then Ni is plated on Zn (Figure 20). Finally, Au is plated on Ni (Figure 21). Detailed operations are described in Appendix G.

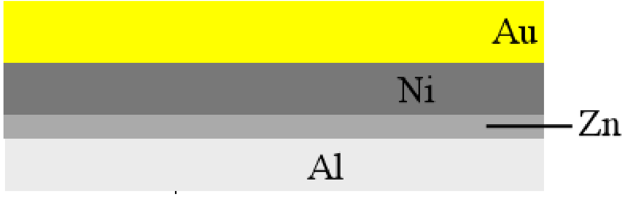

Figure 18. Two intermediate layers of Zn and Ni are deposited to facilitate Au plating on Al.

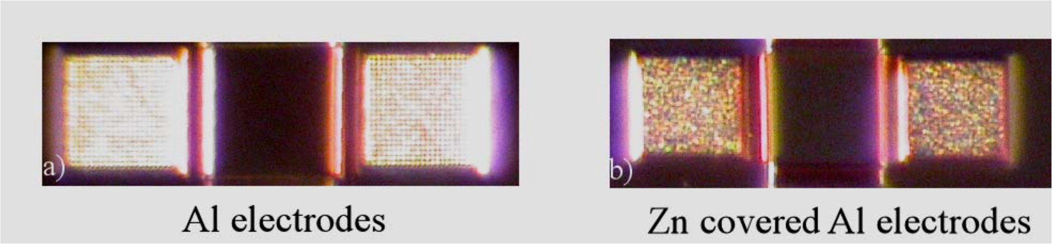

Figure 19. Zn was plated on top of Al. a) Al electrodes before plating, b) after plating.

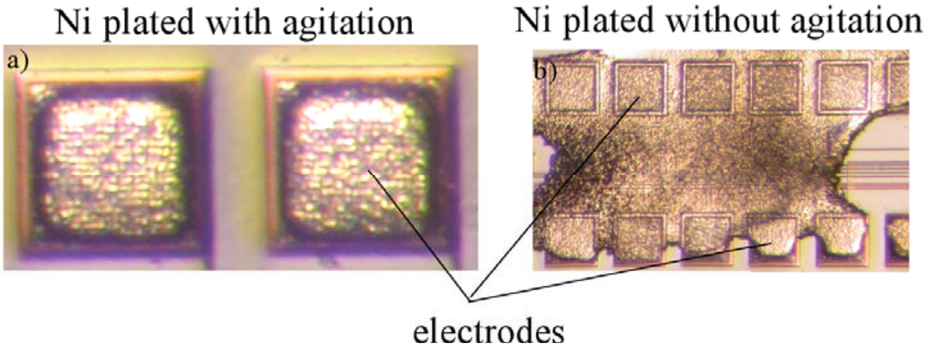

Figure 20. Ni was plated on top of Zn. Agitation was required during plating. Without agitation, Ni connected the electrodes.

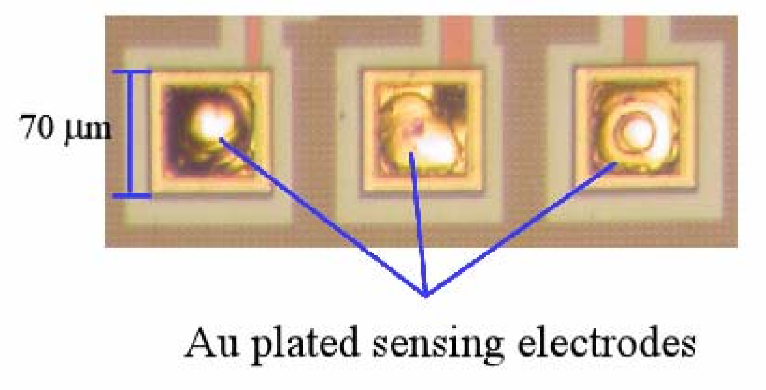

Figure 21. Au covered the Al sensing electrodes on the bio-amplifier chip.

Cleanness was a critical issue in the electroless plating. Contamination, such as NaDBS (a surfactant) on glassware, would result in uneven plating, or delamination of the plated layer (Figure 22). Therefore, only dedicated hardware (beakers, volumetric cylinders, temperature probes, and stir bars) was used for plating. Because the plating solutions are acid-based, the whole plating procedure was performed under a ventilation hood. For these small dimensions, agitation was necessary during the plating. Otherwise, Ni connected the electrodes (Figure 20).

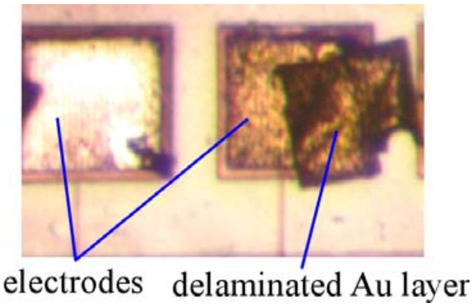

Figure 22. The Au layer on the left electrode came off due to contamination during plating.

3.2.3 Handle Wafer

The first challenge to fabricate microstructures on CMOS chips was to handle the CMOS chip because the chip was quite small (1.5 mm × 1.5 mm). Therefore a silicon handle wafer was employed. Photoresist (Shipley® 1813) was spun onto a piece of silicon (approx. 20 mm × 20 mm), and a chip was placed onto this surface and tapped gently at the edges to ensure flatness and uniform adhesion. The handle wafer was baked on a hotplate at 90 °C for 2 minutes to harden the resist "glue". After baking, the chip adhered strongly to the holder, and the combination could be handled as a regular sample (Figure 23).

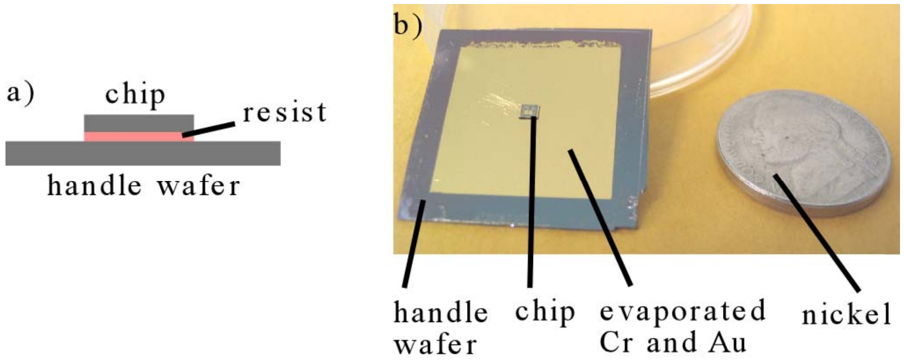

Figure 23. A CMOS chip was glued onto a piece of silicon with photoresist. The silicon piece with the chip was handled regularly through the MEMS fabrication process. a) Schematic of the cross-section of the handle wafer. b) The handle wafer was as big as a nickel. Note that Cr and Au were also evaporated onto the handle wafer during fabrication.

3.2.4 Patterning Photoresist on a Tiny Substrate

Another challenge was to obtain a flat and uniform photoresist layer by spinning. Since the chip surface was small, photoresist became exceptionally thicker at the corners due to surface tension (Figure 24a). In the worst case, uneven photoresist was seen not only at the edges, but also at the center of the chip. As a result, exposing and developing did not remove the thicker photoresist. The unpatterned Cr and Au (Figure 15a-b) shorted the bond pads locating at the edges of the chip (Figure 24b).

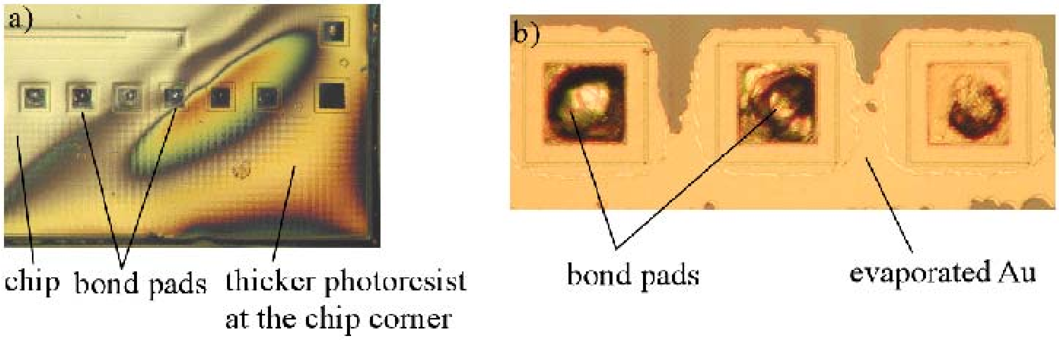

Figure 24. a) Thick photoresist at the edge of the chip due to surface tension. b) Unpatterned photoresist resulted in incomplete removal of the metal during etching, shorting the bond pads at the edges of the chip.

This problem was solved by placing the sample far away from the center of the spinner chuck. At this position, photoresist was spun under a higher velocity, which overcame the surface tension. The chip/handle wafer combination was glued close to the edge of a 4-inch wafer, again using resist (Figure 25). With a short baking time (30 seconds at 90 °C), the adhesion was strong enough to keep the chip on the 4-inch wafer during spinning, but weak enough to allow the chip to be taken off by tweezers afterward.

The photoresist spun at the higher velocity became thinner. Instead of the usual 1.5 μm thickness, when the sample was placed 40 mm from the chuck center, the photoresist was 1.2 μm thick with the same spin rate (4000 rpm) and time (30 sec.). The exposure dose therefore needed to be decreased from 120 mJ/cm^2 to 110 mJ/cm^2 at 365 nm during photolithography.

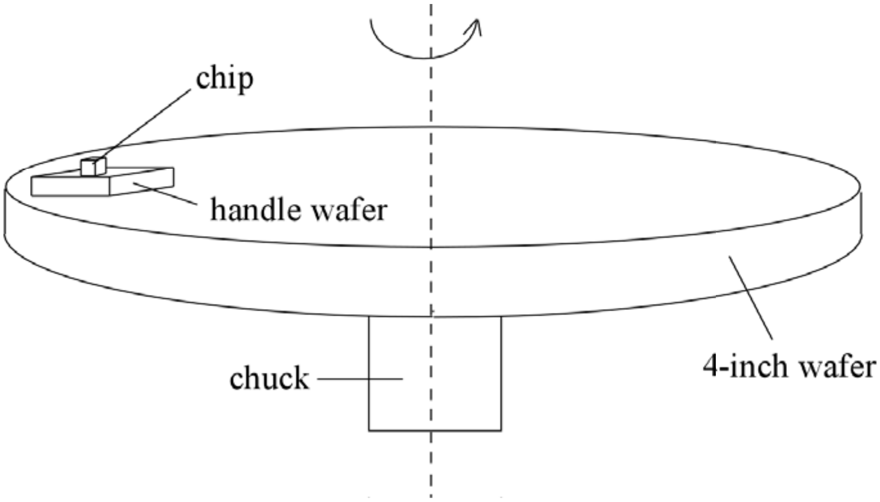

Figure 25. Schematic of spinning photoresist with higher linear velocity and acceleration rate. A 4-inch wafer was placed on the spinner chuck. The chip and handle wafer were glued to the edge of the wafer.

3.2.5 Final Microfabrication

The microstructures were fabricated on the CMOS chips by using the process shown in Figure 15. The only change was that after patterning the structural Au (Figure 15b), an electrical connection from the chip to the handle wafer was formed by wire bonding (Figure 26); the handle wafer was then clamped to the working electrode of the potentiostat to deposit PPy on the chip. After PPy deposition, the bonded wire was taken off with tweezers.

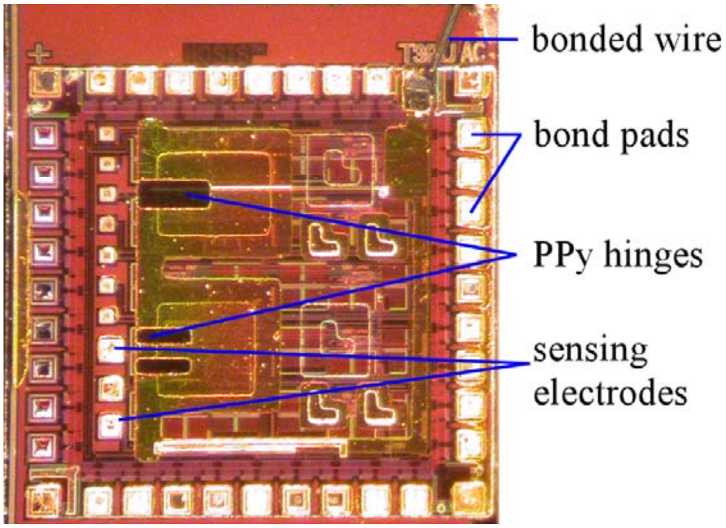

Figure 26. An electrical connection from the chip to the handle wafer was formed by wire bonding for depositing PPy.

3.2.6 Actuation Tests

To test bilayer actuation, the chip was placed into 0.1 M NaDBS solution with electrical connection made to the chip surface through a micromanipulator probe. Voltages between 0 and -1 V vs. Ag/AgCl were applied to the sample using an external potentiostat (Figure 27). Figure 28 shows a rotating lid, which verified successful fabrication.

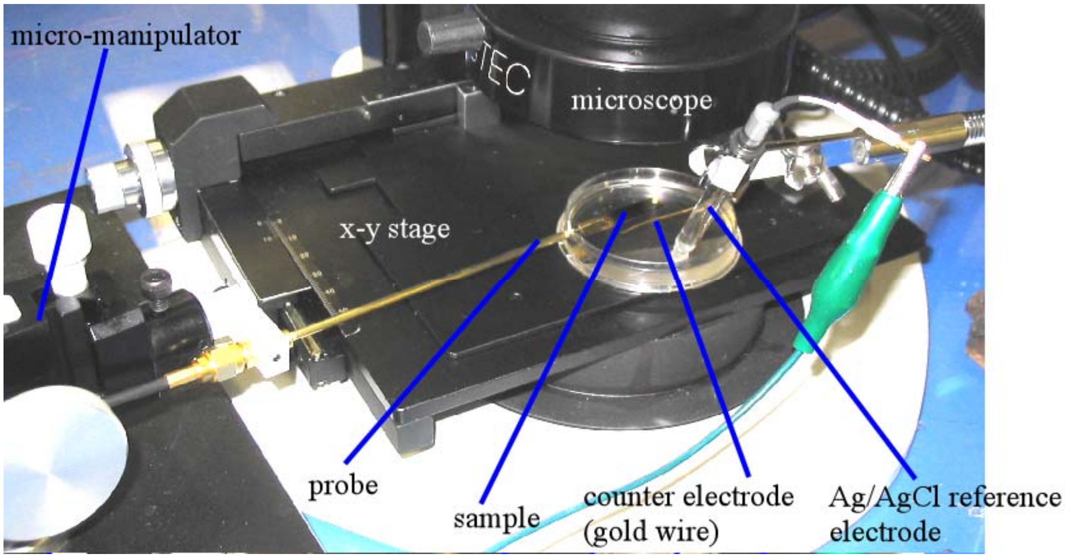

Figure 27. A setup for testing the MEMS-on-chip sample. The sample was electrically connected to the working electrode of a potentiostat through a micro-manipulator probe. Gold wire and Ag/AgCl were connected to the counter and reference electrodes.

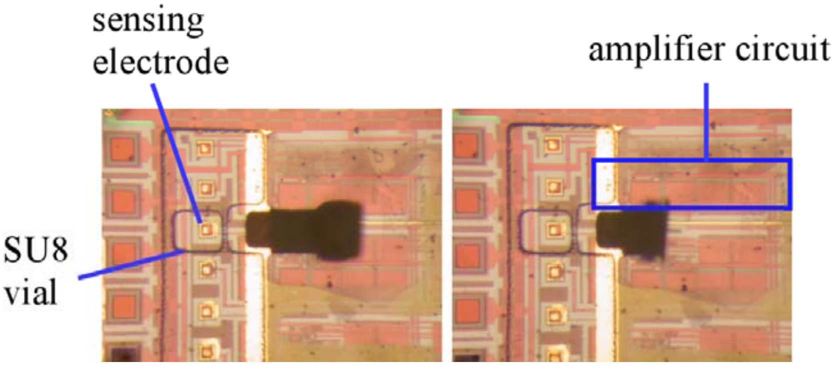

Figure 28. The MEMS process was tested by fabricating microstructures on the first-generation bio-amplifier chip. A vial was positioned around an Au-plated sensing electrode, visible as a small square. The PPy/Au bilayer was successfully actuated, as shown by the rotating lid in these images. The area of the chip with the amplifier is indicated.

Note that the lid in Figure 28, although it moved, did not close, whereas the lid is required to fully close and lie flat on the vial for encaging cells and ensuring electrical isolation. In order to satisfy these requirement, bilayers must be specified in terms of dimensions and PPy:Au thickness ratio. The distance between the anchor of bilayer and the vial has to be determined as well. Therefore, the bending behaviors were systematically characterized to improve the bilayer design; see Chapter 5 and Chapter 6 for details. In addition, the bilayers stopped bending after tens of cycles. This problem was probably due to PPy delamination from the Au surface. As a result, another line of research motivated by the actuation test in Figure 28 was to improve the fabrication for solving the delamination problem (see Chapter 4 for details).

3.3 Biocompatibility and Stability

Another issue related to fabrication is the biocompatibility and structural stability of materials used in the cell-clinics. None of the materials should be toxic to cells, corrode, or delaminate in a cell-culturing environment, e.g. 37°C, 80-95% relative humidity, and salt solution. It was reported that these materials were suitable [3, 131]. We also verified it through our own tests.

Samples were fabricated consisting of all the materials used for the cell-clinics system: SiO_2, PPy, Au, and SU8. Nicole Nelson of Prof. Abshire's group cleaned the samples with ethanol and rinsed them with DI water, then covered them with cell culture medium. She manually plated red-stained bovine aortic smooth muscle cells onto the surface of the samples, and placed them in an incubator for overnight culturing. Figure 29 shows that the cells adhered and formed processes not only on the bottom of the vial, a silicon oxide surface, but also on the surrounding SU8 and Au. The cells were continuously cultured on samples for one week, during which they stayed alive and reproduced, verifying that the microstructures were not toxic to the cells. We did not observe delaminated or corroded structures, which also verified the structural stability.

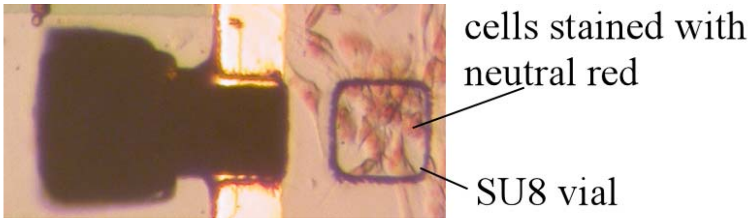

Figure 29. This was a sample only for testing the compatibility of cells and microstructures. After overnight culturing, stained bovine aortic smooth muscle cells adhered to the microstructures and spread out.

3.4 Summary

In this chapter, bilayer microactuators and microstructures were fabricated on CMOS chips. A process sequence was developed comprising low-temperature and surface micromachining steps that did not damage sensors or circuitry. Methods for handling the tiny CMOS chips and patterning photoresist on them were developed to enable fabricating MEMS on CMOS. Electroless plating Au on Al sensing electrodes was conducted to enable usage of the cell-clinics in electrolytes. All materials employed were also tested to be compatible with cells. In summary, the difficulties of fabricating the cell-clinics are essentially smoothed away. On the other hand, problems were found in the actuation, which therefore motivated work not only to improve the design and fabrication of the cell-clinics, but also to achieve a fundamental understanding of the bending behaviors of bilayer microactuators.

Chapter 4 Improving Adhesion for Long-Term Actuation

4.1 Background and Problem Statement

The operation mechanism of PPy/Au bilayer microactuators is that PPy changes volume resulting from the electrochemical redox. For PPy(DBS) layers in 0.1 M NaDBS, 2% in-plane [18] and 40% out-of-plane [132] volume change were reported (Figure 30). Because the Au layer does not change volume, cyclic stresses are generated at the interface between PPy and Au. The stresses drive the bilayer to bend from and back to the substrate. On the other hand, the stresses also become the main cause of the bilayer failure [2, 33, 106-108]: the cyclic stresses pulled PPy off Au (Figure 31). Delamination is a means of relieving the actuation-induced stress at the PPy/Au interface [133]. Delamination deteriorated the performance of PPy/Au microactuators by resulting in smaller bending angle and force and even caused a sudden device failure [33]. Furthermore, if delamination takes place in an implantable device such as the blood vessel connector [134], the PPy segments will block capillary vessels and endanger the patient's life. Hence, it is important to understand which factors contribute to delamination and how to increase long-term adhesion between PPy and the electrodes, which will not only benefit the development of the cell-clinics, but also the commercialization of conjugated polymer based devices and systems [3].

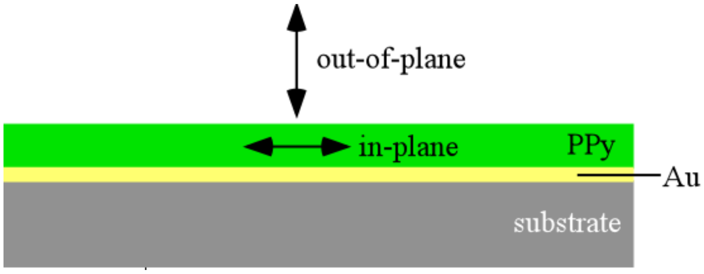

Figure 30. Schematic of PPy in-plane and out-of-plane volume change resulting from electrochemical redox.

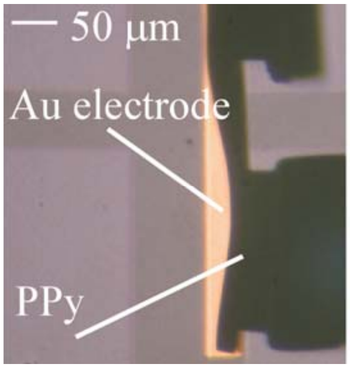

Figure 31. PPy delaminated from the Au electrode due to cyclic stresses (courtesy of Christophersen).

During electrochemical deposition of PPy, the polymer precipitates onto the Au surface. There is no chemical bonding between PPy and Au [106, 135], which results in poor adhesion. Different groups have proposed possible solutions, which are categorized into chemical and mechanical means to strengthen the bonding, and therefore improve adhesion.

Smela et al. employed thiol-modified pyrrole monolayers as possible adhesion promoters at the PPy/Au interface [136-139]. These monolayers were found to improve adhesion of as-deposited films by other groups [140-142]. However, such monolayers were shown to be unstable to electrochemical cycling [139].

Silanization is a commonly used method to promote adhesion between organic and inorganic materials [143]. Silanization can only be conducted on oxidized surfaces, such as titanium, which forms an oxide spontaneously. Guiseppi-Elie reported immobilization of PPy on sensor arrays by using silanization [144]. In our lab, this method was unsuccessful. Even it were successful, however, silanization requires a very clean surface: the surface is treated thoroughly by a series of procedures including organic solvent rinsing, UV cleaning, and baking [144]. These cleaning procedures may prevent the use of silanization on devices and systems with fragile microstructures.

In addition to the chemical means, mechanical means have also been investigated for adhesion improvement. Ding [31] deposited PPy around a wire electrode for a strong attachment: a 25 μm platinum wire was wrapped around a central platinum column (125 μm in diameter and 60 mm long) as a spiral; PPy was deposited around the column and the wire. After deposition, the column was removed manually. The actuator looked like a hollow tube and moved in the direction of the tube axis. The thin platinum wire was embedded in the PPy; it worked as the electrode around the inner surface of the tube. However, most applications still employ PPy in the flat form, especially bilayer microactuators [108].

Pyo [107] reported improving the adhesion of as-deposited PPy by increasing mechanical interlocking. A rough layer of Au was electroplated on top of a smooth layer of evaporated Au; PPy was then deposited on the rough surface. The morphology of the plated Au (e.g. the crystal size and shape) played an important role in improving the adhesion. Such “fuzzy” electrodes were used successfully for improving the adhesion of conducting polymer films on neural probes [106]. These devices were tested just after electrodeposition of the polymer and also after up to 25 cyclic voltammograms. However, the effects of Au electroplating conditions (e.g. solution concentration and plated Au thickness) on the Au morphology were not systematically investigated, nor was the adhesion improvement tested upon extended cycling. Therefore, adhesion improvement by mechanically roughening the Au electrode was investigated. Plating Au and wet etching Au were tested, and the effects of the two methods are compared in this chapter.

PPy delamination and degradation take place simultaneously, and they influence each other during electrochemical cycling. PPy degradation is believed to be due to water and oxygen in the electrolyte solution attacking the nitrogen on the polymer backbone [109, 110]. When PPy degrades, its electroactivity is lowered, which induces less stress and less tendency to delaminate. On the other hand, when PPy delaminates, the electrical contact between PPy and Au decreases; ions and electrons transported in a unit period of time decreases as well, which reduces the loss of electroactivity. A mechanical, rather than an electrical, test for adhesion was thus chosen, and the electrochemical behavior upon cycling was measured.

The test method employed was the ASTM standard tape test, D3359-02 [145]. The force applied by the tape has been reported to be 7.5 to 110 g/mm of width [146, 147] or $5\text{-}9\times10^5$ Pa [148, 149], but this depends on the tape and how strongly it sticks to the film. Because the applied force is small, the test will only minimally influence the measured lifetime. Previous work done in our group validated that the taping process did not shorten the measured lifetime, and that the interval of the taping did not affect the measurement [150]. This tape test method is also relatively simple and quick, does not damage the film, and can be applied during breaks in cycling.

In summary, PPy delamination from the Au electrode surface is a problem that has troubled the community for a long time. Various methods have been proposed to solve this problem. Among of them, mechanically roughening the Au surface by electroplating, initiated by Pyo [107], is promising and has shown adhesion improvement on as-deposited PPy. This method was further investigated, as well as another method: wet etching. The adhesion improvement was tested using a standard tape test upon electrochemical cycling. PPy degradation, which takes place simultaneously, was also investigated.

4.2 Experimental Methods

4.2.1 Sample Preparation

A 4-inch oxidized silicon wafer was sputtered with Cr (100 Å thick) and Au, and cleaved into pieces. Some pieces were used as control samples, others for further treatments of Au wet etching or Au electroplating. The sputtered Au was 2000 Å thick for electroplating Au, 3000 and 9000 Å thick for etching Au. After the treatment, PPy was electrodeposited onto Au. The thickness of PPy films was 3000 Å unless otherwise specified. Each wafer piece was cleaved into small strips (samples) so that there was a 10 mm × 10 mm area of PPy on each sample.

4.2.2 Wet-Etching of Au

A commercially available etchant (gold etchant TFA, Transene Inc., Danvers, MA) was used to etch the Au. The etching mechanism is based on the reaction (3) [151]. One part of the original Au etchant was diluted with three parts of deionized (DI) water to reduce the etching rate for a good control of the etching process.

$$\textbf{(3)} \qquad \mathbf{2Au + I_3^- + I^- \rightarrow 2AuI_2^-}$$

A major problem was inconsistent etching. When the sample was placed into the etchant, the etching takes place at the top and side of Au simultaneously (Figure 32a). As a result, Au was undercut; Au at the edge was etched much quicker than that at the center. Using photoresist to define a smaller surface area helped reducing inconsistence, but it did not solve the problem completely. By using a rocking platform (Type 100, VWR Inc., Bridgeport, NJ) for agitation (Figure 33), 1 mm wide region at the edge was etched quicker on a 15 mm × 15 mm surface (Figure 34b). To get a uniform etching area for the adhesion test, these edges were cleaved. The rocking rate was 50 cycles/min (set at rate 4) and the rocking angle was 6°. Rocking was better than stirring, which generated 3-4 times larger edges.

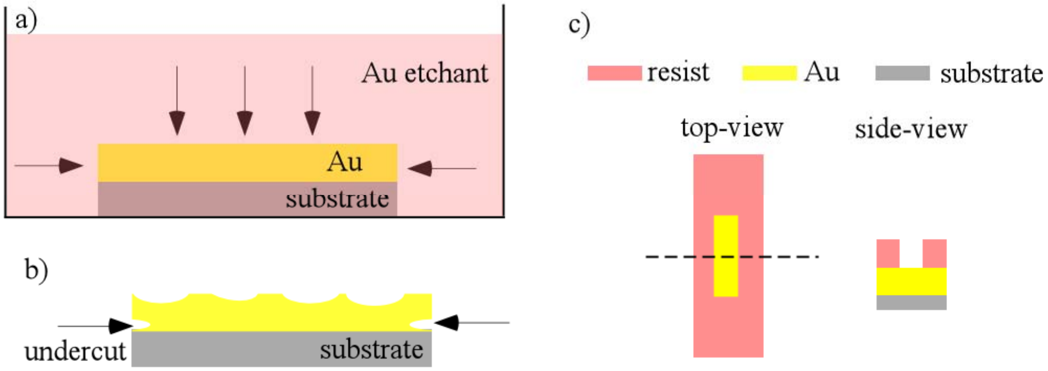

Figure 32. a-b) Schematic of Au undercutting during etching. c) Photoresist can be used to reduce undercutting.

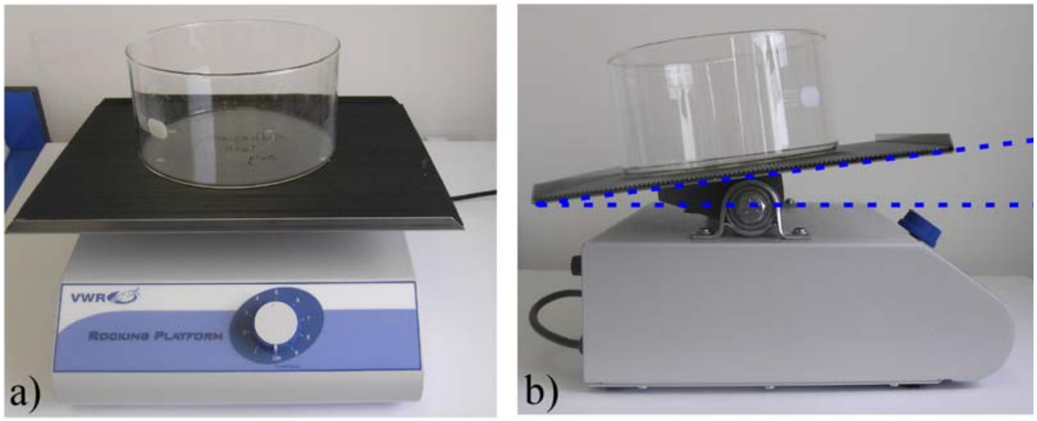

Figure 33. a) Au etching was conducted on a rocking platform for a good agitation. b) The rocking angle was 6°.

The samples were etched one by one. The etch depth was controlled by the etch time. A sample with 1.5 μm thick photoresist was etched in the rocking beaker for one minute, and then taken out, rinsed, dried, and measured by using a profilometer (Dektak^{3}ST, Veeco Inc., Santa Barbara, CA). The sample was continuously etched for one more minute and measured again. The two surface profiles are shown in Figure 34a, which shows an etch rate of 2000 Å/min. Note that the etch rate may vary with different manufacturing lots of the etchant. In addition, the etching becomes slower with more samples etched. Roughly, the etch rate remained constant during removing 8×10^{-2} mm^3 Au (e.g. remove a 8000 Å thick Au layer from one 10×10 mm^2 sample) by using 40 mL etchant and 120 mL DI water. The etch depth should always be checked by profilometry.

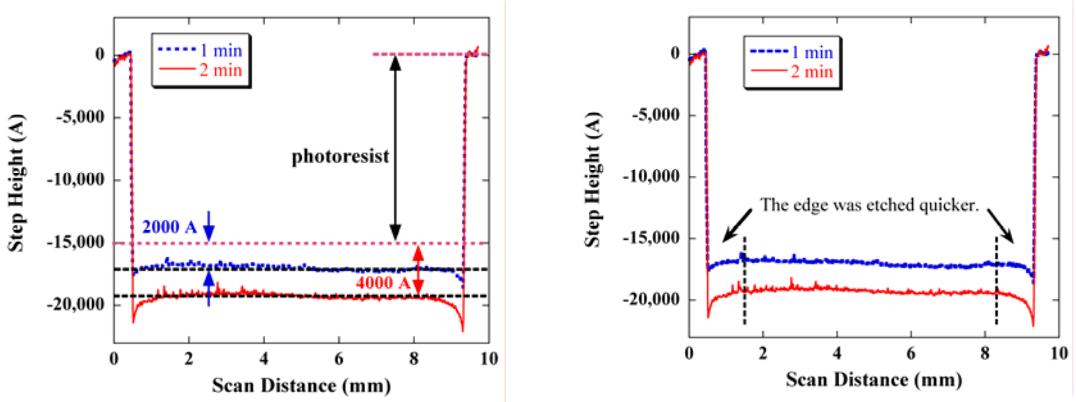

a) Profilometry of an Au surface with photoresist protection after 1 and 2-minute etching. The change of the step height shows an etch rate of 2000 Å/min.

b) Profilometry shows the etching on the 1-mm wide edge area was quicker than at the center. This edge was cleaved off for a uniform etching surface.

Figure 34. Profilometry of etched Au surfaces.

After etching, photoresist was stripped from the sample surface by using ethanol. Then, the sample was rinsed with DI water and dried with nitrogen for PPy deposition.

Samples were made with 700, 2000, 5000, and 7000 Å etch depths. The morphology of the wet-etched Au surfaces was characterized by scanning electron microscopy (SEM, S-4700, Hitachi Inc., Japan).

4.2.3 Electroplating of Au

The Au-plating setup was conducted in a three-electrode electrochemical cell. The sample was connected to the working electrode, an Au coated wafer piece was connected to the counter electrode, and Ag/AgCl was used as the reference electrode. All three electrodes were connected to a potentiostat (Autolab PGSTAT30, Eco Chemie B.V., the Netherlands). Au was plated by applying a voltage vs. the reference electrode. The thickness of plated Au was controlled by the total charge applied. The plated Au thickness was measured by surface profilometry, and the surface morphology was characterized by SEM.

The plating solution was made by mixing a commercial plating solution (Oromerse SO Part B, Technic Inc., Cranston, RI) with 1.7 M Na_2SO_3 solution. The effective ingredient of the commercial solution is $Na_3Au(SO_3)$. The Na_2SO_3 solution was used to maintain the pH of the mixture and to prevent $Na_3Au(SO_3)_2$ from decomposing [152].

$$\text{(4)} \qquad \mathbf{Au(SO_3)_2^{3-} + e \rightarrow Au^+ + 2SO_3^{2-}}$$

$$\text{(5)} \qquad \mathbf{Au^+ \rightarrow Au^0 + Au^{3+}}$$

The mechanism of plating Au [153] is that Au ions in the sulfite complex are reduced under an applied voltage:

$$\textbf{(6)} \qquad \mathbf{Na_3Au(SO_3)_2 + H_2O + e \rightarrow Au^0 + Na_2SO_3 + NaHSO_3 + OH^-}$$

Different mixing ratios of the commercial solution over the Na_2SO_3 solution were used: 1:3, 1:10, and 1:20. The corresponding concentrations of Au ions are listed in Table 1.

Table 1. The corresponding Au^+ concentrations in plate solutions with different mixing ratios.

Commercial solution:Na_2SO_3 solution (volume ratio)	1:3	1:10	1:20
Concentration of Au^+ (mol/L)	0.08	0.03	0.015

Because the commercial solution is expensive ($1,000/liter), the plate solution was recycled. According to Equation (4), the reaction reaches equilibrium at an alkaline pH, more than 9.5 as reported [153]. The pH of a newly-made plate solution (with a volume ratio of commercial solution to Na_2SO_3 of 1:10) measured using a pH meter (Type 720, Thermo Orion Inc., Beverly, MA), was 10. The pH value of the plate solution decreased with more Au plated. The plated Au layer was not uniform when the pH value was below 8.9. Therefore, the recycled solution was tested by plating Au on a scrap before putting in a real sample. Use of the recycled solution continued if the plated Au layer was uniform; otherwise a new solution was made.

Cleanliness was critical to the Au electroplating. Contaminations such as NaDBS (a surfactant) on glassware resulted in an inconsistent deposition. Therefore, only designated reference electrode, counter electrode, and glassware were used for plating. Also the samples (Au on silicon substrate) were cleaned using a freshly made piranha solution (H_2SO_4:H_2O_2:H_2O = 1:2:4 volume ratio). After cleaning, the samples were kept in DI water until electroplating.

4.2.4 Electrochemical Cycling

The samples were electrochemically cycled in 0.1 M NaDBS solution to cause stress at the PPy/Au interface, i.e. to drive PPy to delaminate. Eight samples were cycled simultaneously in a specially made electrochemical cell: all the samples were positioned in a circle and connected together to the working electrode (WE) of a potentiostat (Type BT 2000, Arbin Instruments Inc., College Station, TX). An Ag/AgCl reference electrode (RE) was put at the center of the circle. A piece of graphite (VWR International, West Chester, PA) was placed at the bottom of the cell as the counter electrode (CE), perpendicular to the WE and RE. As a result, each sample had nearly identical position with respect to the RE and CE (Figure 35). The voltages were switched between 0 V and –1 V to mimic the real environment in which stepping voltages are applied for a rapid bending of bilayer. The voltage was hold until the PPy films were fully oxidized or reduced (Figure 36).

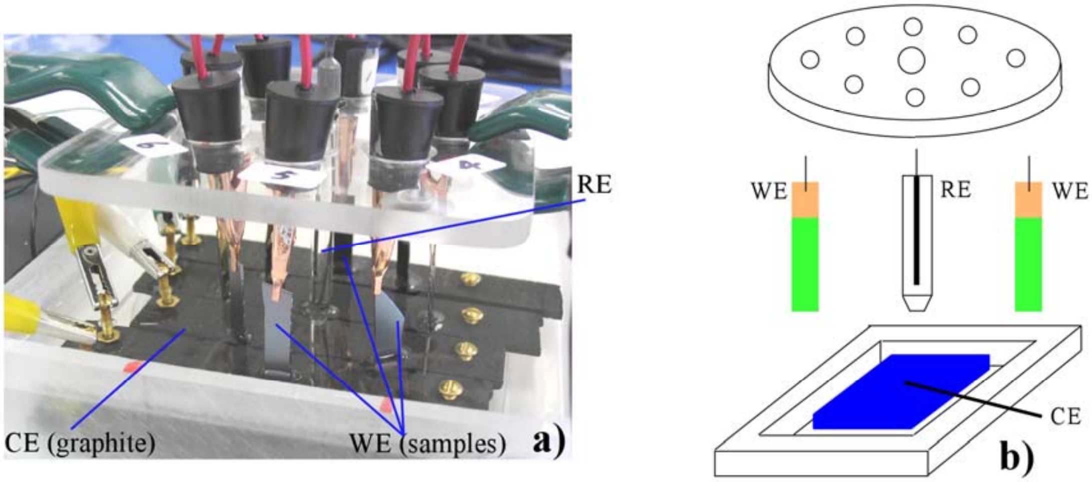

Figure 35. Eight samples were electrochemically cycled simultaneously in a specially made electrochemical cell to drive PPy to delaminate. Each sample had nearly identical position with respect to the RE (Ag/AgCl) and CE (graphite). a) Photograph. b) Schematic.

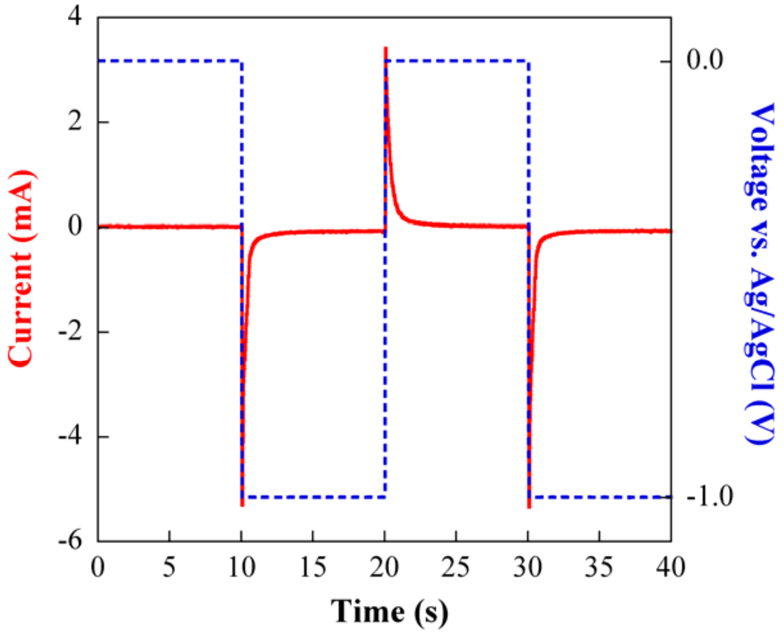

Figure 36. Voltage (dashed line) and current (solid line) vs. time when a 3000 Å thick PPy film was cycled between 0 V and –1 V vs. Ag/AgCl. The corresponding current became constant after 4 seconds at each voltage, which implied PPy was fully oxidized and reduced.

Samples were cycled under the stepping voltages until they failed. In this chapter, the definition of sample "failure" is: 1) PPy comes off completely from the Au surface; 2) PPy loses its electroactivity even it still adheres to the Au surface. In order to check the electroactivity of PPy, triangular voltage ramps (Figure 4 in section 2.2.2), not the stepping voltages, were applied and cyclic voltammetry (CV) curves were recorded periodically before and after cycling. The oxidation/reduction peaks almost disappeared after 55,000 to 60,000 cycles (Figure 37), which implies the polymer degraded and lost its electroactivity. Electro-inactive PPy does not undergo volume change, so no further delamination takes place. Stepping was stopped when there was no PPy remaining on the Au or the PPy was no longer electroactive, and this defined the lifetime of the sample. The longer the lifetime is, the better the adhesion.

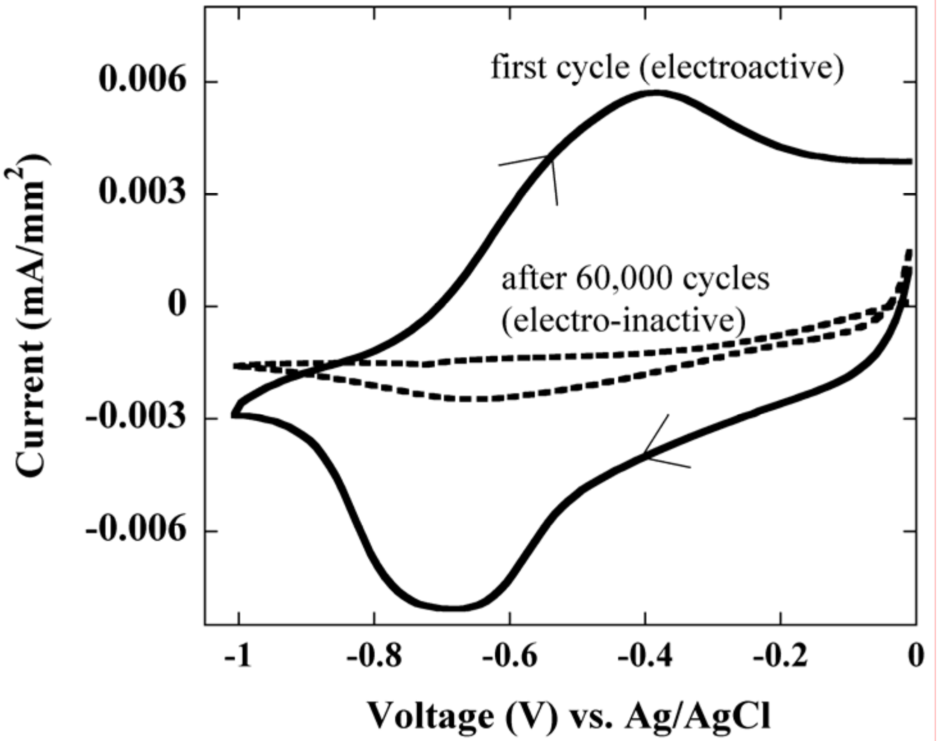

Figure 37. Cyclic voltammetry curve at 50 mV/s of PPy after 60,000 cycles shows almost no redox peaks compared to that of the first cycling. It implies PPy loses electroactivity.

4.2.5 The Tape Test

A tape test was used to find when delamination took place and how much of PPy came off from Au. The applied voltage cycles were usually stopped every 5,000 cycles. The samples were taken out of the cell, rinsed with DI water, and dried with nitrogen. A piece of Scotch® tape (Type 810, 3M Inc., St. Paul, MN) was placed on PPy and pressed by a finger. Color change was seen to ensure the tape had a good contact with PPy. The tape was removed with the pulling force parallel to the sample (Figure 38). If PPy came off, the delaminated PPy would stick to the tape. After the tape test, the samples were put back into the cell and the cycling test continued. Figure 39 shows PPy came off gradually, starting at the edge because the interfacial shear stresses concentrate at the edges of the film [154]. No PPy was left on the Au after 20,000 cycles. A curve of cycling number vs. delamination percentage was drawn based on the tape test results (Figure 40).

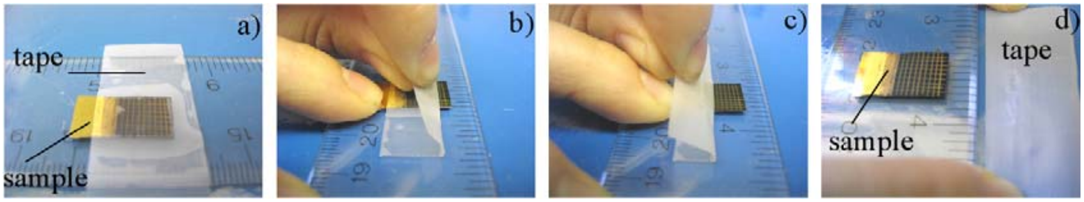

Figure 38. Illustration of the tape test. a) Place a piece of Scotch® tape on PPy and pressed by a finger to ensure contact. b-c) The tape was removed with pulling force parallel to the sample. If PPy came off, the delaminated PPy would stick to the tape. d) No delamination was seen on this sample.

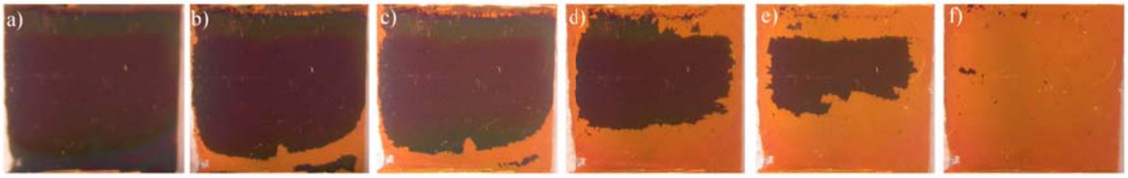

before cycling after 4,000 cycles after 10,000 cycles after 16,000 cycles after 18,000 cycles after 20,000 cycles

Figure 39. PPy came off gradually and no PPy was left on Au after 20,000 cycles on this sample (3000 Å PPy on 1800 Å Au plated at –0.9 V vs. Ag/AgCl by using a solution of 1:10 concentration).

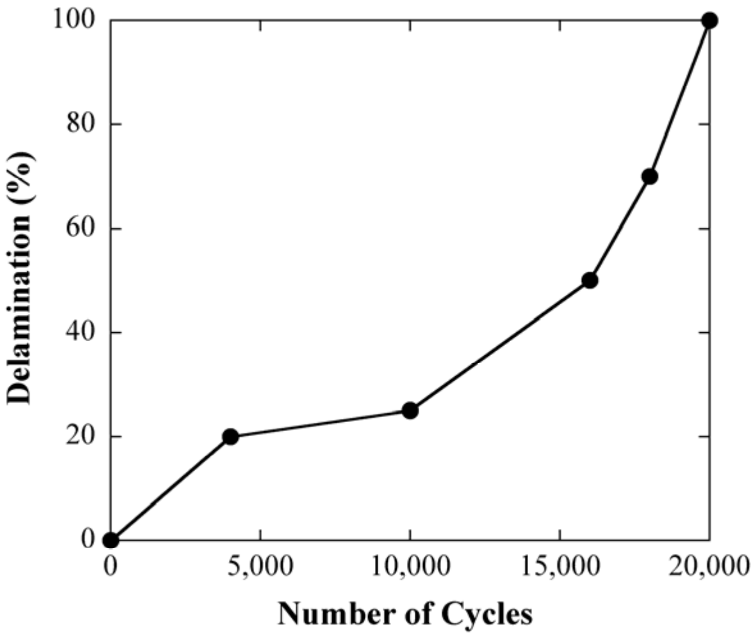

Figure 40. A curve of cycle number vs. delamination percentage was drawn based on the tape test results in Figure 39.

There is a standard tape test method released by the American Society for Testing and Materials (ASTM D3359-02): Standard Test Methods for Measuring Adhesion by Tape Test [145]. This method requires scribing the sample surface to form a grid for quantifying delamination (Figure 38). Tape tests were also done directly on samples without a grid (called the regular method). Test results from the ASTM and regular methods were compared by testing 2 groups of samples: control samples (Figure 41a) and electroplated samples with 1 μm thick Au (Figure 41b). The samples showed similar lifetimes and delamination tendency under the two tape testing methods. One control sample showed an exceptionally long lifetime, 12,000 cycles, under the ASTM method, which was most likely due to the large lifetime distribution of the control samples (see section 4.3 for details). Hence, there was no difference between the two methods.

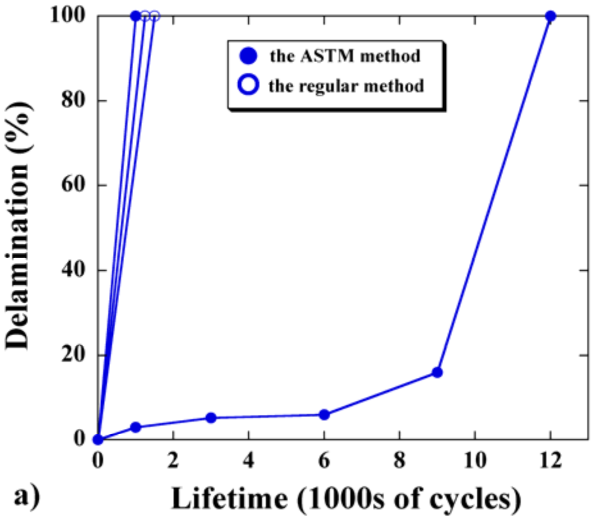

Four control samples were tested by the ASTM and regular methods. Three samples had similar lifetime and delamination tendency. One exceptional sample may be due to the large lifetime distribution of the control samples.

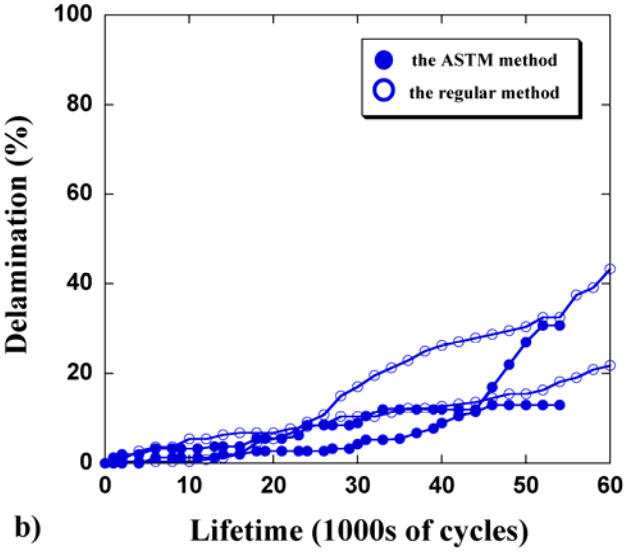

Four electroplated samples were tested by the ASTM and regular methods. They had similar lifetime and delamination tendency.

Figure 41. Control and plated samples were tape tested using the ASTM and regular methods. No obvious differences were observed, which verified that the two methods were identical.

4.2.6 Summary

The experimental procedure is summarized in Figure 42: PPy was deposited on bare Au (as control samples), etched Au, and electroplated Au. Samples were electrochemically cycled to drive PPy to delaminate. The adhesion between PPy and Au was characterized by a tape test and quantified into a delamination curve.

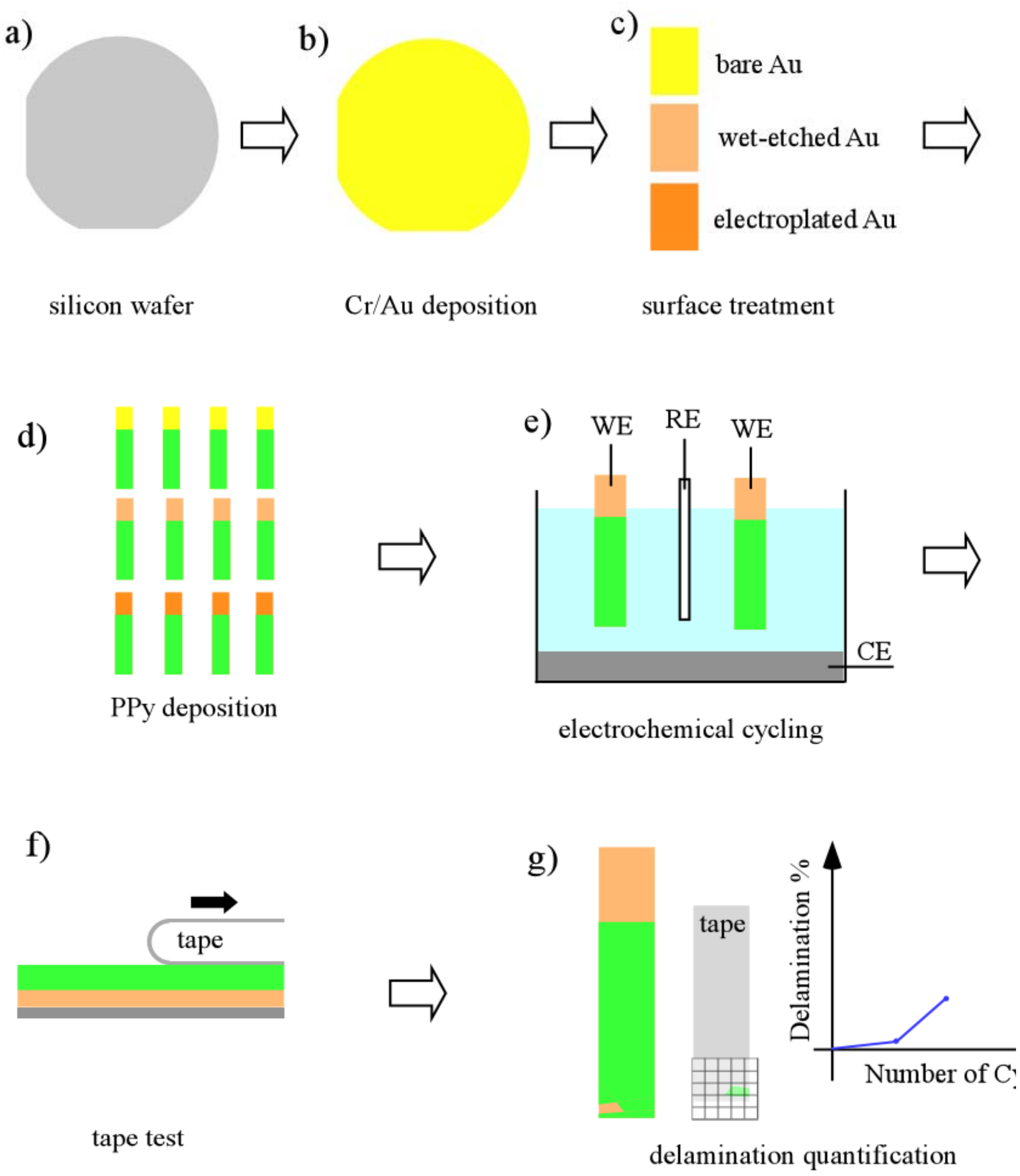

Figure 42. Summary of the experimental procedure. a) Start with 4-inch silicon wafer substrate. b) Sputter Cr/Au onto the wafer. c) Cleave the wafer into pieces, wet-etch and electroplate. d) Cleave wafer pieces into strips as samples, deposit PPy. Samples without treatment were control samples. e) Cycle samples to drive them to delaminate. f) Test adhesion by a tape test every thousands of cycles. g) Quantify delaminated PPy on the tape into a lifetime curve.

4.3 Lifetime of Control Samples

Before discussing the adhesion improvement, we want to know the lifetime of control samples (untreated surface). Twenty seven control samples were cleaved from 6 wafers sputtered with Au in different batches. The average lifetime of the controls samples was 7,000 cycles (Figure 43). There was a significant variation in lifetime among the samples from different batches. The average lifetime in batches 1-5 was quite similar, 4,500 cycles, whereas it was 17,000 cycles in the batch 6. Even the samples coming from the same wafer had considerable variation. The reason for the lifetime variation is still unknown. It is clear, however, that the untreated surfaces are not good for possible applications due to the uncertain lifetime.

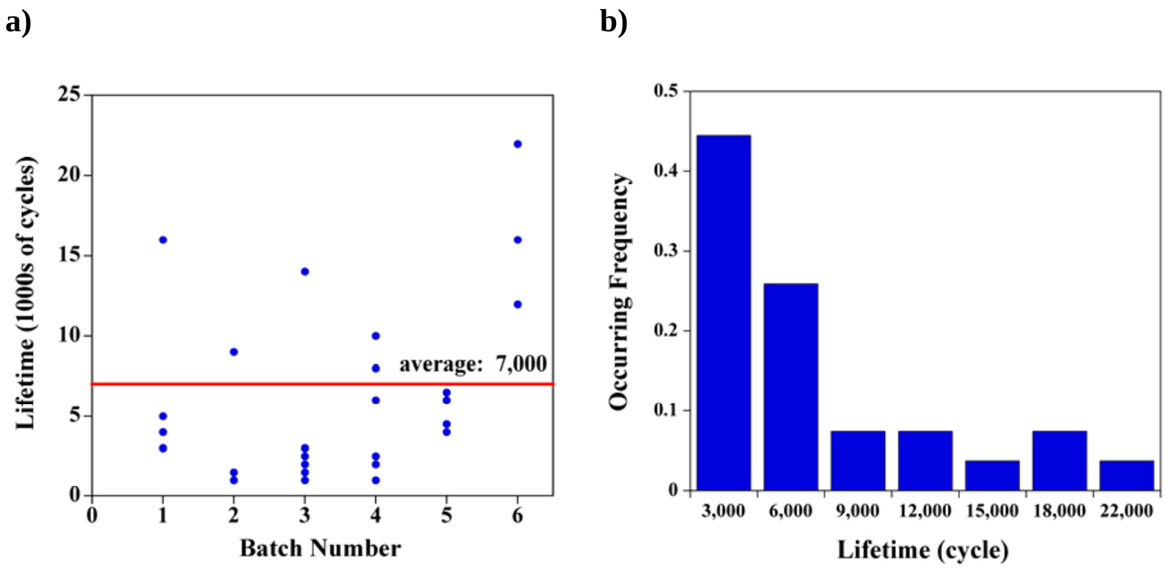

Figure 43. The lifetime of control samples. a) In 27 samples coming from 6 batches of sputtering, the average lifetime was 7,000 cycles. b) Nearly half of the control samples failed within the first 5,000 cycles, and 90% failed within 15,000 cycles.

4.4 Effect of Plating

This section describes the effect of different plating conditions on the adhesion in terms of the lifetime and Au morphology. Table 2 summarizes the electroplating conditions and values tested that might affect adhesion. They are discussed individually.

Table 2. Summary of the factors and values of electroplating that were tested.

Au plate conditions	**Plate voltage**	**Plated Au thickness**	**Plate solution concentration**
Values tested	-0.9 V -1.25 V	< 1000 Å 1000 – 5000 Å > 1 μm	1:3 1:10 1:20

4.4.1 Effect of Plating Voltage

During electroplating, the applied voltage is the driving force for electrochemical reactions. In order to find suitable plating voltages, a linear voltage sweep from 0 V to -1.6 V vs. Ag/AgCl was applied at 50 mV/s in a 1:3 plating solution, and the corresponding current recorded (Figure 44). When the applied voltage was less negatively than -0.7 V, the current was small, which means a slow or even no plating. When the voltage became more negative, the current increased, and a current peak was observed at -1.25 V. Bubbles were generated when the voltage was more negatively than -1.30 V, which is related to the hydrogen evolution reaction (equation (7)) [155]. For the plate solutions of three different concentrations (Table 1), the shape of the sweep curve remained the same, and only the voltages corresponding to the current peaks varied slightly.

$$\mathbf{(7)}\qquad \mathbf{2H^+ + 2e \rightarrow H_2}$$

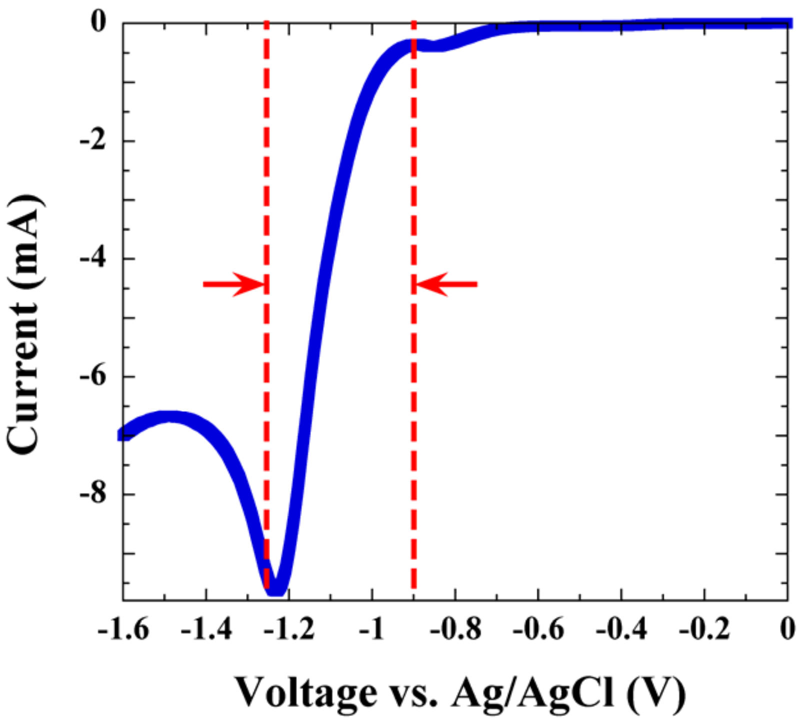

Figure 44. A linear sweep voltammogram from 0 V to -1.6 V vs. Ag/AgCl (50 mV/s).

The lifetimes of samples plated from -0.9 V to -1.25 V were compared. Comparable samples had similar thicknesses of Au, and plating was done in 1:3 and 1:10 concentration. For samples plated in 1:3 concentration with thicknesses ranging from 40 to 330 nm thickness (Figure 45a), there was no difference in lifetime, regardless of whether the Au was plated by applying -0.9 V or -1.25 V. For samples plated in 1:10 concentration, similar results were also observed (Figure 45b). Hence, it can be concluded that the plate voltage did not play an important role in adhesion.

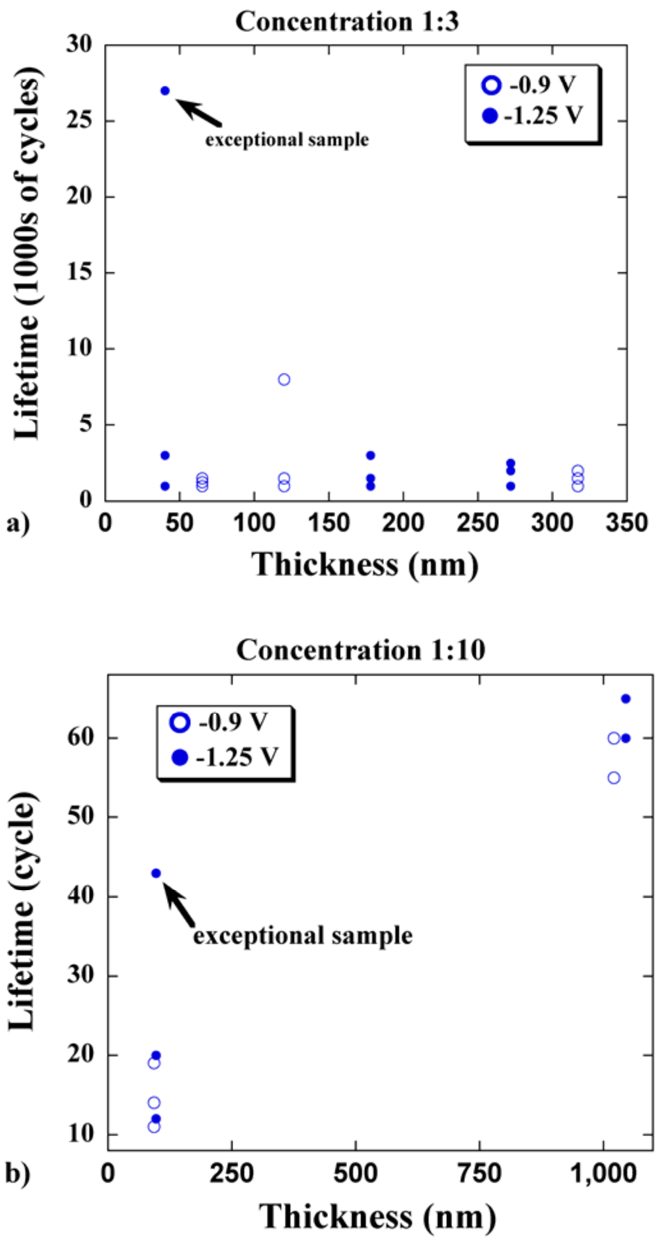

Figure 45. Lifetime of samples with Au plated at -0.9 V and -1.25 V in (a) 1:3 and (b) 1:10 concentration solution. Samples with similar thickness had similar lifetimes (except for two exceptional samples).

Two samples with plated Au thinner than 100 nm had exceptionally long lifetime.

Possibly the plated Au was too thin to “suppress” the significant variation of lifetime among untreated samples.

Although the plate voltage did not affect adhesion, it affected the MEMS fabrication. When Au was plated on the cell-clinics at -1.25 V, bubbles were formed on the Cr/Au opening of the MEMS structures (Figure 46). These bubbles made the Au layer easy to break in subsequent fabrication. Hence, Au was always plated on cell-clinics at -0.9 V.

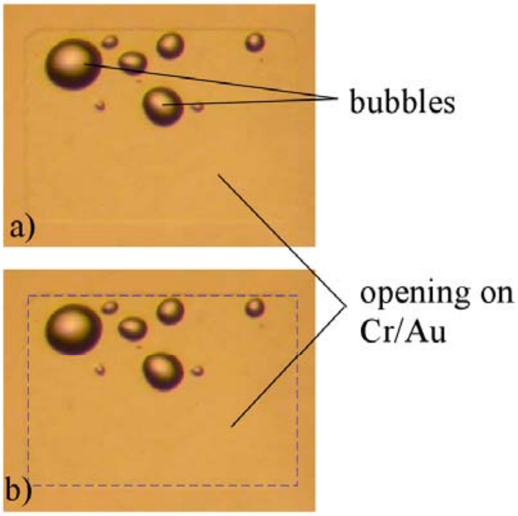

Figure 46. When Au was plated at -1.25 V, bubbles were formed on the Cr/Au opening. These bubbles made the Au layer easy to break during MEMS fabrication.

4.4.2 Effect of Plated Au Thickness

Figure 47 and Figure 48 show that 1 μm thick plated Au had a much longer lifetime. When PPy lost electroactivity, there was still 40-80% PPy remaining on Au (Figure 48). PPy on the thinner plated Au completely delaminated by 30,000 cycles, while 0.4 μm thick plated Au seems in the middle of the transition: two samples completely failed by

50,000 cycles while one sample retained 60% of the PPy when it lost activity. Hence, thicker plated Au helped improving the adhesion.

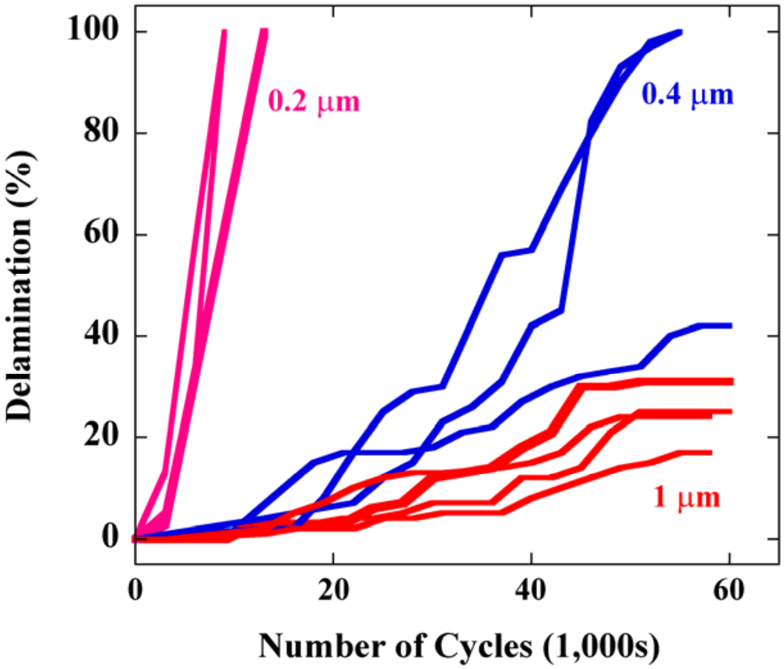

Figure 47. Lifetime of samples plated in 1:3 concentration. Samples with plated Au 1 μm and thicker demonstrated much longer life.

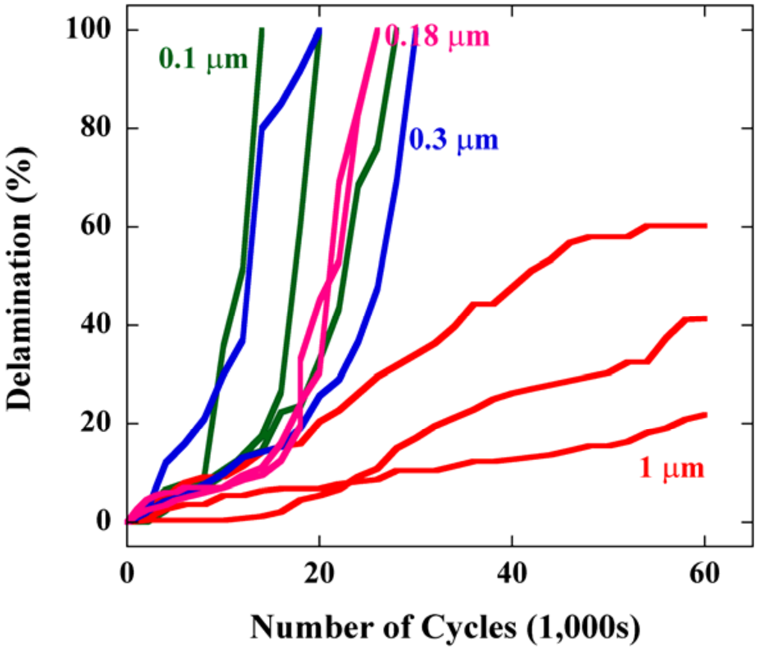

Figure 48. Lifetime of samples plated in 1:10 concentration. Samples with plated Au 1 μm and thicker again demonstrated much longer life.

From top-view SEM micrographs (Figure 49-Figure 50), the crystal size of plated Au increased with thickness. Furthermore, from side-view SEM micrographs, the crystal grains of 1 μm thick plated Au protruded and formed an irregular surface (Figure 51b-c). The irregular surface created anchor sites for PPy to hold, which improved the adhesion. In contrast, the surface of thinner plated Au, e.g. the surface of 0.3 μm thick plated Au, was quite flat and uniform (Figure 51a).

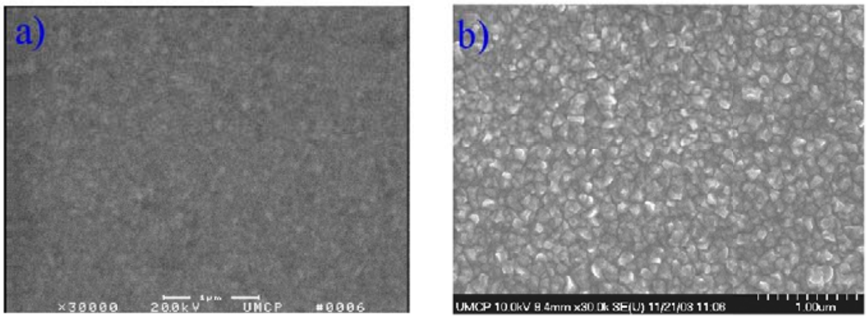

sputtered Au

0.1 μm

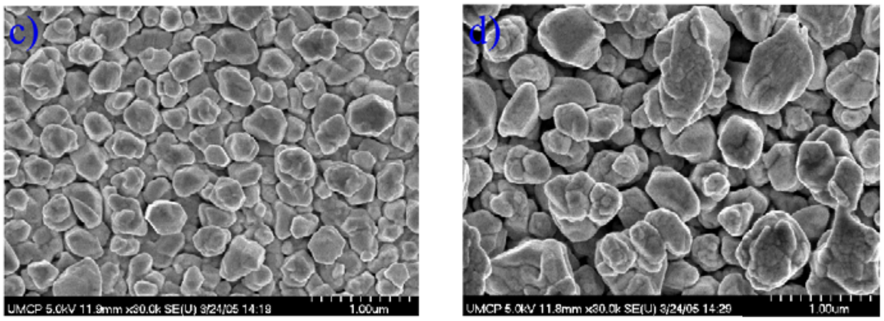

0.4 μm

1 μm

Figure 49. Top-view SEM micrographs of Au plated in 1:3 concentration.

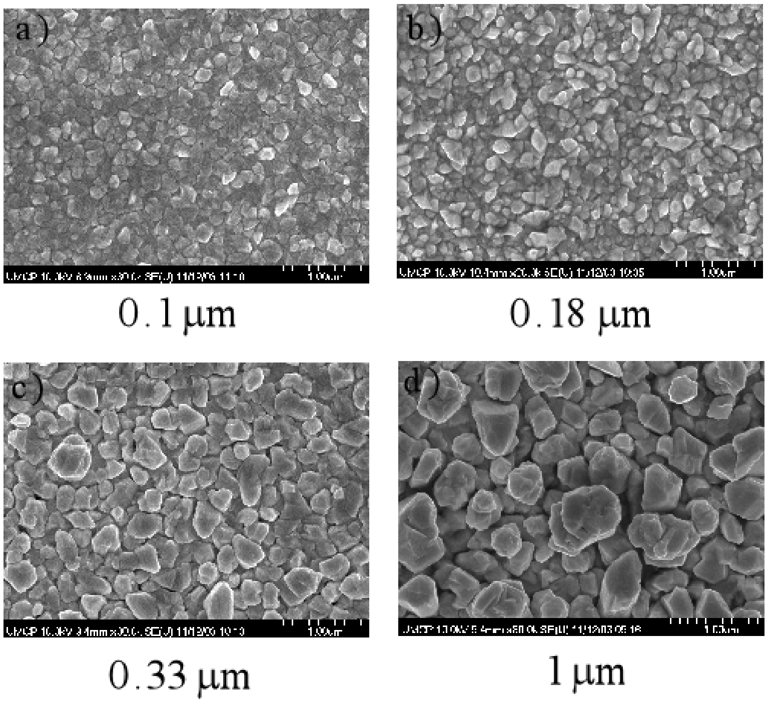

0.1 μm

0.18 μm

0.33 μm

1 μm

Figure 50. Top-view SEM micrographs of plated Au in 1:10 concentration.

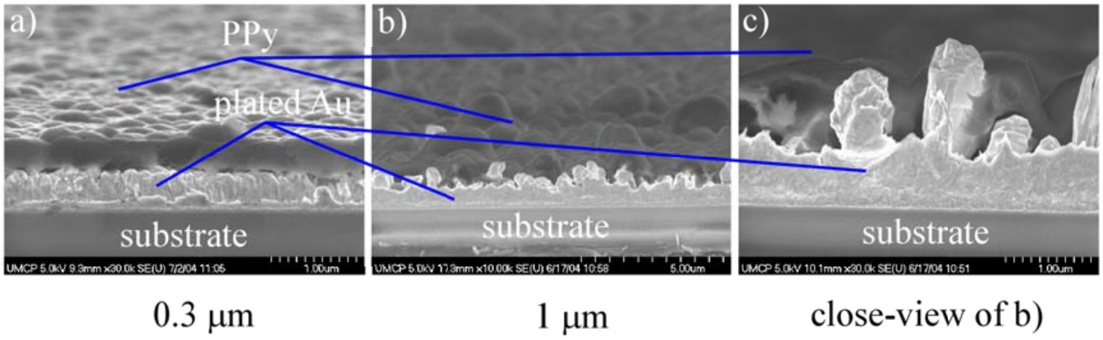

0.3 μm

1 μm

close-view of b)

Figure 51. Side-view SEM micrographs of a) 0.3 μm and b-c) 1 μm thick electroplated Au at -1.25 V in 1:10 concentration. The crystal grains of 1 μm thick plated Au protruded and formed an irregular surface.

Watanabe [156] proposed a mechanism to explain the surface morphology change with increased plated film thickness (Figure 52). During plating, the metal ions (M^+) are reduced, so a metal ion denuded layer (MIDL) is formed in the area close to the substrate surface. The metal ions diffuse to “refill” the MIDL to continue the plating. In practice, ion diffusion and reduction are not uniform due to heat fluctuation, so the thickness of the MIDL varies on the surface. At the site that the MIDL is thinner, more ions are reduced. As a result, a protrusion site is formed on the plated film. Simultaneously, a valley site is formed at the site with thicker MIDL. As plating progresses, ion reduction at the protrusion sites is continuously promoted. The film surface becomes rougher with more metal plated, and an irregular surface is formed.

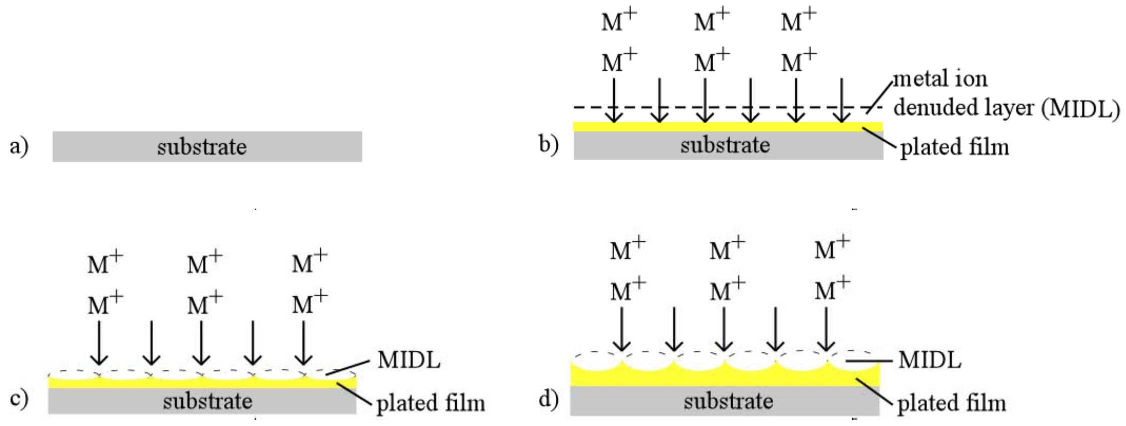

Figure 52. Schematic of Watanabe's mechanism to explain the surface morphology change with increased plated film thickness. a-b) A metal ion denuded layer (MIDL) is formed in the area close to the substrate surface because of metal ion reduction. The metal ions diffuse to "refill" the MIDL to continue the plating. c) The thickness of the MIDL varies on the surface, which generates protrusion and valley sites. d) As plating progresses, ion reduction at the protrusion sites is continuously promoted. Finally, an irregular surface is formed. (Courtesy of Watanabe [156].)

4.4.3 Effect of Solution Concentration

Figure 53 shows that the plated Au from the 1:10 concentration had a longer lifetime than those from 1:3 concentration. The lifetime variance can be explained based on Watanabe's mechanism [156]. Film growth at the valley sites comes from an overflow of metal atoms from the protrusion sites (Figure 54a). When a plating solution of lower concentration is used, the metal ions diffusing to the MIDL become fewer in a unit period of time, so do the metal atoms added to the film. As a result, the overflow of atoms to the valley sites becomes weaker. The extent of the overflow determines the distance that an atom moves from the protrusion to the valley via surface diffusion. The atoms move shorter because of the weaker overflow, which leads to a less rounded region between the protrusion and valley sites (Figure 54b). Hence, a lower concentration solution is favorable to generate a more irregular surface. As a result, additional samples were plated using 1:20 concentration and tested.

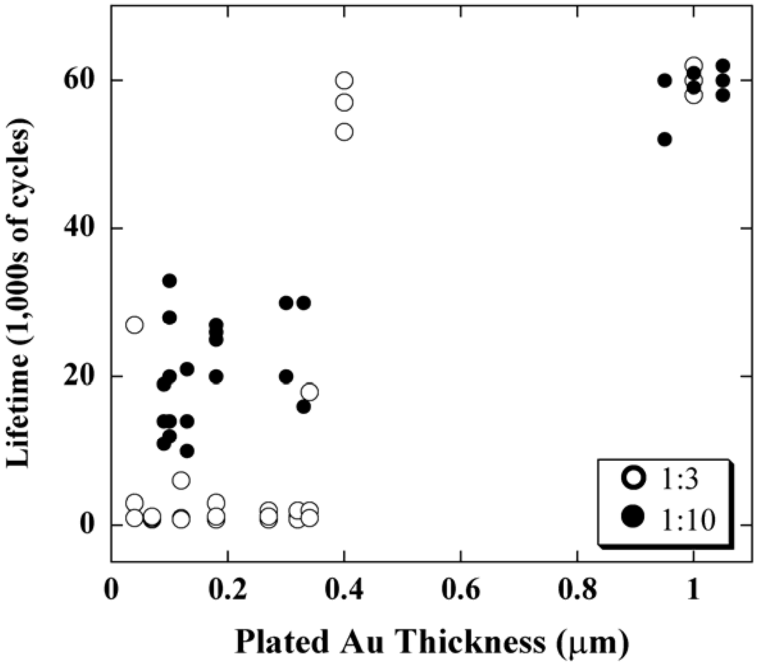

Figure 53. Samples plated in 1:10 concentration had a longer life than those in 1:3 concentration.

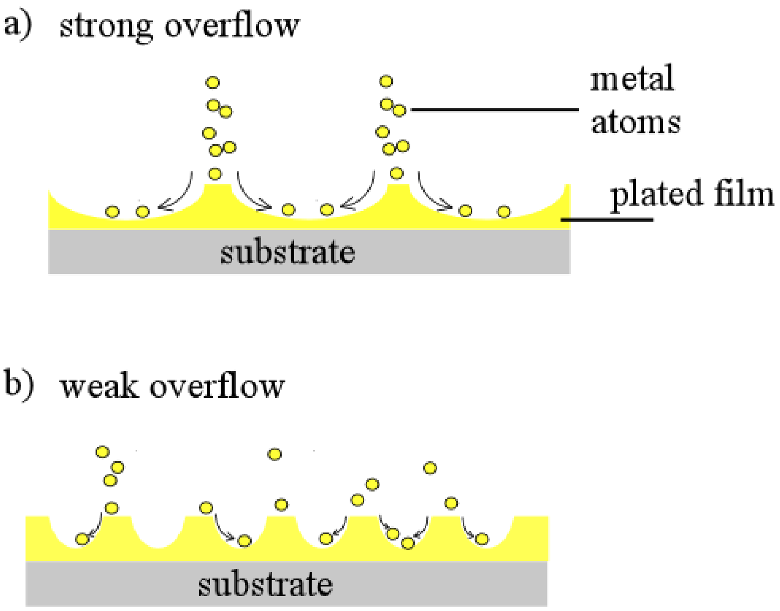

Figure 54. Schematic of surface morphology affected by solution concentration [156]. a) High concentration leads to strong overflow and longer diffusion distance of atoms from the protrusion to the valley site, which creates a more rounded surface morphology. b) Low concentration leads to weak overflow and shorter diffusion distance of atoms, which creates a more irregular surface morphology.

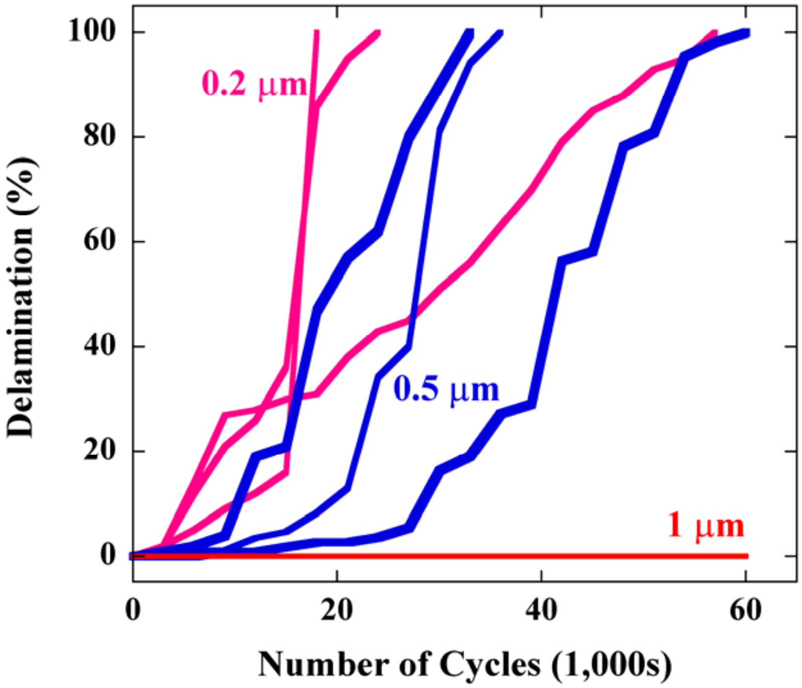

Figure 55. Lifetime of samples plated in 1:20 concentration. Samples with 1 μm thick plated Au demonstrated no delamination.

There was no delamination from 1 μm thick Au plated in 1:20 concentration (Figure 55). Other students in our group (Q. Gan and S. Baig, ME department) independently plated 1 μm thick Au samples in 1:20 concentration solution and repeated the adhesion test. Their results confirmed that no delamination took place during cycling. No obvious difference can be seen from the top-view (Figure 56a and d) and side-view micrographs (Figure 56b, c, e, and f): both show protrusions on the surface. The reason for no delamination on 1:20 samples could not be determined from the micrographs. By using the linear intercept procedure describe in the ASTM standard [157], the average grain sizes of Au were compared. A grid comprising 5×5 test lines was drawn on top of the micrographs by using drawing software (Canvas, version 7SE, ACD Systems Inc., Canada). The test line crossed a number of grains, and the length of the overlap between the test line and these grains were measured; this is the intercept length. The measurement was conducted on 8 micrographs of samples plated in 1:10 concentration and 6 micrographs of 1:20 concentration samples. More than 250 intercepts in total were obtained, respectively. The average grain size of 1:10 and 1:20 concentration samples was 0.39±0.17 μm and 0.34±0.19 μm, correspondingly. The distribution of grain size was quite similar in both cases, as shown in Figure 57. Hence, it is difficult to explain the reason that the 1:20 concentration samples had a better adhesion. Other analytical tools such as AFM may be helpful to answer this question by investigating the detailed microstructures of plated Au, but the results on identifying and generating such a rough surface are good enough to be able to start using the method in applications. Note that a concentration lower than 1:20 was also tried. The plate rate became very slow and Au deposited preferentially on the edges due to higher electric fields, which resulted in an inconsistent plated layer. Therefore, it is impractical to use lower concentrations.

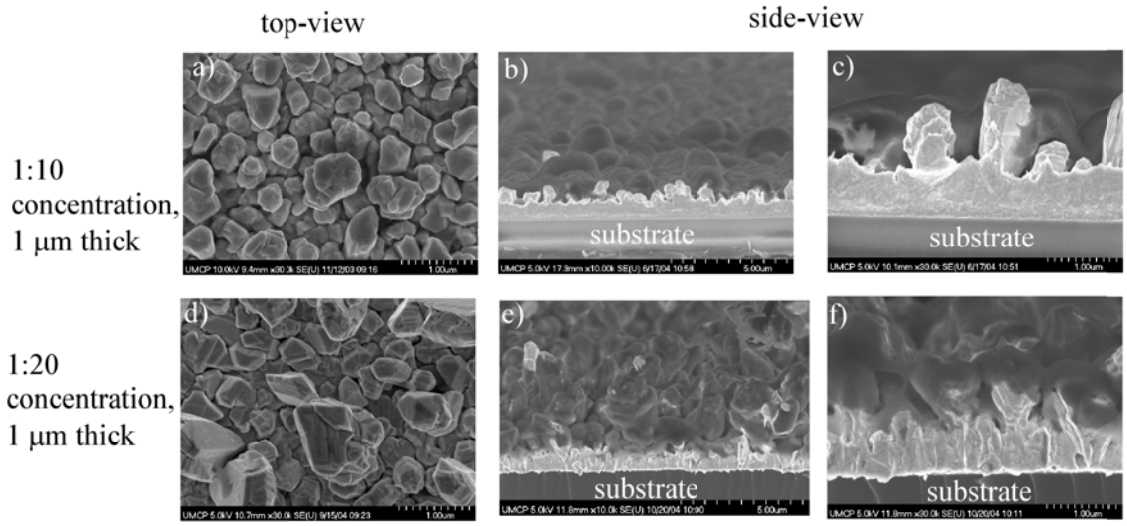

Figure 56. SEM micrographs taken on 1 μm thick Au plated in 1:10 and 1:20 concentration. a) and d) are top-view micrographs. The side-view micrographs (b, c, e, and f) show protrusions on both samples.

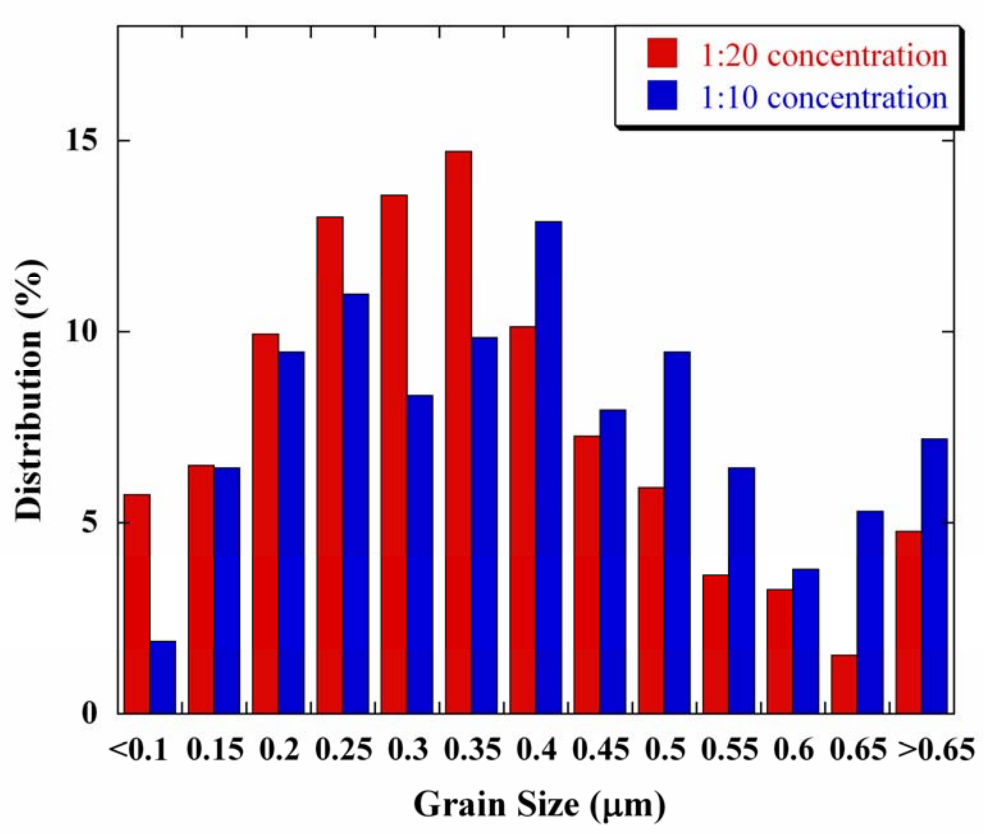

Figure 57. The distribution of grain size of Au films plated in 1:10 and 1:20 dilution plating solutions. The x-axis is the grain size range, e.g. 0.3 means 0.25 < grain size < 0.3. The y-axis is the percentage of the measured data within the various grain size ranges. The total number of measurements was more than 250 in both cases.

According to the bending curvature measurements (see section 5.4), bilayers with thicker Au layers had smaller curvature. In particular, there was relatively little bending for bilayers with Au thicker than 0.3 μm. Unfortunately, preventing delamination required 1 μm thick Au (Figure 55). Hence, plating Au does improve the adhesion, but it cannot create an applicable no-delamination surface for the bilayer microactuators. For macro-actuators with PPy ranging from a few [19] to tens of micrometers [11, 115, 158], using such a thick plated Au layer is workable. In addition, a PPy-based micro-valve is being developed by our group (Figure 58) and other groups [33], which is not based on bending (i.e. in-plane volume change), but on the out-of-plane volume change of PPy. It has been reported the PPy delamination resulted in a short lifetime of the device [33]. As a result, the thick plated Au will be helpful in this kind of application.

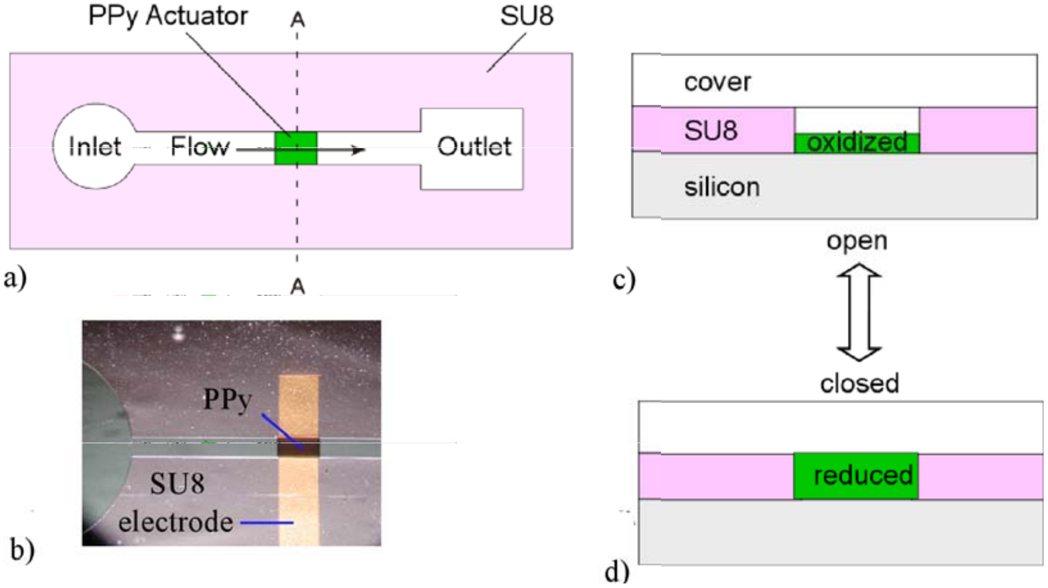

Figure 58. A PPy-based micro-valve being developed in our group. a-b): Top-view of the valve. PPy is deposited into a micro-channel connecting an inlet and an outlet. c-d): When PPy is oxidized and reduced, its volume contracts and expands, which opens and closes the micro-channel. (Courtesy of Nehmiz.)

4.5 Wet Etching Results

Figure 59 shows the delamination of samples with different etch depths. PPy on samples with 5000 and 7000 Å etch depth completely came off before it lost electroactivity. PPy on samples with 2000 and 700 Å etch depth adhered to Au. In particular, only a little bit of delamination, <10%, was seen on the samples with 700 Å etch depth. The delamination was spotty at the edge of the substrate. New samples were fabricated and the cycling and tape test repeated, and the same results obtained. In summary, shallow etch depths, especially 700 Å, greatly increased the adhesion between PPy and Au.

The reason for the adhesion improvement is illustrated by SEM micrographs. Figure 60a-c shows side-view micrographs of samples with 2000, 5000, and 7000 Å etch depths. All the micrographs clearly show the etching is faster along the Au grain boundaries, as the literature has described [151]. The "valleys" seen on the micrographs result from the etching: the grains probably come off from the bulk Au once the grain boundaries are etched through. The "valleys" on the etched Au surface form a larger contact area with PPy than that of the untreated Au surface, which actually helps to improve adhesion (Figure 60d).

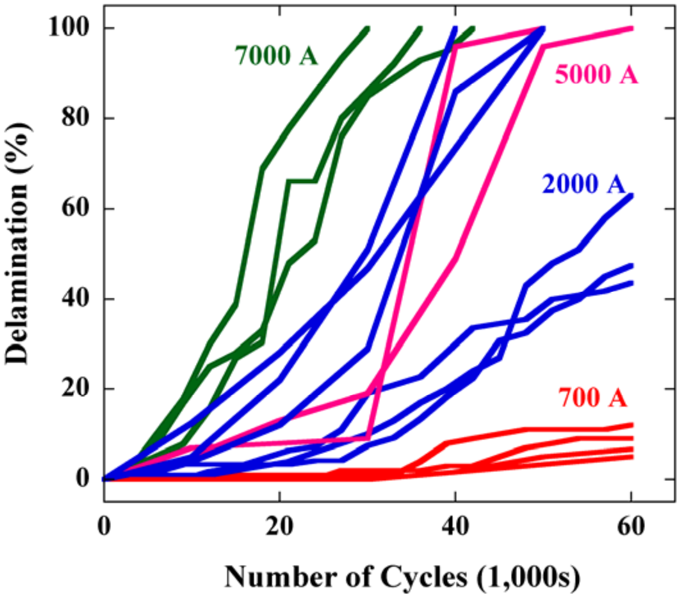

Figure 59. Lifetime curves of wet-etched samples with 4 different etching depths.

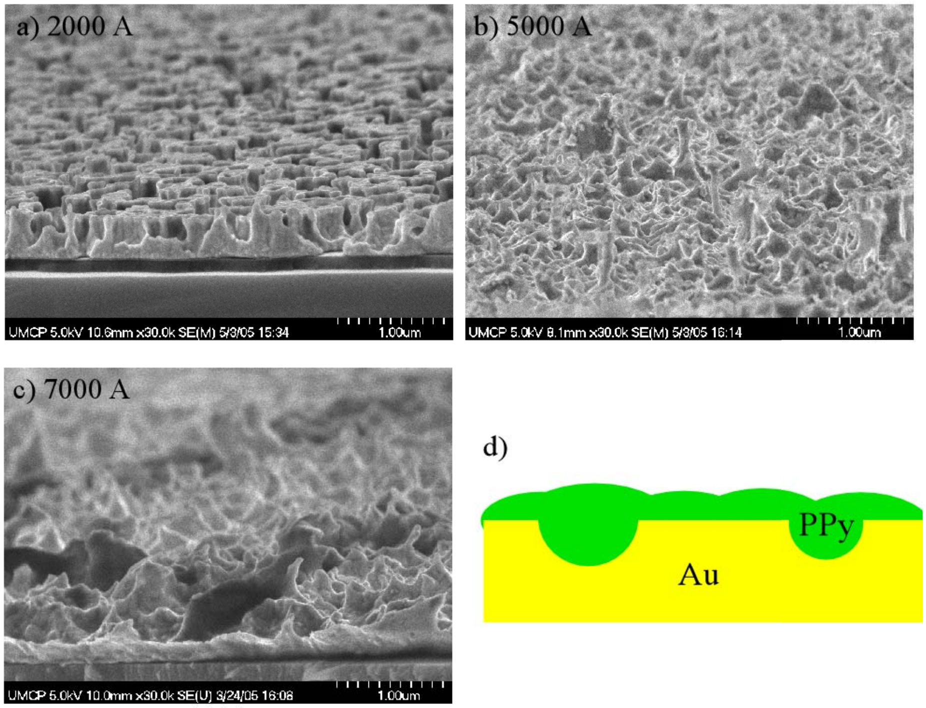

Figure 60. Side-view SEM micrographs of Au surface with a) 2000, b) 5000, and 7000 Å etch depths. All these images show that etching took place quicker along the grain boundaries, which seems to have resulted in grains coming off from the bulk Au. d) Schematic shows the adhesion is improved probably due to PPy growing along the contour of the etched surface and being anchored.

Figure 61a shows a side-view of the samples with 700 Å etch depth. A layer structure is seen, as highlighted by the dashed circles. The corresponding top-view SEM is shown in Figure 61b. In this case, the etching time was shorter than that in Figure 60. The grain boundaries were not completely etched through. As a result, some grains did not come off (Figure 62a-b), which resulted in a layered structure (Figure 62c). PPy adhered more strongly to the layer structure than to the irregular surface of deep etching samples (Figure 60d and Figure 61c), which explains the less delamination on shallow etching samples.

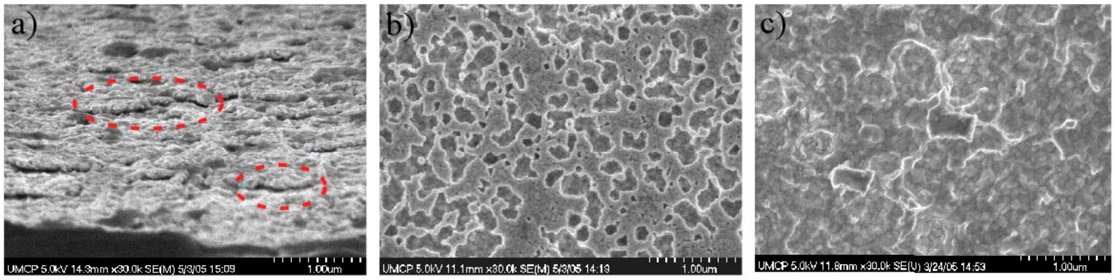

Figure 61. a) A side-view SEM of samples with 700 Å etch depth. The layer structure is highlighted by the dashed circles. b) The corresponding top-view SEM of a). This layer structure was not seen on samples with longer etch times (c), which explains why the adhesion was not strong.

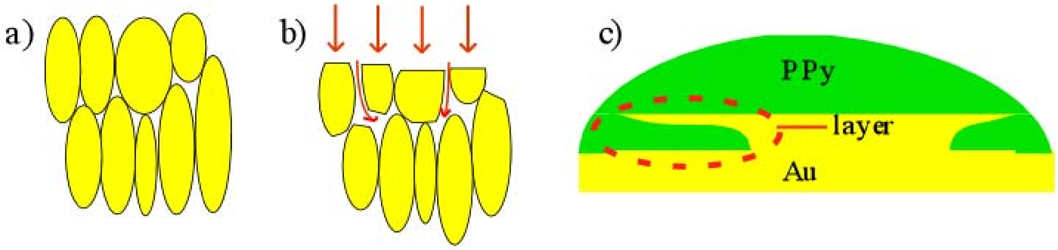

Figure 62. Schematic illustrating the formation of the layer structure during short etch time. a) Au grains are closely packed before etching. b) During a short time etching, the grain boundaries are not completely etched through. Some grains do not come off. As a result, layer structures are created to anchor PPy (c).

Unlike the plating method, the etching method can be used with a thin layer of Au, so this is a useful method for improving adhesion in microstructures. Another advantage of the etching method is the easiness of the process. The plating method requires a very clean surface for Au deposition; fragile structures on micro-devices and microsystems are easy to break during the harsh cleaning procedures. In contrast, the etching method is a simple wet etching procedure. Some possible contaminations on Au can be removed during the etching as well, which will help the deposition of PPy, and therefore the adhesion between PPy and Au. This etching method is compatible with the MEMS process, so it can be easily integrated into bilayer fabrication. For example, photoresist is patterned into bilayers for PPy deposition (see Appendix C); the etching can be conducted next, and then PPy deposited. Furthermore, because the etching takes place on those micro-scale bilayer areas, it will be easier to gain a uniform etching compared to the macro-scale samples. In conclusion, the etching method is a much better method than plating in terms of workability and easiness for MEMS.

4.6 PPy Degradation

As mentioned in the *Introduction*, the lifetime of the PPy/Au bilayer microactuators are limited by both PPy delamination and degradation. As long as PPy strongly adheres to Au during electrochemical cycling, PPy degradation becomes the primary cause. In other words, PPy degradation can only be identified and characterized when there is no delamination taking place. In order to investigate the loss of electroactivity with cycle number, PPy was cycled on untreated Au surfaces (control samples) and etched Au surfaces (700 Å etch depth), 5 samples of each. The cycling was stopped every 10,000 cycles and CVs were recorded (Figure 63). (No tape test was conducted.) In both cases, the areas enclosed by the CV curves, as well as the height of the redox peaks, decrease with cycling (Figure 63). The area enclosed by a CV curve is the total charge exchanged during the electrochemical oxidation and reduction, which is a direct and obvious symbol of the PPy electroactivity, as shown in Figure 64. PPy on the etched surface lost 40% exchanged charge in the first 20,000 cycles, although redox peaks and color change were still observed in Figure 63a and in the experiments. With continued cycling, the loss of the total exchanged charge with cycling almost remains a linear relation. There is still ~ 40% charge remaining after 60,000 cycles. In contrast, PPy on untreated Au lost 50% charge in the first 20,000 cycles. The charge loss stabilized at 80% at 60,000 cycles. Because no tape test was conducted, PPy on both samples was not removed. Hence, the charge loss comes from both degradation and delamination; PPy on the control sample lost more charge than that on the etch sample due to delamination. In summary, the loss of electroactivity with cycle number has been quantified for the first time, which is important because it impacts how the PPy-based actuators can be used. The cycling number at losing 50% exchanged charge can be considered as the lifetime of PPy to determine the biomedical applications for which the actuators are and are not appropriate.

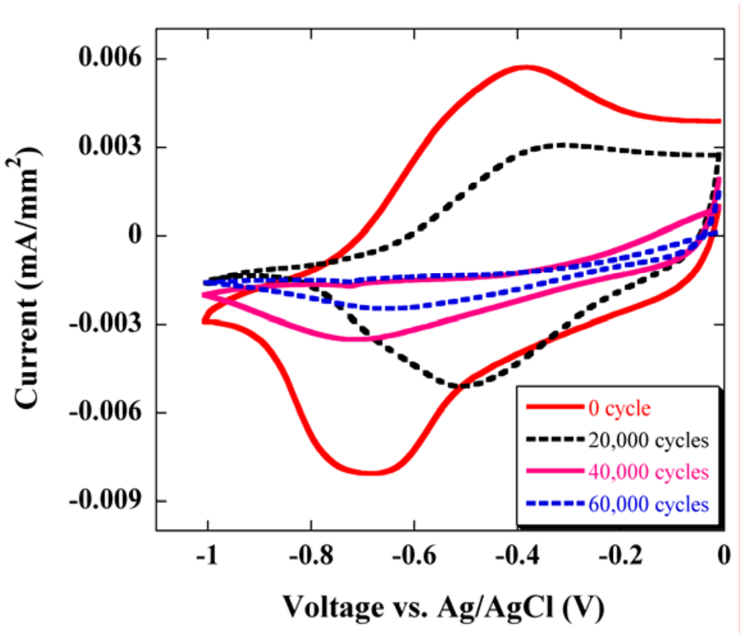

a) CVs of PPy on the etched Au surface before cycling and after 20,000, 40,000, and 60,000 cycles. The total exchanged charge decreases with cycling, showing PPy degrades.

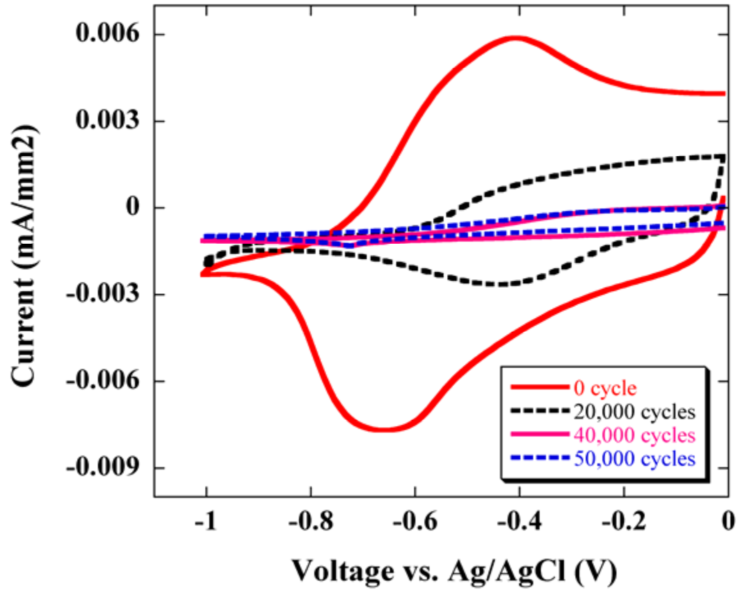

b) CVs of PPy on the untreated Au surface before cycling and after 20,000, 40,000, and 50,000 cycles.

Figure 63. The change of CVs of PPy upon electrochemical cycling.

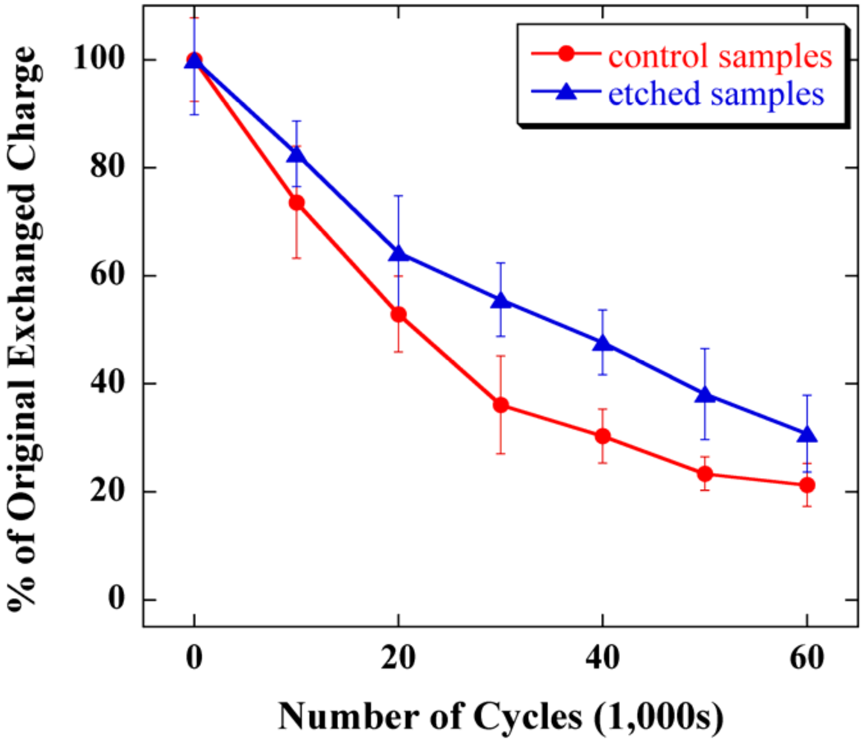

Figure 64. The total exchanged charge of PPy on the control and etched sample upon cycling. Because the adhesion on the etched sample is good, the charge decrease is primarily due to PPy degradation. In contrast, the charge decrease is due to PPy degradation as well as delamination on the control sample.

4.7 Cycling Test on Real Bilayers

There were two key differences between samples in the adhesion test and bilayer bending: the former did not bend and the latter was patterned into micro-scale. Adhesion improvement was therefore tested by plating Au on real PPy/Au bilayers. The bilayer samples were designed and fabricated by Christophersen for characterizing the bending performance; see section 5.3. Au 0.04 µm thick was plated (see top-view SEM in Figure 65b) on 1000 Å structural-Au by using 1:10 concentration and -0.9 V. The bending angle (after 100, 400, and 1,000 cycles) was used as an indirect measure of adhesion. The bending angle did not change after 100 and 400 cycles, but decreased 25-50% after 1,000 cycles (Figure 66). At the same time, delamination was seen, especially at corners where stress was concentrated (Figure 65a). In contrast, the sample without plated Au completely failed after 100 cycles; PPy came off from Au and the bilayers did not bend. Hence, the plated thin layer Au improves the adhesion, although delamination was not prevented with this thin plated Au layer.

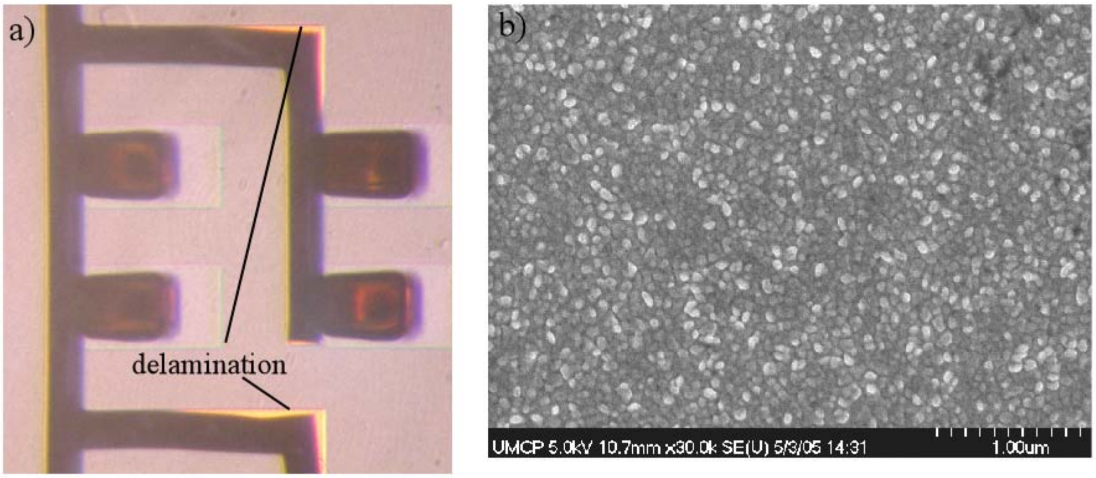

Figure 65. a) PPy came off after 1,000 cycles on a real bilayer-bending sample. b) Top-view SEM micrograph of the Au plated on the sample.

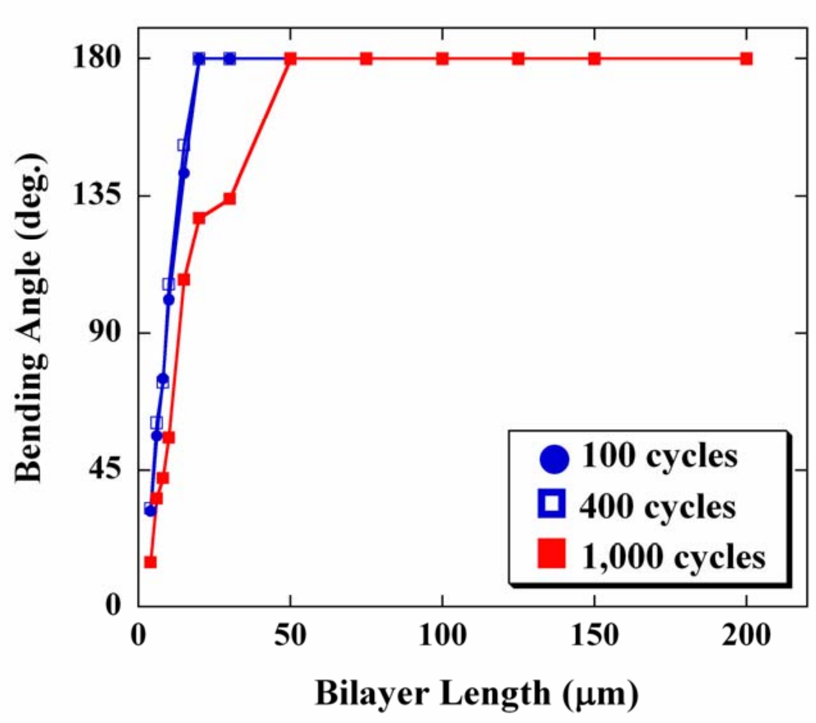

Figure 66. Bilayer bending angles vary upon cycling of an Au plated sample. The bending angles do not change before 400 cycles. After 1,000 cycles, the bending angles became smaller due to delamination. See section 5.3 for the meaning and relation of the bilayer length and bending angle.

Note that the control samples in the adhesion test always showed a lifetime longer than 1,000 cycles, whereas the sample without the plated Au in the test above and in the bending characterization (section 5.4) failed at 100 cycles. The difference may come from the different sample size. The real bilayer sample is micro-scale; any delamination generated will spread so as to quickly affect the whole surface area. In addition, the microfabricated bilayers have greater edge-to-center ratios and sharp corners, at which delamination begins.

4.8 Summary and Suggested Future Work

The Au electrode surface was mechanically modified for improving the adhesion of PPy on Au. The methods employed were electroplating and wet etching. Compared to the chemical methods introduced in literature, the mechanical methods are easy to perform and are compatible with MEMS processes. An experimental setup and a methodology were developed to test adhesion upon extended cycling, which is required for real applications of most PPy/Au bilayer actuators.

Adhesion was significantly improved by depositing a layer of electroplated Au on smooth Au surfaces, as well as by etching a layer from the Au surface. The lifetime was extended by tens of thousands of cycles, and the delamination mode was changed to prevent catastrophic failure. In particular, samples with a 1 μm thick Au layer plated from a low concentration solution and samples with a shallow etch depth of 700 Å did not show delamination before PPy lost electroactivity. Because the original Au morphology deposited by different apparatus and batches varied significantly [10], these specific operation parameters maybe not stay unchanged. However, SEM micrographs illustrated the morphologies of surfaces with good adhesion, which will provide guidance for repeating the experiments and results. These surface-roughening methods are not limited to the usage only with PPy and Au. Indeed, they can also benefit a wide range of other conjugated polymer devices including electrochromic display [159, 160] and supercapacitors [161-163].

The no-delamination Au surface also facilitated the investigation of PPy degradation upon electrochemical cycling. The change of the shape of CVs and the corresponding total exchanged charge showed that PPy lost 40% of its original electroactivity after 20,000 cycles, which helps future users to understand the lifetime of PPy-based devices in aqueous electrolytes, and therefore the feasibility of their use in a specific biomedical application.

Chapter 5 Polypyrrole/Gold Bilayer Bending Angle

5.1 Background and Problem Statement

In order to turn the concept of PPy/Au bilayer microactuators into real applications, the designer must know the material properties and performance metrics. Among the metrics, the bending performance is the key issue, which is determined by both the material properties and the geometry of the bilayers. Previously, bending curvature [11, 19] and Young's modulus [22, 23] were measured using macro-scale bilayers with PPy thicker than 10 μm. On the other hand, existing models [120] fail to predict the correct behavior of microactuators, in part because 1) there is a strain gradient in the PPy arising from the electrodeposition process [18]; 2) during actuation, the Young's modulus of the polymer varies [23]; 3) the modulus of PPy has only been measured for thicker films [23]; 4) the morphology of the PPy changes with thickness [121]; and 5) the properties of the PPy may be affected by the microfabrication process. Therefore, experimental data are required to characterize the bending performance of the PPy/Au bilayers. This chapter focuses on curvature measurement, and the next chapter on force.

PPy/Au bilayer microactuators are important components in the cell-clinics system. Their bending performance not only affects the design, but also determines whether the microsystem can work properly. In the cell-clinics, the bilayers must be able to rotate lids to open and close the cell-holding vials (Figure 11 in section 2.5). In order to encage and isolate cells for measurement, the bilayers must rotate the lids so that they can lie flat on the vial surface and fully cover the vials. Figure 67a shows an unsatisfactory bilayer: the lid only covered part of the vial. To close properly, the diameter of the bent bilayer should equal the sum of the height of the vial h and the thickness of the lid t, Figure 67b. (The thickness of the Au is much thinner than h or t, so it is neglected.) Hence, the diameter d determines the thickness of the vial and the lid, and furthermore the material (different types of SU8 generate layers with different thickness ranges) and fabrication parameters (the thickness of SU8 within a range results from the spinning rate) to be employed. The diameter also affects the design of the microstructures by determining the relative positions of the vial and the bilayer (Figure 12 in section 2.5). In addition, the closed lids might not be tight enough for electrical isolation. Other techniques, such as using a magnetic force, may be required to facilitate sealing the vials. In this case, the PPy/Au microactuators need to exert enough force to open the vials. Therefore, the PPy/Au bilayers need to be characterized in terms of the bending curvature and bending force.

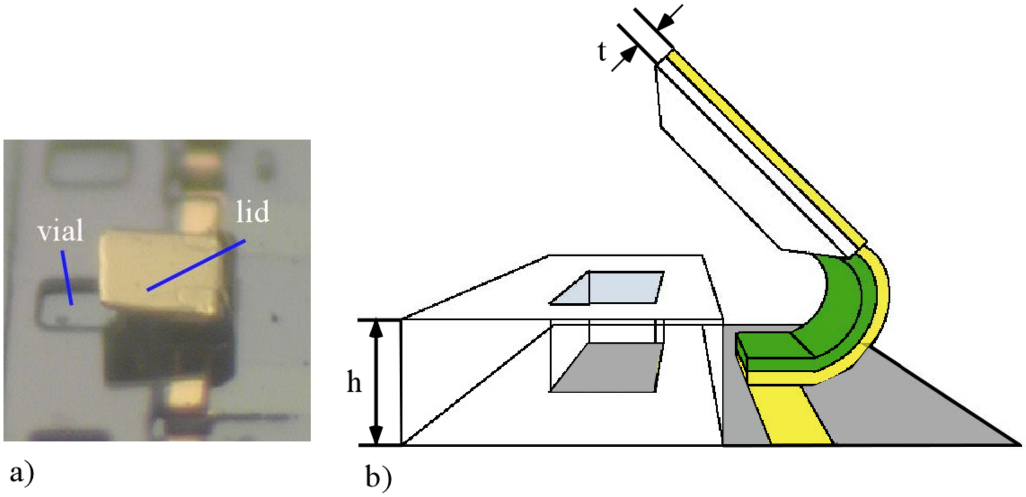

Figure 67. A lid will lie flat over a vial when the bilayer bending diameter equals the sum of the height of the vial *h* and the thickness of the lid *t*. a) A side-view photo of an actual bilayer bending and b) a schematic of bilayer bending.

The bilayer bending performance is determined by both bilayer geometric parameters (dimensions, configurations, and layer thicknesses) and component layer mechanical properties. Simple models predict that there is a ratio of PPy to Au thickness at which the bending curvature (*1/r*, *r* is the radius of the bending bilayer) is maximum [164], whereas the force simply increases with PPy thickness (Figure 68). The layer thickness must therefore be properly designed: the minimum PPy thickness is determined by the required force, with greater thickness negatively impacting speed; the gold thickness is then set by the PPy:Au ratio that gives the diameter *d* of the bending bilayer. In this chapter, a comparison between the experimental data and the simple model is described, which resulted confirmation of the existence of strain gradients in the conjugated polymer film.

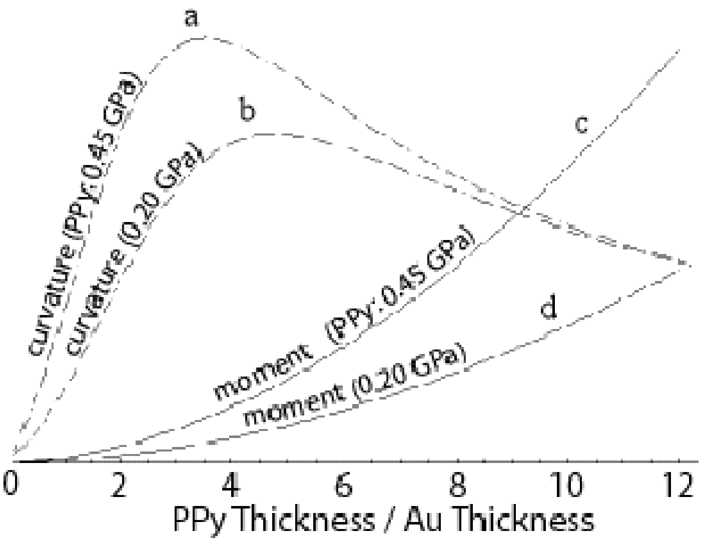

Figure 68. Predicted bending curvature (a-b) and moment (c-d) as a function of PPy:Au thickness ratio. The curvature and moment values are normalized with respect to bilayers of the unit width. Different Young's modulus of PPy, 0.2 and 0.45 GPa, are used to show the changing trend of curves. (Courtesy of Fanning and Sharpiro [165].)

5.2 Experimental Methods

Bilayers under an applied 0 V voltage were imaged directly by a digital camera (Coolpix^{TM} 4500, Nikon Inc., Japan) attached to a microscope (MZ 125, Leica Inc., Germany), Figure 69. The projection of the plates, Lp, was calculated by using the width of the electrode (50 μm) as a reference dimension, equation (8). When the bending angle α was smaller than 90° (Figure 70b), α was calculated by using Lp and the plate length Ld that was known from the design, equation (9). Furthermore, the bending radius r and curvature κ ($\kappa=1/r$) were obtained by using α and the bilayer length L, equation (10). The calculation of α, r, and κ was similar when α was larger than 90°, see Figure

70d.

(8) $$L_p = \frac{50 \times plate-on-photo}{electrode-on-photo}$$

plate-on-photo: the plate width measured on the overhead photo(e.g. Figure 70a and c) by using drawing software (Canvas, version 7SE, ACD Systems Inc., Canada).

electrode-on-photo: the electrode width measured on the same overhead photo with the plate width.

(9) $$Cos\alpha = \frac{L_p}{L_d}$$

(10) $$r = {}^{1}\!/_{\kappa} = \frac{L}{\alpha}$$

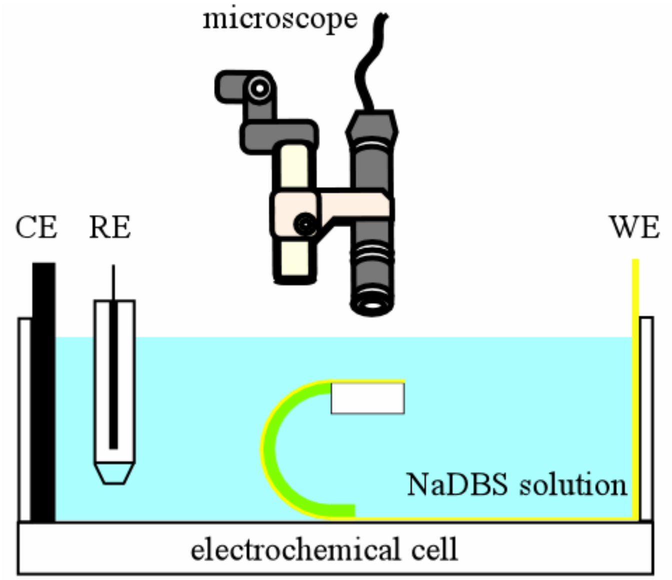

Figure 69. Schematic of the experimental setup to measure curvature. The bilayer is placed in a three-electrode electrochemical cell. The curvature data are calculated from overhead photos taken through a microscope.

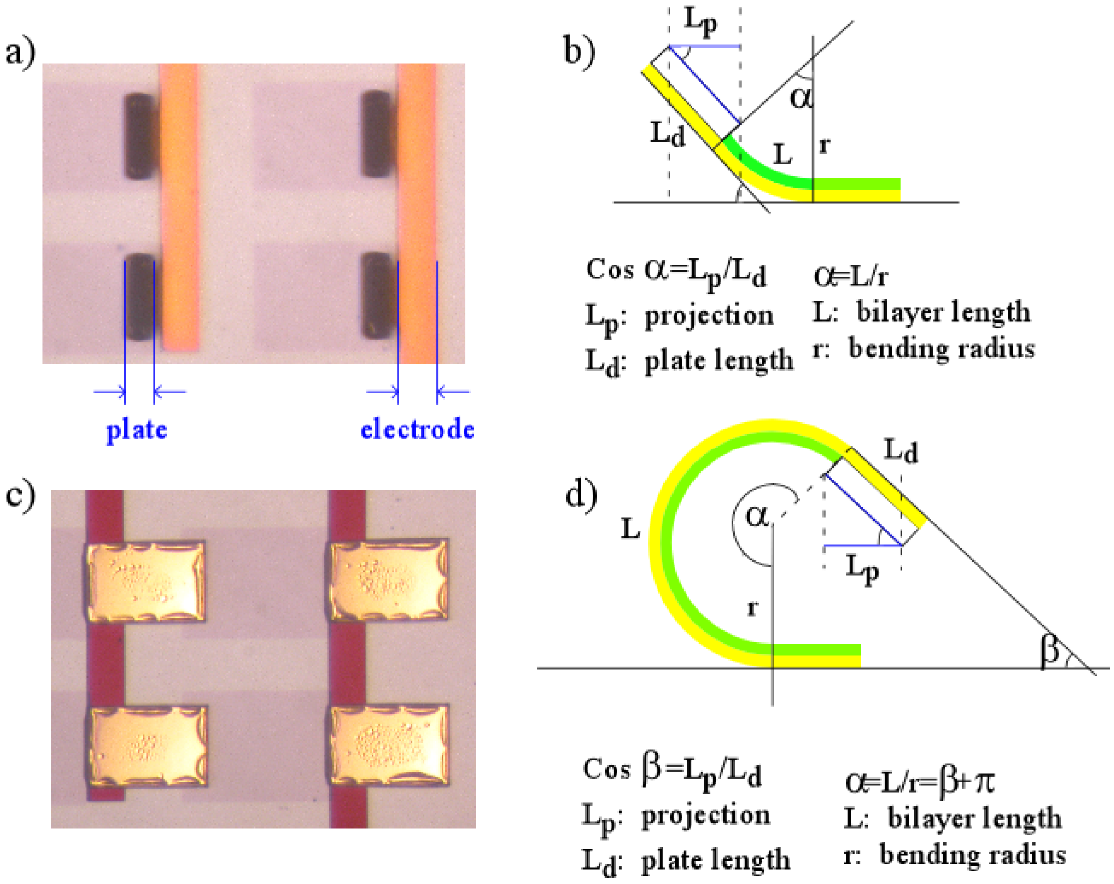

Figure 70. The bending angle and curvature were calculated by using the projection of the plates. The electrode width was 50 μm. By comparing the plate projection and electrode width on the overhead photos, the plate projection L_P is obtained. Then, the bending angle α and radius r are calculated by using geometry.

An attempt was made to visualize bending angles directly so as to obtain curvatures. In order to take photos when bilayers bent, a digital camera (Coolpix^{TM} 990, Nikon Inc., Japan) attached to a microscope (Z16 APO, Leica Inc., Germany) was placed at an angle (around 45 °) with respect to the substrate surface of bilayers (called angle-view, Figure 71). The microscope was placed on a boom stand, which enables five degree-of-freedom positioning. The sample was illuminated by a light source (ACE$^{®}$I, Schott Inc., Southbridge, MA).

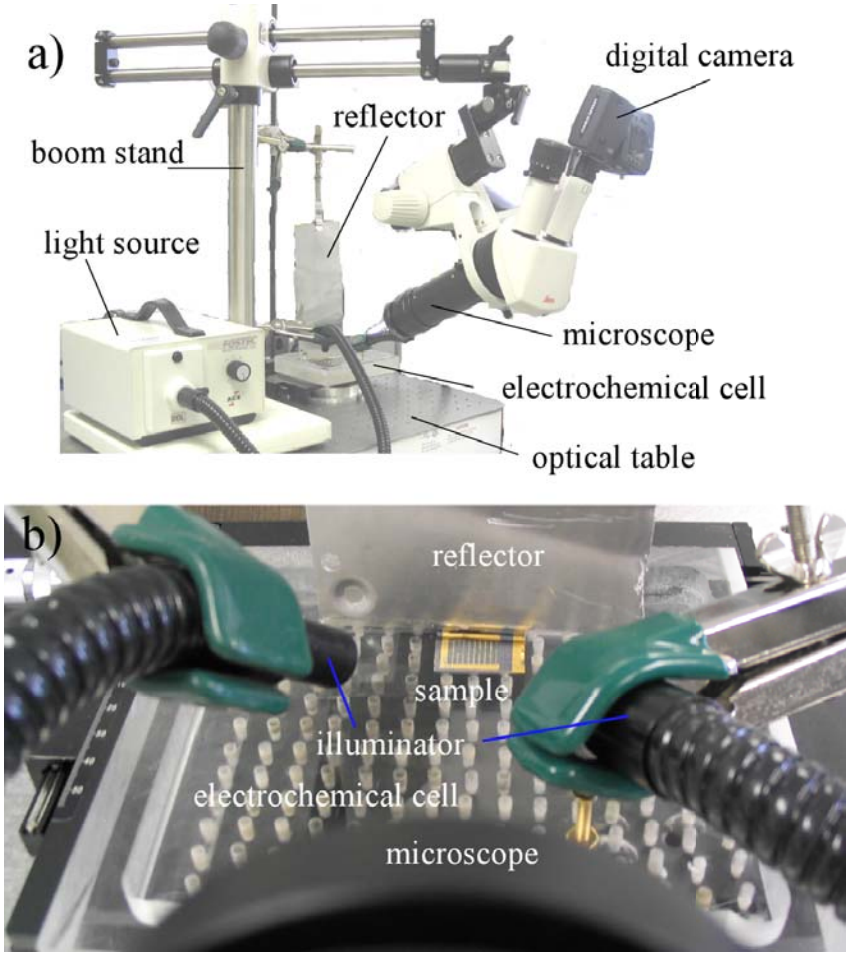

Figure 71. a) An overview of the angle-view setup comprising microscope, digital camera, light source, boom stand, scatter, and electrochemical cell. The whole setup was placed on an optical table to reduce vibration. b) A close-view of the setup. The sample was placed in the electrochemical cell and immersed into the solution. Light was scattered by an Al plate to illuminate the tiny bilayers. Photos were taken through the microscope. (Courtesy of Chin.)

Several problems arose during the measurements. 1) Bilayers could not be focused because any small vibration on the laboratory desk was amplified by the high-magnification microscope system (object piece × 9.2, eyepiece × 10, and camera × 3). Hence, the whole setup was put on an optical table to reduce vibration. 2) When the sample was immersed into the NaDBS solution, the light was absorbed by the solution, which resulted in a poor lighting on the sample. An aluminum plate was employed as a reflector that light from two illuminators was scattered and shone the whole bilayer. At the same time, the solution added into the cell was remained as shallow as possible to reduce the traveling distance (and the absorption) of light in the solution; the sample was kept only tens to hundreds micrometers under the liquid surface. The depth was enough for the bilayers to move during the bending procedure. The method of placing the microscope straight to the sample (Figure 72) was given up because this method resulted in the longer traveling distance and poor lighting that even the reflector could not help.

Figure 73 shows the clearest image of a bent bilayer bilayer we could get. The photo was still blurry. In particular, it was difficult to identify the contour of bilayers for measuring the angle due to the shadow. It was also very time-consuming to adjust illumination for a clear image, about half an hour for one bilayer. As a result, overhead photos were used instead of the angle-view photos.

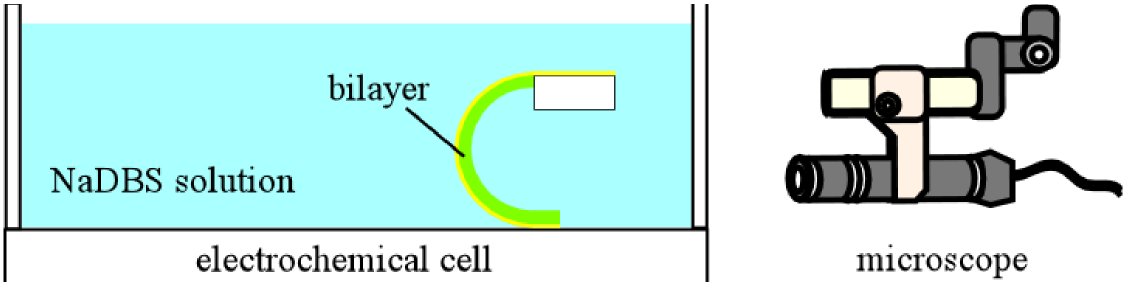

Figure 72. Schematic of taking bending photos by placing the microscope straight to the sample.

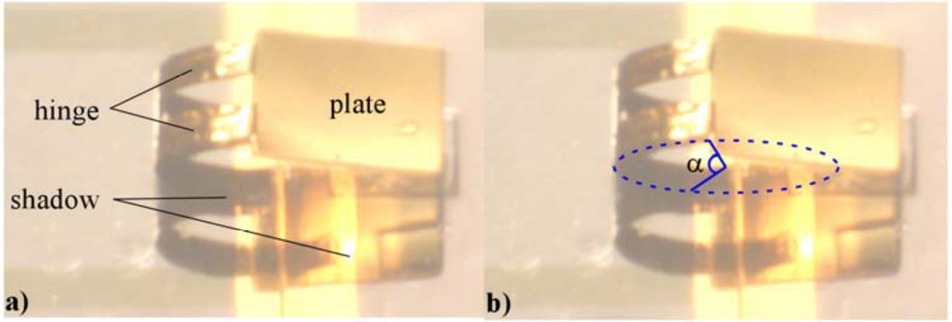

Figure 73. Angle-view photo of a bent bilayer. a) The clearest image we got by using the reflector. b) The bending angle α is determined according to the contour of the bilayer.

5.3 Bilayer Design

In developing the fabrication process for the cell-clinics (see Appendix C), arrays of PPy/Au bilayers with 10 μm thick SU8 vials and plates were fabricated using low-cost transparency masks. These bilayers were used not only to test the process, but also to test the bending performance. The lengths of the bilayer bilayers were 50, 70, 130, 180, 230, and 280 μm. All the bilayers had the same width of 100 μm (Figure 74).

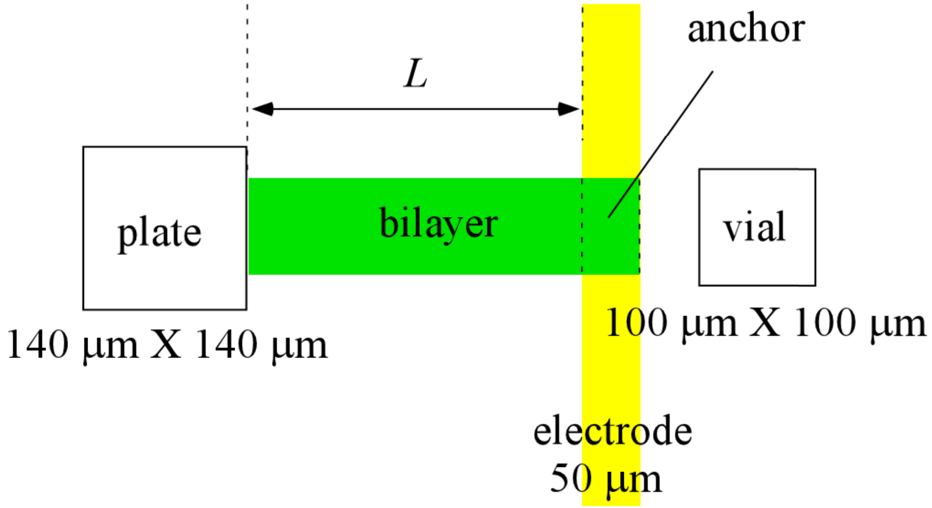

Figure 74. Size and dimensions of bilayers for rough design screening.

Using these samples, the design of the bilayers was roughly screened (Figure 75). Vials could not be fully covered by bilayers shorter than 130 μm, but bilayers longer than 130 μm twisted. Twisting is related to aspect ratio (length/width) of bilayers [166]: short bilayers with aspect ratio less than 1 demonstrated normal bending. Large errors occurred when curvatures were calculated even by using photos of not-twisted bilayers. The errors came from a number of sources. 1) Blurry photos. According to Figure 70, clear images of both plates and electrodes were required for an accurate calculation. Because plates and electrodes were not on the same plane, the camera did not focus on them at the same time. It was worse when the magnification was high due to the greater loss of focus depth. A compromise had to be made to reduce magnification for a larger focus depth, zooming-in by using software to process photos for compensating the lower magnification. 2) Photolithography masks. The masks were the low-cost transparency masks, which had around 10 μm dimension error. In order to systematically investigate the bending behaviors of bilayer bilayers with different dimension, a high-resolution

Cr/glass mask had to be employed (see Appendix F for details). 3) In order to reduce errors coming from random variation in fabrication and measurement, enough redundant devices had to be fabricated and measured simultaneously. As a result, the bilayers were redesigned by me and Dr. Christophersen (a postdoctoral fellow in our group).

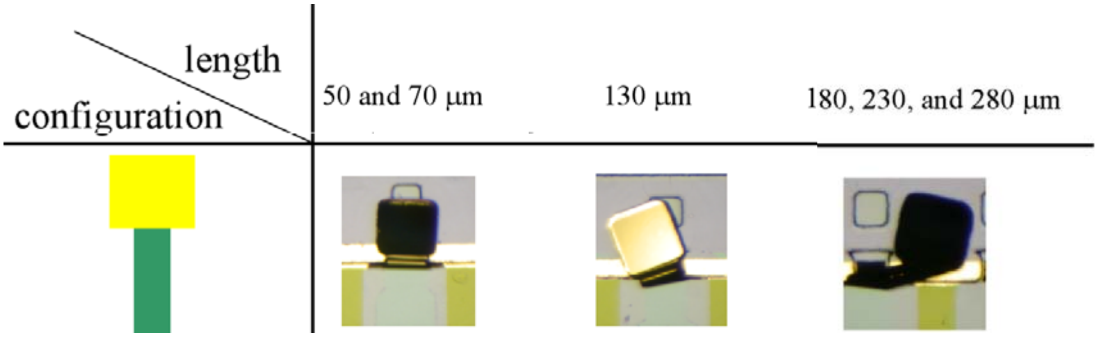

Figure 75. Top-view bilayer bending performance in terms of bilayer dimensions and configurations: short bilayers could not fully close vials, while longer ones twisted.

Several aspects were involved in the new design of bilayer bilayers. 1) Aspect ratio of all bilayers was less than one (Figure 77). For bilayers shorter than 10 µm, their width was 40 µm. The width of the other bilayers was 4 times their length (Table 3). 2) Bilayers with a series of lengths were designed. The bilayer was expected to bend in a circle, which was verified by a photo taken from a side-view (Figure 76a). As a result, bilayers with different lengths would bend to different angles but have the same curvature (Figure 76b-c). By measuring a series of bilayers, the average curvature was calculated to reduce measurement errors. 3) The high-resolution Cr/glass mask (±1 µm dimension error) was employed in photolithography. 4) There were around 3,000 bilayers drawn on the mask. This large number of bilayers was fabricated simultaneously to minimize variations from fabrication. In practice, Dr. Christophersen made around 30 wafer quarters with different PPy:Au thickness ratios (up to 9 ratios) and structural-Au thicknesses (500, 1000, and 2000 Å). Bilayers on each wafer quarter had a specific PPy:Au thickness ratio and structural-Au thickness (Figure 78); more than 90% bilayers bent normally. 5) SU8 plates connected to the bilayers were 150 μm long, and their width was 20 μm wider than the bilayers (Figure 77). The objectives of including the SU8 plates were to keep the bilayers from bowing during bending, helping to enable the curvature measurement (Figure 79). The plates also magnified the displacement (Figure 80). In addition, the plates enabled force measurements (see Chapter 6).

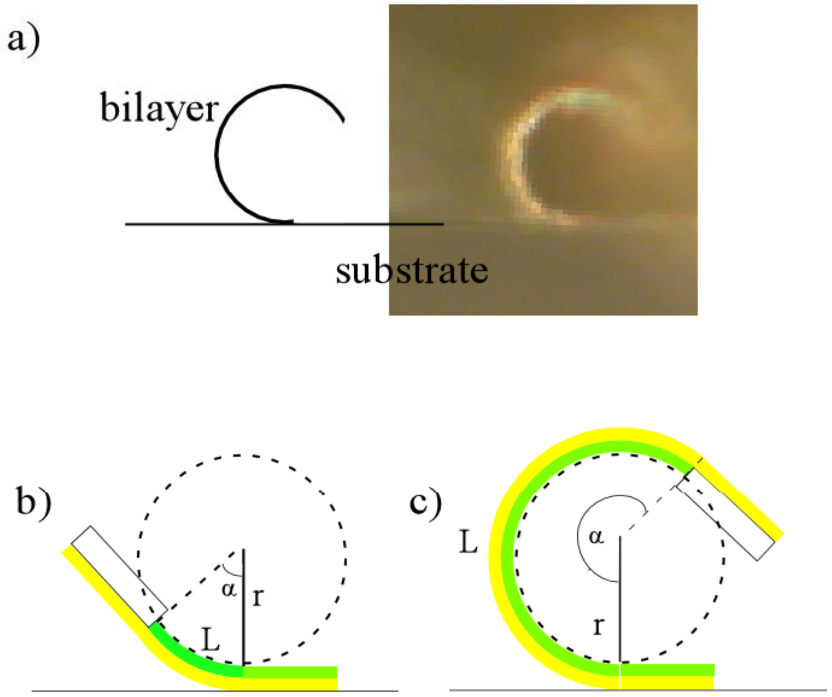

Figure 76. The bilayer bends in a circle, which is verified by the photo (a, courtesy of Christophersen) taken from the side. As a result, bilayers with different lengths will bend to different angles but have the same curvature (b-c).

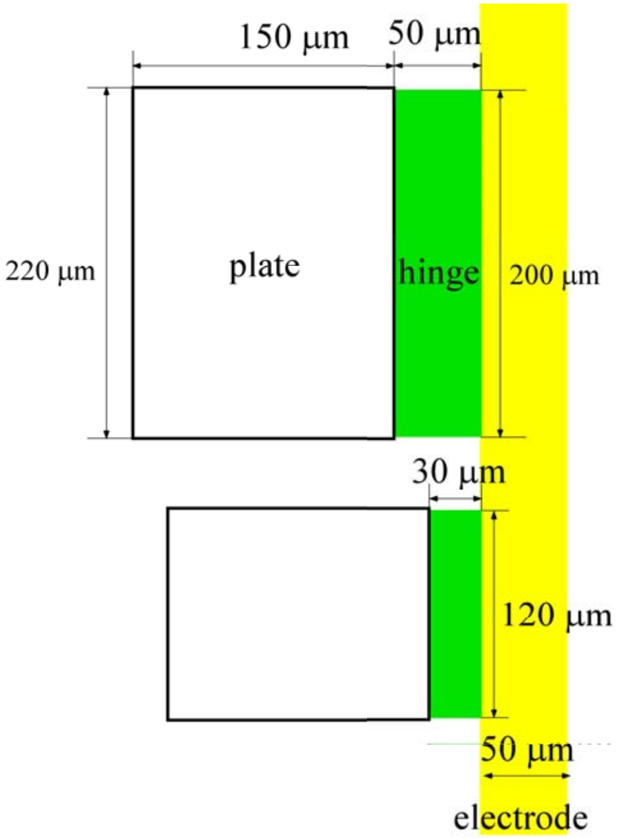

Figure 77. Dimensions of the redesigned bilayers with aspect ratio less than 1.

Table 3. Dimensions of the bilayers for curvature measurement.

Bilayer Length (µm)	4	6	8	10	15	20	30	50	75	100	125	150	200
Bilayer Width (µm)	40	40	40	40	60	80	120	200	300	400	500	600	800
Plate Width (µm)	60	60	60	60	80	100	140	220	320	420	520	620	820

Figure 78. Overview of the sample for bending measurement. There are around 3,000 bilayers on a wafer quarter. All the bilayers have the same PPy:Au thickness ratio, but different bilayer dimensions. (Courtesy of Christophersen.)

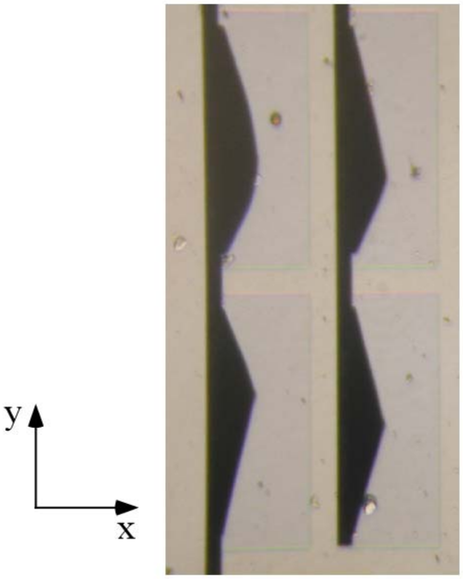

Figure 79. When PPy(DBS) is oxidized, its volume contracts in both x and y directions, so bilayers without plates bowed. (Courtesy of Duerkop.)

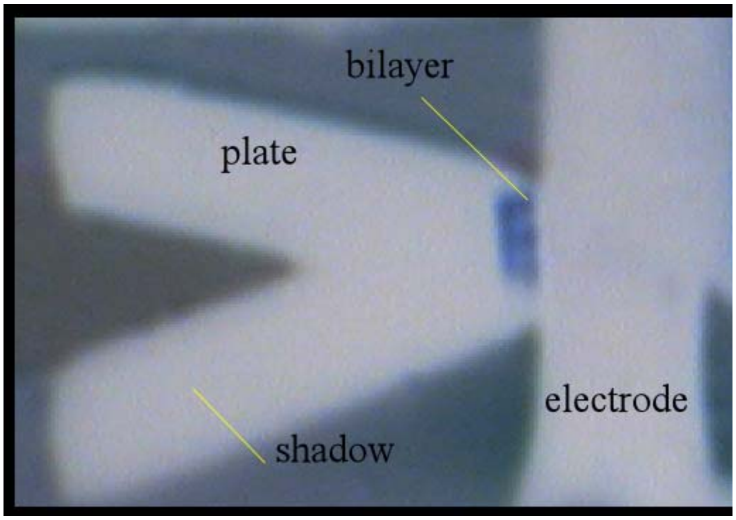

Figure 80. The rigid SU8 plate is used to help the measurement by enlarging the displacement.

5.4 Results and Discussion

Figure 81 shows the bending angles of bilayers with 1000 Å thick structural-Au and 10:1 PPy:Au thickness ratio. The bending angle increased linearly with the bilayer length up to 180°, as expected. When the bilayers were longer than 50 μm, they bent more than 180° and the plates touched the substrate, which made further bending impossible. Based on the equation (10), the curvature κ of bilayers of different length was calculated. The average and the standard deviation were 0.074±0.006 μm^{-1}. The curvature of bilayers with other PPy:Au thickness ratio are plotted together in Figure 82, showing how κ varies with the ratio. The curvature shows a maximum at 5:1, and then decreases. (Maximum curvature means minimum bending radius r.) In other words, a bilayer with a fixed length and a larger curvature will have a larger bending angle α.

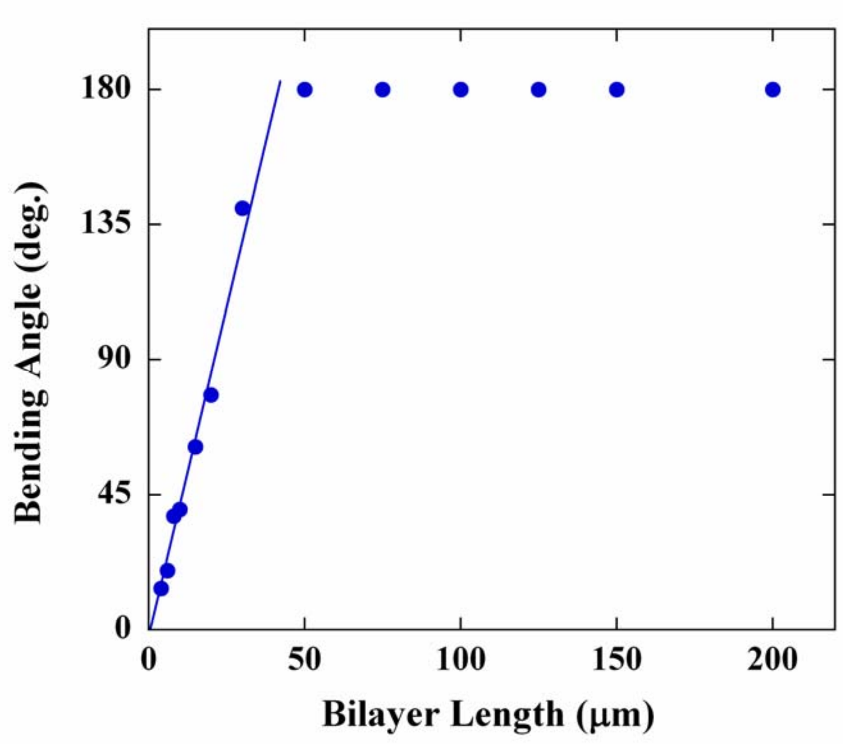

Figure 81. Bending angles vs. bilayer length. The bilayers had 1000 Å thick structural-Au and 10:1 PPy:Au thickness ratio. As expected, the angle increased linearly with bilayer length. When the bilayers were longer than 50 μm, they bent more than 180° and the plates touched the substrate, which made further bending impossible. The average and standard deviation of κ for this sample are $0.074 \pm 0.006\ \mu m^{-1}$.

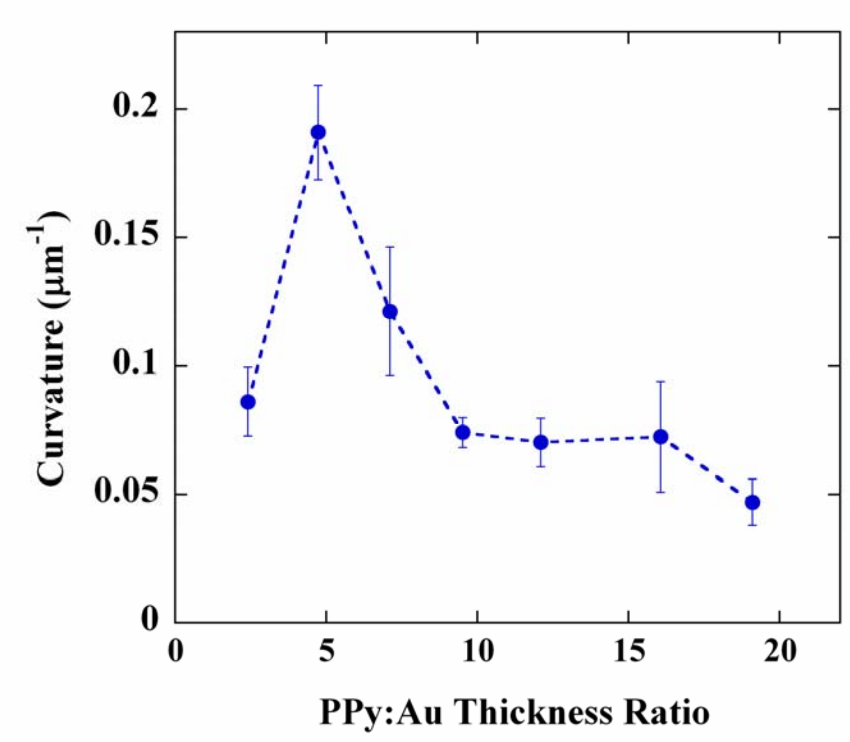

Figure 82. Curvature κ vs. PPy:Au thickness ratio. All the bilayers have 1000 Å thick structural-Au. The curvature increases to a maximum at 5:1 and then decreases.

When the curves for different structural-Au thicknesses were plotted together (Figure 83a), all three curves had a similar shape: the curvature increased to the maximum at 5:1, and then decreased. At the same time, the figure shows that bilayers with the same PPy:Au thickness ratio but thinner structural-Au had larger curvature. It is because both PPy and Au layers resists bending. Bilayers with the same thickness ratio but thinner structural-Au have a smaller total thickness of PPy and Au. Therefore, they are easy to bend.

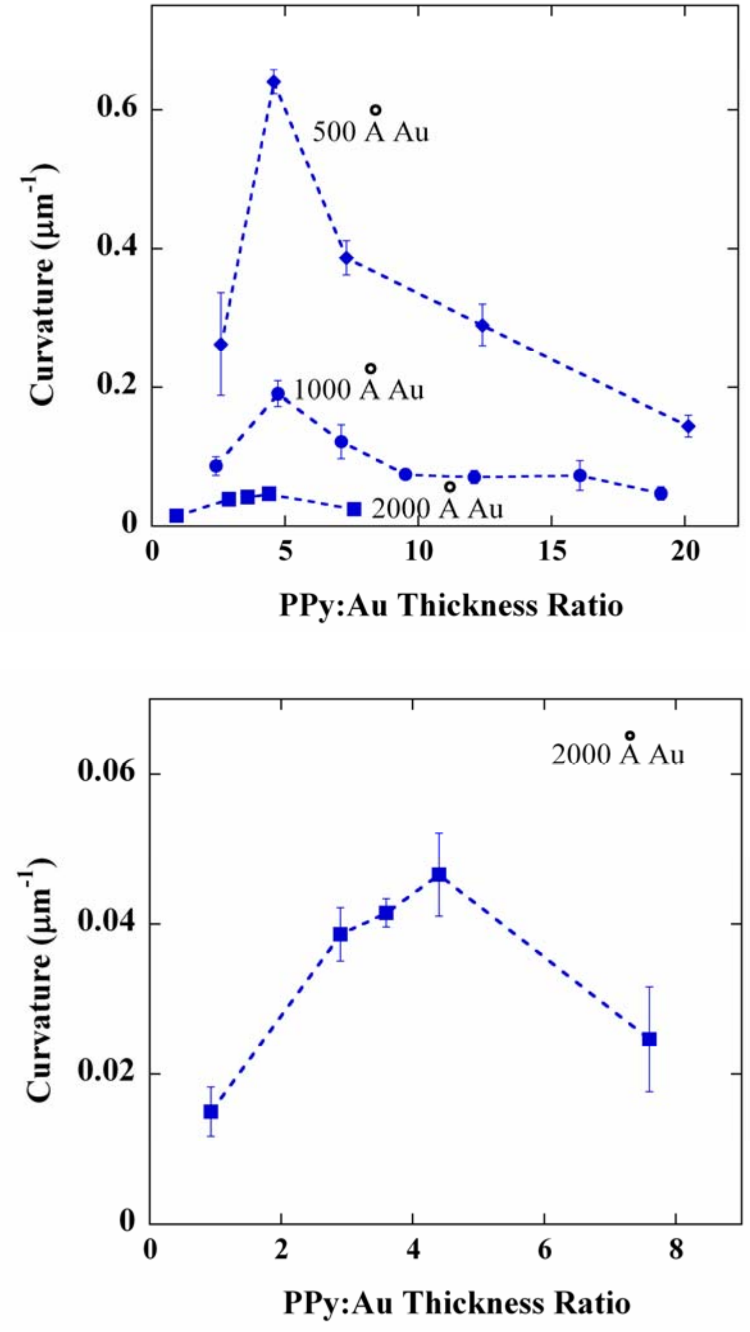

Figure 83. **Curvature κ vs. PPy:Au thickness ratio of bilayers with different structural-Au thicknesses. All three curves show a similar shape: the curvature increases to a maximum at 5:1, and then decreases. Bilayers with the same PPy:Au thickness ratio but thinner structural-Au show larger curvature.**

As mentioned in the *Introduction*, bilayers in the cell-clinics are required to actuate lids to lie flat (α=180°) at 0 V, as well as rotate at least 90° to open vials at -1 V. In practice, all the bilayers rotated more than 90°. So we only consider choosing a bilayer with 180° bending angle, and do not need to worry whether vials can be properly opened.

5.5 Modeling

This section briefly introduces the work of developing a model for bilayer bending. Timoshenko [164] developed a model based on pure bending of beams to describe bi-metal thermostats. Considering the similar situation of PPy/Au bilayer bending, his model was used as a starting-point. The assumptions of the Timoshenko model include 1) the bending radius *r* is much larger than the layer thicknesses, 2) the deformation is within the elastic regime, i.e. linear relation of stress and strain, 3) Young's modulus and strain are constant through the thickness of layers, 4) the layers are isotropic along the directions of length and width, and 5) no external force exists. The Timoshenko equation is expressed as:

$$\textbf{(11)} \qquad \frac{1}{r} = \kappa = \frac{(\alpha_1 - \alpha_2)}{h_2} \frac{6mn(1+m)}{1+4mn+6m^2n+4m^3n+m^4n^2}$$

where the PPy layer is denoted as 1, and the Au layer as 2.

α: in-plane strain. (Because Au does not change volume during electrochemical redox, α_2=0.)

h: thickness. $m = h_1/h_2$.

E: Young's modulus. $n = E_1/E_2$.

Curvature κ was calculated and compared to validate this model. Literature values were reported as E_1 0.45 GPa [23]), E_2 from 53 [167, 168] to 78 GPa [169] for thin film Au, and α_1 from 0.35% to 3.6% [19, 23].

Figure 84 shows how the modeling curves vary with α_1 and n. Curvature greatly increases with strain α_1, while n changes the curve shape. Curvature becomes larger with n, and the peak moves to the left side.

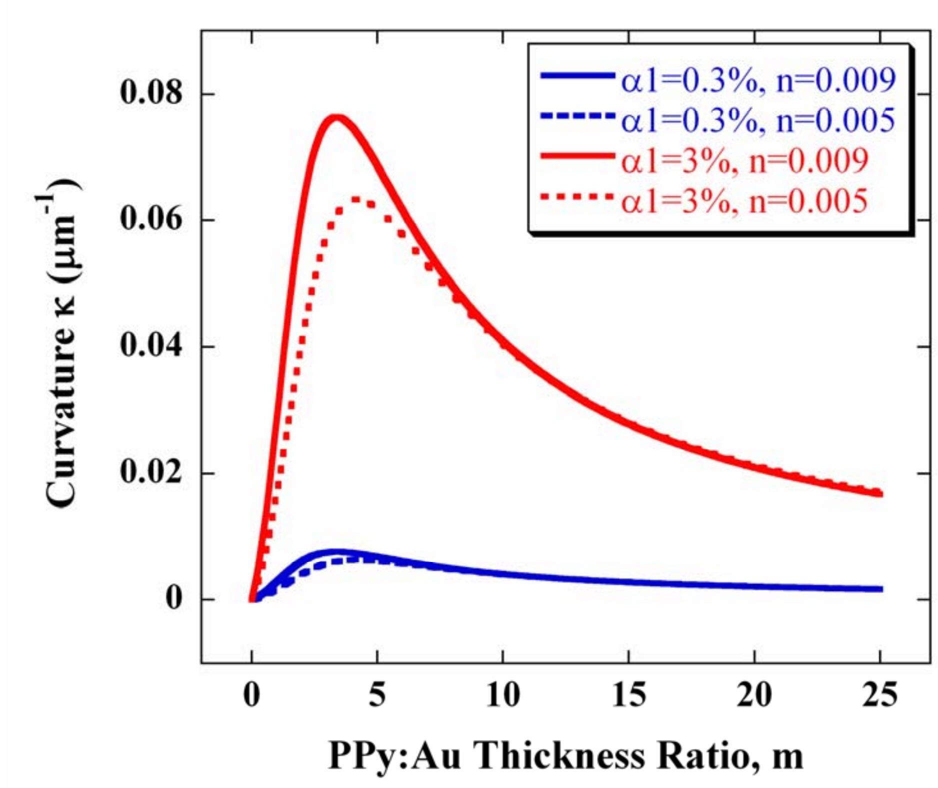

Figure 84. **Effects of strain α_1 and modulus ratio n on shape and magnitude of modeling curves. Curvature increases with strain. The PPy:Au thickness ratio showing the maximum curvature moves to the left side with larger modulus ratio.**

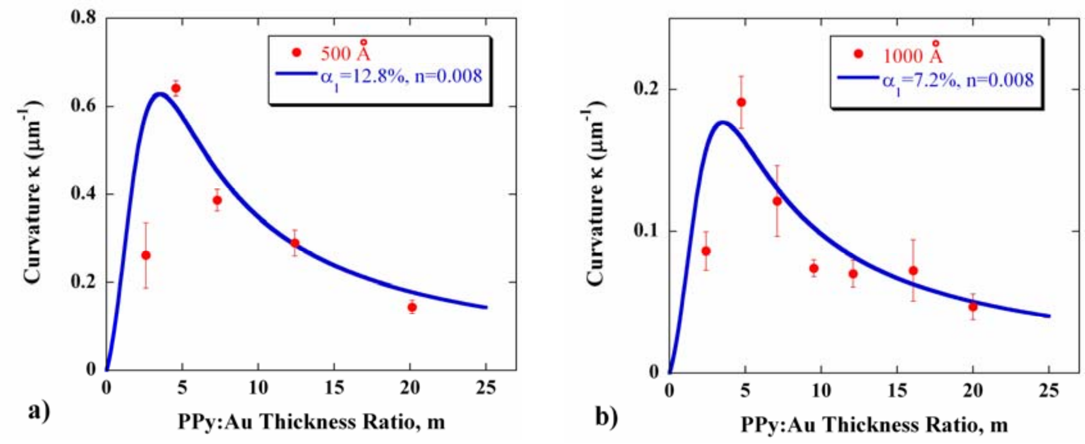

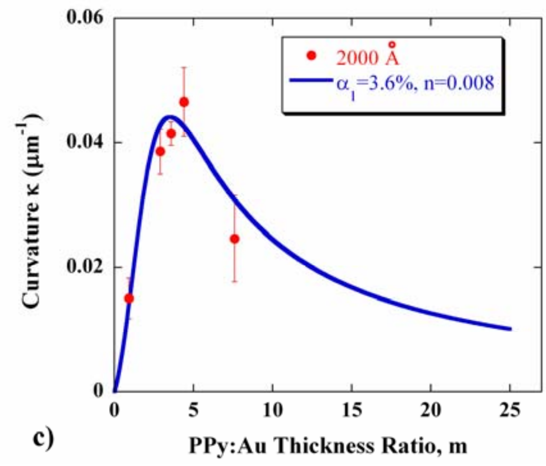

Figure 85. A good fitting was obtained by applying a larger strain to thinner structural-Au. Modulus ratio of 0.008 was taken by employing E_1 of 0.45 and E_2 of 56 GPa.

By changing α_1 and *n*, the modeling curves were adjusted to fit the experimental data. A good fit could not be obtained for data with 500, 1000, and 2000 Å thick Au simultaneously by applying a constant strain α_1 to all the modeling curves. As shown in Figure 85, a reasonable fit was, however, achieved when strains of 12.8%, 7.2%, and 3.6%, were used, respectively. Note that the average thickness of PPy from *a)* to *c)* in Figure 85 increased. As a result, it is reasonable to propose that thicker PPy layers generate a smaller strain. In other words, a strain variation exists along the thickness of PPy.

Previous work has shown the properties of PPy(DBS) are anisotropic along the thickness [121, 170]. In particular, it has been reported that the volume change, which determines in-plane strain, varied with the PPy thickness [170]. It was probably due to more crosslinking or defects at PPy layers close to the Au interface resulting from electrochemical deposition. By fitting the experimental data, the existence of strain gradient in PPy was verified, as well as calculated for the first time. The existence of strain gradient also explains why the Timoshenko model did not work to account for the experimental data of bilayers: the Timoshenko model assumes a constant strain through the layer thicknesss. Prof. Shapiro (Aerospace Engineering, UMCP) and Prof. Smela (Mechanical Engineering, UMCP) built a mathematical expression of the strain gradient to replace the constant strain in the Timoshenko model; see the full paper [171] for details. On the other hand, the same *n* of 0.008 was used in all three modeling curves. Therefore, there are no significant modulus gradients in the film.

5.6 Summary and Suggested Future Work

In this chapter, PPy/Au bilayer microactuators with a range of dimensions and configurations were designed and fabricated to enable bending curvature measurement. Bilayers with a fixed PPy:Au thickness ratio show a specific curvature. As the PPy:Au thickness ratio increases, the curvature first increases and reaches a peak around 5:1 PPy:Au thickness ratio, and then decreases. The thicker structural-Au in the bilayer resisted bending, which generated smaller curvature. The experimental data were measured for the first time, which fills the blank in the data for metrics of bilayer microactuators, and will benefit future designers and possible applications.

A simple model based on classical beam theory was introduced to describe the bending behavior of bilayers. To fit the experimental data, we confirmed that a strain gradient exists in the PPy. Actuation strain is smaller with PPy closer to the Au interface, which results from electrochemical deposition. Prior work on modeling bilayer bending failed due to neglecting this PPy strain gradient. On the other hand, the fitting shows that there are no significant modulus gradients in the film.

For cell-clinics, the curvature data allow easy variation of the design of the cell-culturing microstructures. Recently, Beebe et al. reported that the height of PDMS microfluidics channels influenced cell proliferation when cells were cultured in channels for a week [53]. In contrast, no effects from the length and width of channels were observed. In the cell-clinics, we can also build SU8 vials with different heights. We can always design a bilayer to open and close the vials and enable the culturing, no matter what the height of the vial is. The investigation of the effect of the microenvironment on cell behavior is very important for understanding cell biology, and is helpful to biomedical applications [172].

Chapter 6 Polypyrrole/Gold Bilayer Bending Force

6.1 Background and Problem Statement

The bending force exerted by the PPy/Au bilayer microactuators is a basic but important performance metric. Designers need to know the force so that they can determine how many bilayer-actuated micro-valves are required to open a channel under bio-fluidic pressure [48, 173]. Another example is to open a sealed cell-holding vial in cell-clinics. In particular, the maximum force generated by bilayers against a load is indispensable for possible applications, which is indeed the block stress of bilayers. As mentioned in section 5.1, existing models failed to predict the performance of bilayer microactuators. Hence, in this work a system to measure the force directly was developed.

Force measurement was conducted before in our group by placing tiny objects on PPy/Au bilayers [18, 48]. Graduated MS student Lance Oh used glass cover slips 1 mm × 1 mm × 0.1 mm (L × W × T) weighing 0.52 mg. The glass pieces were manually placed on a Kapton flap actuated by the PPy/Au bilayer microactuators. Voltages were applied to actuate the flap until it could not lift the pieces any more (Figure 86). Since the smallest size of glass that could be cut was still much larger than that of the flaps (0.4 mm × 0.4

mm), one end of the glass always rested on the substrate, which resulted in inaccurate measurements.

Based on Oh's preliminary results (Figure 87), we purchased a force transducer (Type 406 A, Aurora Scientific Inc., Aurora, Canada) with 0.01 μN resolution and a loading range of ± 0.5 mN (positive reading represents a pulling force applied to the transducer, negative means a pushing force). The force transducer is composed of a control box and a transducer head (Figure 88). A glass tube (Figure 88b) extruding from the transducer head is connected to a variable displacement capacitor inside the transducer head [174]. When a pulling or pushing force is applied to the glass tube, the capacitance changes. A control circuit processes and converts the capacitance change to an output voltage, which is proportional to the sensed force.

In our setup, the output of the transducer was input to the potentiostat, and thereby the force data correlated with the potential and current. The force transducer was calibrated before the measurement by using objects with known weight.

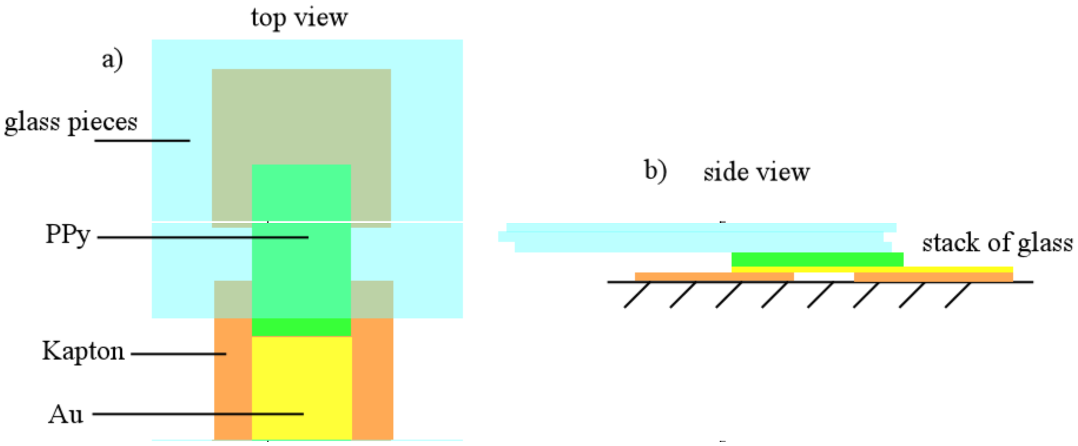

Figure 86. A schematic of measuring bilayer-bending force by placing glass pieces on bilayers and plastic flaps. a) Top view, b) side view. Note the glass was much longer than the flap. (Courtesy of Oh [48].)

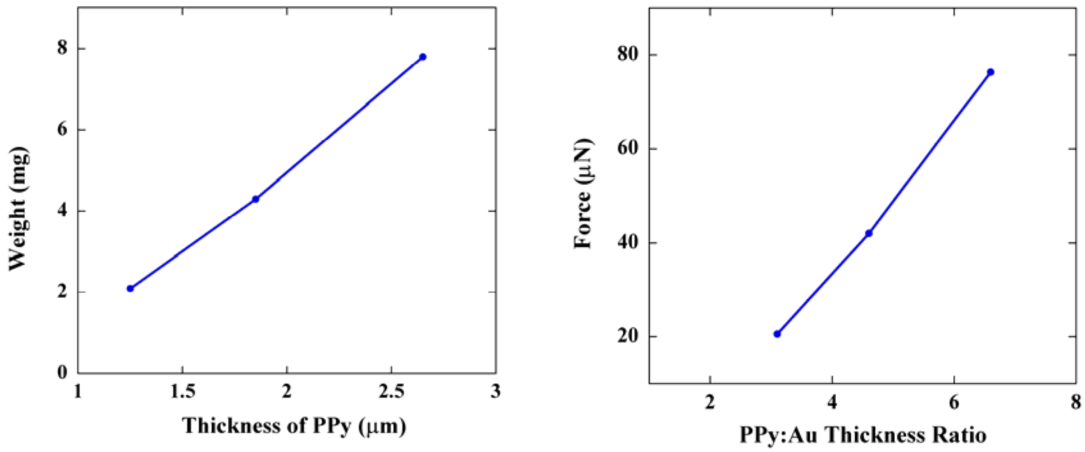

a) Maximum weight lifted by a bilayer vs. thickness of PPy.

b) Force vs. PPy/Au thickness ratio, data converted from a).

Figure 87. Preliminary results of measuring bilayer-bending force by placing glass pieces on bilayers (89 μm long, 300 μm wide, 4000 Å thick Cr/Au) and plastic flaps. (Courtesy of Oh [48].)

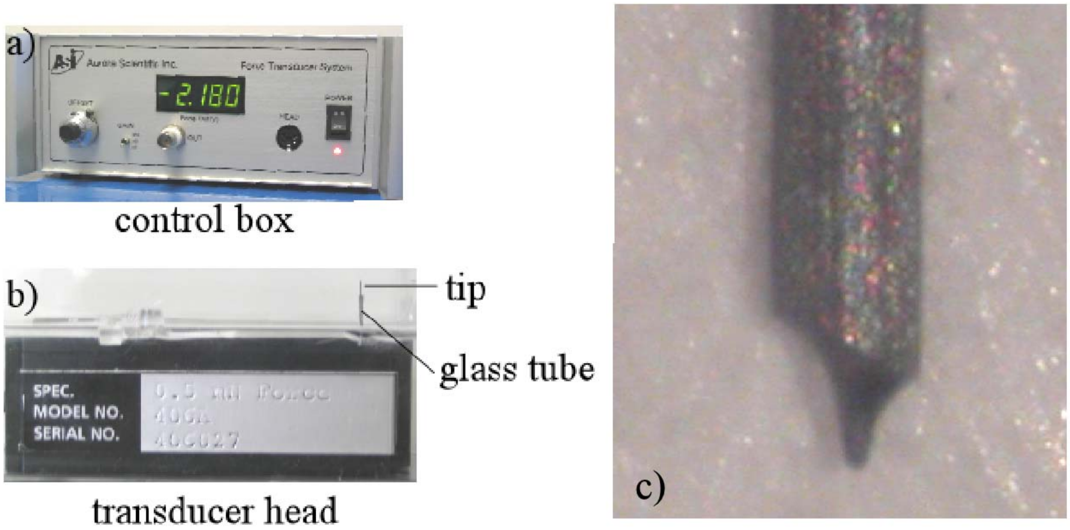

Figure 88. The force transducer (Type 406 A, Aurora Scientific Inc., Canada) is composed of a control box (a) and a transducer head (b). A STEM tip c) is glued to a glass tube for measuring the force.

6.2 Experimental Methods

The force measurement system was developed by me and Dr. Christophersen to measure the tiny force in an aqueous environment. The experimental setup and operation procedure had to be considered carefully for accurate and repeatable measurement. The primary challenges during development included:

1) how to create a clear view of the microscale bilayers so that the force transducer could be positioned,

2) how to obtain a reasonable reading during the measurement, and

3) how to ensure repeatability and accuracy of the measured force.

The samples used to measure the force were the same as those for the bending curvature measurement. Because the force transducer was placed over the sample (Figure 89b), the microscope had to be positioned at an angle with respect to the sample (Figure 89a). The sample was placed in an electrochemical cell, with a piece of graphite used as the counter electrode. The bending of the bilayer was monitored through the angle-view imaging system as shown in section 5.2. The whole setup was placed on an optical table to reduce vibrations. At the same time, all measurements were conducted during the night, when fewer people walked in the hallway, which helped keeping the image still, as well as improving the force measurement repeatability and accuracy.

The SU8 plates were rotated by the bilayers to hit the force transducer for a reading. Because the glass tube was larger than the plate, a sharp tungsten tip (Figure 88c) was glued to the glass tube with paraffin wax as the sensing element. The tip came from Prof. Chia-Hung Yang (Electrical & Computer Engineering, UMCP), who used the tip in a scanning tunneling electron microscope (STEM).

The force transducer was calibrated before use by placing a 5.40 mg piece of Al foil on top of the sensing tip. According to the manual, the corresponding output voltage should be 1.060 V (conversion factor 50 μN/V). In practice, the average voltage from the transducer based on 5 separate measurements was 0.965±0.002 V. As a result, the conversion factor was changed to 55 μN/V.

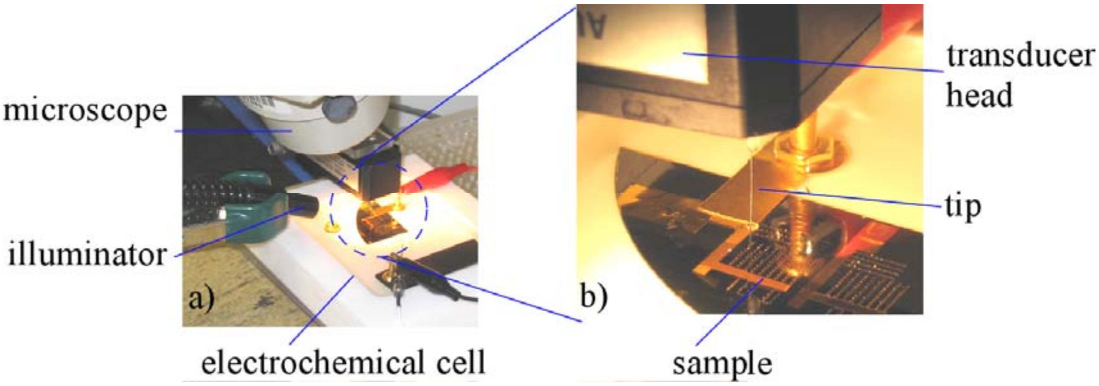

Figure 89. a) The force measurement setup is composed of microscope, a light source, an electrochemical cell, and the force transducer. b) A sharp tungsten tip (Figure 88c) is glued to the glass tube with paraffin wax as the sensing element.

The measuring procedure is illustrated in Figure 90. The sample was placed into the electrochemical cell. Under the microscope, the tip was positioned a little bit above the plate, and then -1 V applied using the potentiostat. As a result, PPy was reduced and the plate was moved upward by the bilayer to hit the transducer, and generated a reading (Figure 91).

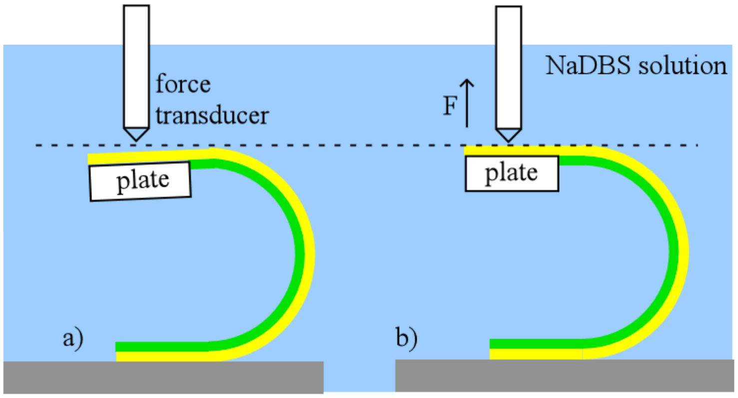

At 0 V, PPy is oxidized; the transducer is positioned that it does not touch the plate.

At -1 V, PPy is reduced; the transducer touches the plate and generates a reading.

Figure 90. Schematic of the force measurement procedure. a) The tip is positioned, not touching the plate. b) A reduction voltage is applied and kept that PPy expands to actuate the plate to hit the force transducer for a reading.

Bilayers with different PPy:Au thickness ratios and structural-Au thicknesses had different bending curvatures. In other words, the length of the bilayers that generated a bending angle of 180° varied with respect to these two factors. In the force measurement, the bilayers were required to have 180° bending angle (Figure 92a, b). Otherwise, the bilayer will exert a horizontal force, F_h, on the transducer (Figure 92c). According to the user's manual of the transducer [174], this horizontal force will generate large errors in the measurement. Hence, this error should be avoided by choosing a longer bilayer to measure. At the same time, the longer bilayer is wider (5.3), which therefore generates larger force and makes the measurement easier. Based on the results of the curvature measurement, bilayers with 100 μm length and 400 μm width were measured.

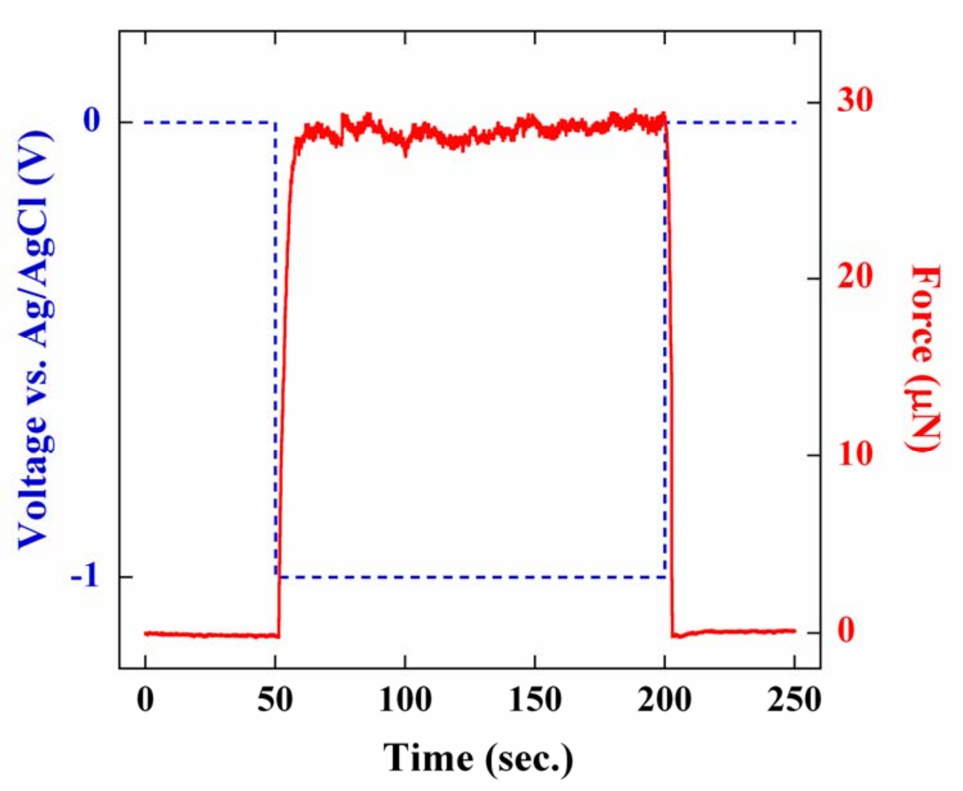

Figure 91. The corresponding current (dashed line) and force (solid line) when -1 V was applied to a bilayer (PPy:Au thickness ratio 19, 1000 Å thick structural-Au).

In practice, force was measured by applying a stepwise voltage, 0 V → -1 V → 0 V. The force was calculated by subtracting the average readings at 0 V (0-50 and 200-250 sec with plates not touching the transducer tip) and -1 V (50-200 sec, plates touching the tip) in Figure 91. The time delay in Figure 91 between the voltage and the force was the time that ions entered or left PPy, PPy changed volume, and the plate traveled.

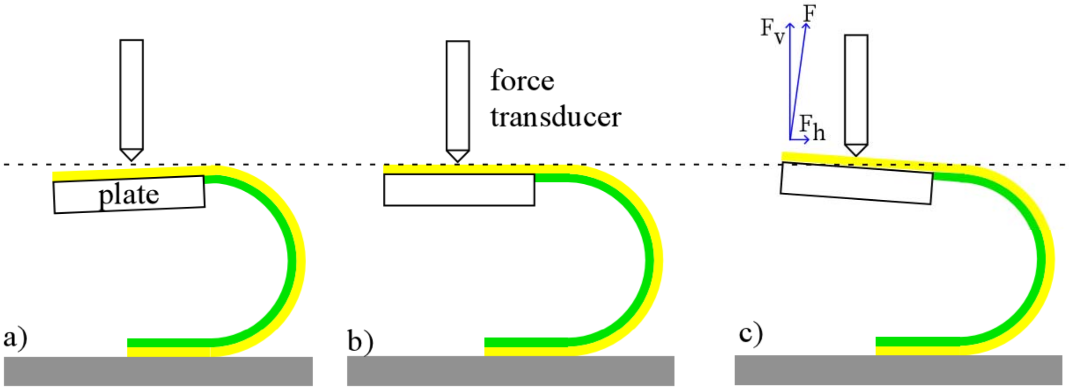

Figure 92. Schematic of the bilayer with bending angle a) more than, b) equal to, and c) less than 180°. In c), the bilayer exerts a horizontal force F_h on the transducer and generates errors in the measurement, which should be avoided by choosing a bilayer with a suitable length.

Note that the tip was positioned a little bit above the plate (Figure 93), because the tip would sense environmental vibrations when it was positioned on the plate directly, which brought a lot of noise to the zero reading before applying the voltage.

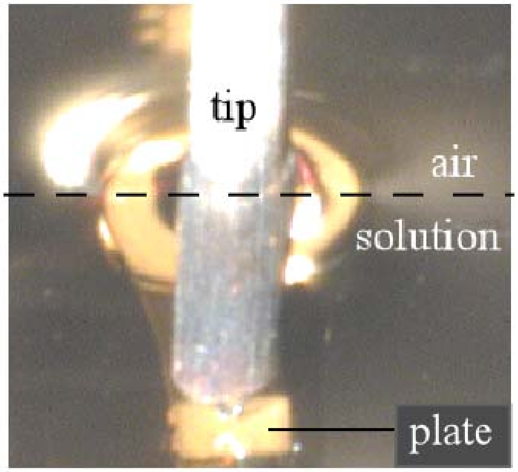

Figure 93. The tip was positioned at the plate center and a little bit above the plate to reduce vibration reading before applying voltage.

In order to reduce the measurement error, the force was measured at least on 9 bilayers, and the results averaged. Multiple measurements by applying a pulse voltage cycle were not employed because the force dropped under the second and third load (Figure 94).

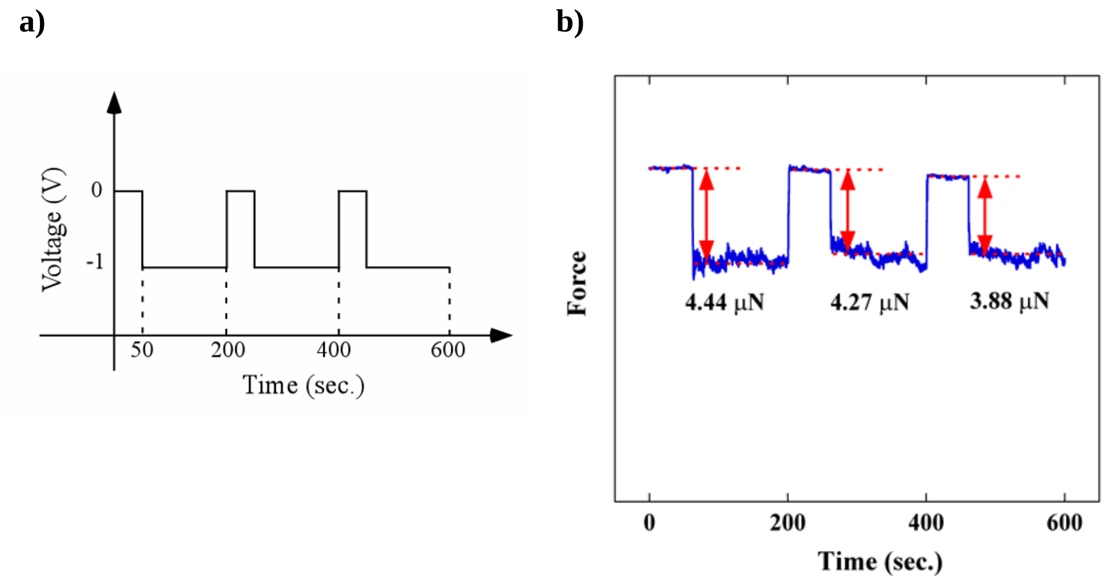

Figure 94. Experimental curve (b) from applying a pulse voltage cycle (a) to a sample with 9:1 thickness ratio and 1000 Å thick structural-Au. Force drops under the second and third load.

The force transducer tip was not positioned at the edge of the plate because 1) the arm of force increases and the force decreases by half, which makes the measurement more difficult (smaller signal/noise ratio) and 2) plates were observed sliding away from the tip so that no reading was recorded. In addition, when positioning the tip at the center of the plate, the edges of the plate can be used as references to help for an identical position every time (Figure 93).

An issue of the force measurement is the smallest force the transducer can measure. In both cases of plates touching and not touching the tip, the standard deviation of the output force was 0.05 μN. If a force is less than 0.1 μN, it will not be identified from the reading (Figure 95). Hence, the smallest force that can be measured is 0.1 μN.

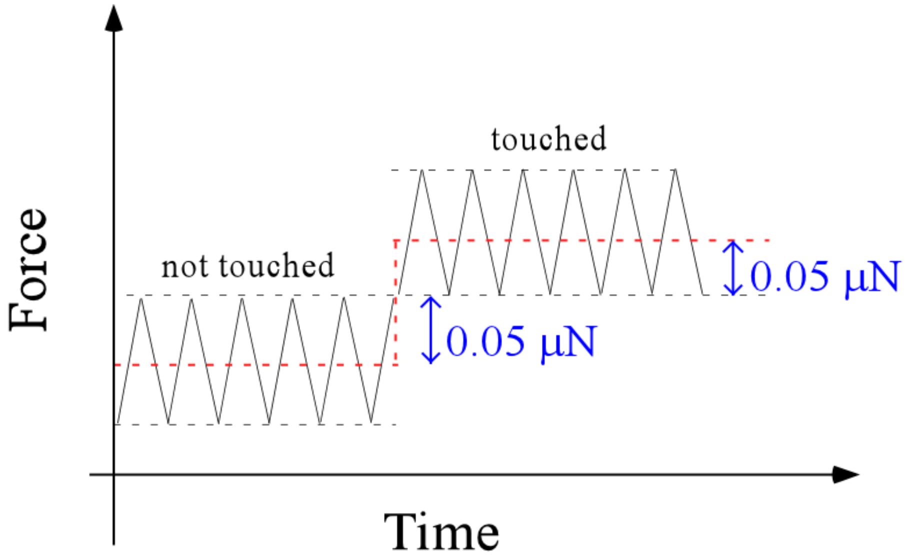

Figure 95. Schematic of smallest measurable force determined by reading variations.

6.3 Results and Discussion

Figure 96 shows how the force changes with the PPy:Au thickness ratio. As expected, the force increases when the thickness ratio becomes larger. At the same time, the force increases when the structural-Au becomes thicker, which is compatible with Timoshenko’s model [164].

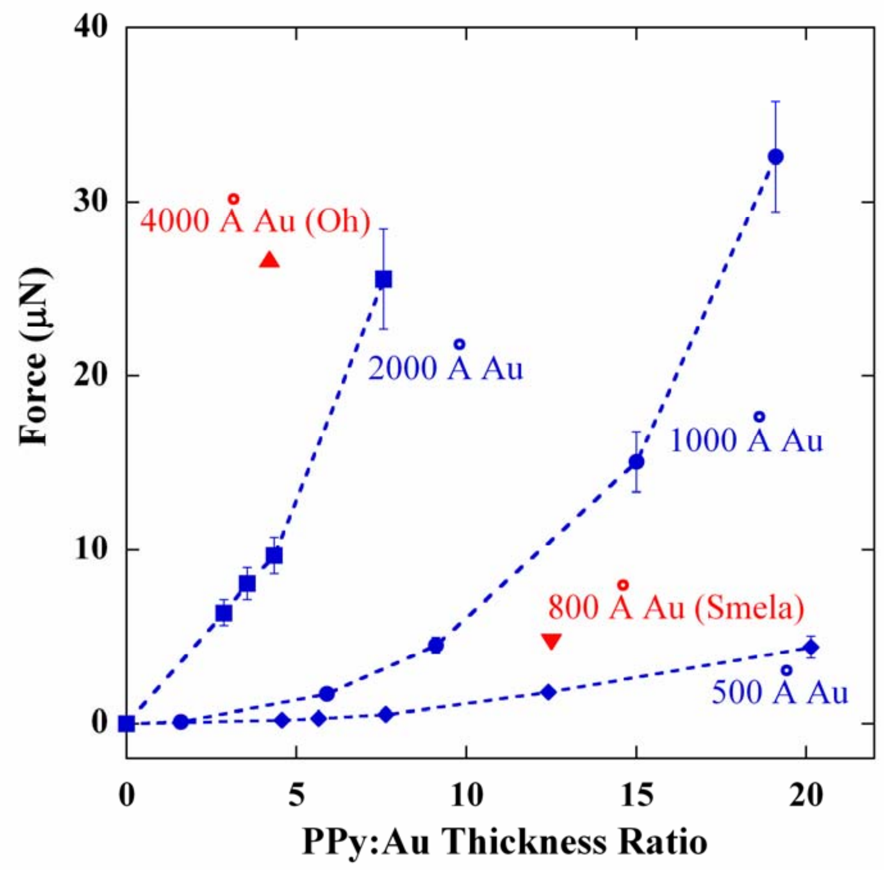

Figure 96. Force data generated by bilayers with various PPy:Au thickness ratios and structural-Au thicknesses. As expected, the force increases with thickness ratio and structural-Au thickness. The data from our group's previous work are also plotted, which follow the trend of my data fairly well.

Our group's preliminary results are also plotted in Figure 96 to allow comparison with our new results. Oh's bilayer was 89 μm long and 300 μm wide, which was close to mine (100 μm long and 400 μm wide). In his experiments, because the glass pieces were long, he assumed that half of the weight of the glass pieces were on the bilayer, and the other half were on the supporting ground [48]. Hence, the force exerted by the bilayer (PPy:Au thickness ratio of 4.2 and 4000 Å thick Au) was 20 μN (Figure 87b). If the bilayer had been 400 μm wide, this force would have been 26.7 μN. Smela reported that approximately 70 bilayers (1.91 mm × 40 μm, 800 Å thick Au, 1 μm PPy, 12.5 thickness ratio) lifted a total weight of 3.3 mg [18]. The force exerted by one bilayer (although it was not the maximum force) was normalized to 4.7 μN. Oh and Smela's forces followed the trend of the force vs. structural-Au thickness curves, which verified that these measurements were realistic and reasonable.

Dr. Christophersen and I redesigned the bilayers so that the plates were ten times longer and the bilayers ten times wider in order to obtain higher signal to noise ratios as well as results that would be more straightforward to model. However, during testing, the bilayers were found to bow, which resulted in unreasonable force readings. Future work will include improving the design to accommodate the development of a bending force model.

6.4 Size of Forces Obtained

As mentioned in the *Introduction*, in order to open a sealed vial in the cell-clinics, the force exerted by the bilayer has to be larger than the force sealing the vial, which is furthermore larger than the force a cell generates to push the lid. Now the force that the bilayers can exert has been measured. How much force can a cell generate? Lin et al. employed miniature transducer to measure the contractile force generated by a single rat heart cell [175-177]. Briefly, the cell was glued between two polysilicon beams. When the cell contracted, the beams deformed; the deflection was monitored either by a camera or an integrated strain-gage. By improving the structure and fabrication of the transducer, their measurement dropped from 32 μN [177], 13 μN [176], to 6 μN [175]. Tan et al. used another method to measure the contractile force [178]. They fabricated arrays of one-end anchored microneedles. A bovine muscle cell was placed on the needles. When the cell contracted, the needles under the cell deflected. A bending force exerted on each needle was calculated based on the deflection; summing up the bending forces from all the deformed needles resulted in the force cell generated, which also depended on the area the cell spread. The maximum force they measured was about 1 μN. Galbraith and Sheetz [179] measured the force by using a similar microfabricated device: arrays of pads on the free ends of cantilevers. A chicken embryo fibroblast crawled on pads and the force generated by the cell was calculated by monitoring the displacement of the pad. They showed the result of 0.1-4 nN/μm^2. Typical dimension of cells is 5-20 μm in diameter [127]. For example, Pan's [180, 181] group microfabricated "neuron cages" with 30 μm diameter to encage neuron. Based on these data, the force a neuron generates during moving is about 3 μN, which is in the range of the forces the bilayer can exert. Therefore, the bilayers can exert enough force to open a vial that is sealed to contain cells.

6.5 Summary and Suggested Future Work

In this chapter, another metric of PPy/Au bilayer microactuators, the bending force, was measured with respect to the PPy:Au thickness ratio and the thickness of the structural-Au. An experimental system and a methodology were developed to mechanically interface the microactuator with a macroscale instrument for measurement. The measurement results show that the force is on the order of μN. It increases with the thickness of PPy; at a fixed PPy:Au thickness ratio, thicker bilayers generated more force.

Based on the results of curvature and force measurements, cell-clinics for sealing the cell-holding spaces can be designed. An example is introduced here. Bovine aortic smooth muscle cells (Figure 29 in section 3.3) were employed to test the biocompatibility of cell-clinics. These cells are approximately 15 μm in diameter. In order to hold this kind of cell, the height of the vial should be larger than 15 μm. In the fabrication of cell-clinics, the lids and vials are formed simultaneously by patterning SU8. In other words, they have the same height. As a result, the bending diameter d of the bilayers should be larger than twice of the diameter of the cell, i.e. $d > 30$ μm or $\kappa < 0.06$ μm^{-1}. The force this kind of cell can exert has not reported before. According to the analysis in section 6.4, it is reasonable to assume the force is smaller than 10 μN. So the force exerted by the bilayer should be larger than 10 μN. A bilayer satisfying these requirements is found by checking Figure 83 and Figure 96: a PPy:Au thickness ratio of 8 with 2000 Å thick Au. The bending curvature is 0.025 μm^{-1} ($d = 80$ μm) and the force is 25.5 μN (400 μm wide bilayer). If this force is applied to a lid (150 μm long and 420 μm wide, Table 3 in section 5.3), a pressure of 405 Pa will be generated.

Chapter 7 Summary and Contributions

In this dissertation, three key metrics of PPy/Au bilayer microactuators, lifetime, bending angle, and force, were measured for the first time. These experimental results will enable the design and fabrication of cell-clinics, a CMOS-based microsystem for cell study and cell-based sensing. Furthermore, these results will help to understand the basic properties of bilayer-based devices, e.g. how they perform and what are the factors affecting their performances. Based on the knowledge and data, more real devices and microsystems will be developed and commercialization will be promoted.

Lifetime of bilayer microactuators is limited by PPy delamination from electrodes and PPy degradation with electrochemical cycling. The delamination problem has troubled the community for the last decade. In order to solve this problem, Au electrode surface were roughened by electroplating another layer of Au, as well as by wet etching the original Au surface. Through tape and cycling tests on samples processed by various conditions such as plate voltages, plate solution concentrations, plated Au thickness, and etched Au depths, the surface morphologies for a strong adhesion between PPy and Au were identified. Thick plated Au (>1 μm) generated protrusions on the surface; shallowly etched Au (< 1000 Å) showed a "layer" structure. PPy was anchored on both surfaces, so that the adhesion was improved. Based on the surfaces without delamination, the loss of electroactivity of PPy with electrochemical cycling was investigated. The total exchanged charges of PPy linearly decreased with cycling, losing 40% in the first 20,000 cycles and another 20% in the next 40,000 cycles. These results elucidate the meaning of the lifetime of PPy-based devices in aqueous electrolytes, and therefore help designers to determine their feasibility for a specific biomedical application. Part of this work and preliminary results have been presented in the SPIE's 12th Annual International Symposium on Smart Structures and Materials (EAPAD 2005) [182].

Curvature was measured from micro-scale PPy/Au bilayers with a series of dimensions and configurations by taking overhead photos and calculating projections. Bilayers with a fixed PPy:Au thickness ratio showed a specific curvature. As the PPy:Au thickness ratio increased, the curvature first increased and reached a peak around 5:1 PPy:Au thickness ratio, and then decreased. The thicker structural-Au in the bilayer resisted bending, which generated smaller curvature. These experimental data can be used directly to enable design and fabrication of real devices. In addition, a simple model based on classical beam theory was introduced to describe the bending behavior of bilayers. Existence of a strain gradient along the thickness of PPy was confirmed by fitting the experimental data, which explained the failure of prior work on modeling bilayer bending due to neglecting this PPy strain gradient. On the other hand, the fitting showed that there were no significant modulus gradients in the film. Part of this work and preliminary results have been presented in the SPIE's 12th Annual International

Symposium on Smart Structures and Materials (EAPAD 2005) [173].

A measurement setup and methodology were developed to measure the tiny force generated by PPy/Au bilayer microactuators. The bending force was measured with respect to the PPy:Au thickness ratio and the thickness of the structural-Au. The measurement results showed that the force was on the order of μN. It increased with the thickness of PPy; at a fixed PPy:Au thickness ratio, bilayers with thicker structural-Au generated more force. In real applications, an external loading always exists to restrain bilayer bending. Hence, these first hand data are indispensable to designers. The work of developing the tiny force measurement system and some preliminary results have been presented in the SPIE's 12th Annual International Symposium on Smart Structures and Materials (EAPAD 2005) [173].

In addition, work was performed on fabricating cell-clinics. A method was developed to build PPy/Au bilayer microactuators on CMOS chips. This method provides an easy way to deal with post-CMOS MEMS fabrication, which will benefit the lap-on-a-chip field. Furthermore, this work provided experiences with different combinations of fabrication steps and sequences, which will help future designers to modify the processes when more components are added into the microsystem for more functions. Part of this work and preliminary results have been presented in the IEEE's 26th Annual International Conference on Engineering in Medicine and Biology Society (EMBS 2004) [46].

Bilayers on a plastic substrate were also designed and fabricated so that the substrate itself folded, up to 360°. Part of this work and preliminary results were presented in the 12th International Conference of Solid State Sensor, Actuators, and Microsystems (Transducers 2003) [165].

Appendix A Deposition of PPy

The experimental setup to deposit PPy(DBS) was a electrochemical cell with three electrodes connecting to a potentiostat (Autolab PGSTAT30, Eco Chemie B.V., the Netherlands), Figure 3. All the three electrodes were immersed in an aqueous solution of 0.1 moles/liter (M) pyrrole in 0.1 M NaDBS (see [10] for details about making the solution). An Au-coated silicon substrate was connected to the working electrode (WE) lead; PPy was deposited on the Au. The reference electrode (RE) was Ag/AgCl (type MF-2052 RE-5B, Bioanalytical Systems Inc., West Lafayette, IN). A reversible redox reaction (equation (12)) takes place and reaches equilibrium at the RE. Thus, no current flows through the RE. This reaction provides a reference potential (0 V) [12]. All electrochemical potentials given in this dissertation are voltages applied between the WE and the RE (i.e. vs. Ag/AgCl). The CE was either a piece of platinum foil, an Au-covered silicon substrate, or a piece of graphite. In Figure 3, an Au-coated silicon substrate was used as the CE. The CE should be much larger than the WE to ensure that the reactions do not limit the speed of the reactions at the WE [10]. The WE, the aqueous NaDBS solution, the counter electrode (CE), and the potentiostat comprise a complete current loop.

$$\textbf{(12)} \quad \mathbf{AgCl(s) + e \leftrightarrow Ag(s) + Cl^{-}\ (aq)}$$

In practice, PPy can be deposited by applying a constant voltage or current. Because PPy can be overoxidized by applying a constant current [10], our group prefers applying a constant voltage. The suitable voltage value is related to the electrochemical oxidation procedure. If the voltage is too low, the deposition rate is slow, or no deposition takes place. At a higher voltage, the deposition becomes faster. However, the deposited PPy film is not uniform: the edge is thicker than the center [10]. The suitable voltage is also related to the cell configuration (distance between WE, RE, and CE). Hence, every time before depositing PPy on real samples, PPy was first deposited onto a scrap sample (an Au-coated silicon piece) to find the suitable voltage. A voltage ramp was applied from 0 V to 0.8 V at 0.05 V/s and the corresponding current recorded. The current rose between 0.45 and 0.5 V (Figure 97a), indicating the deposition started. In order to obtain a uniform PPy film, a fairly low voltage was used, for example 0.47 V in Figure 97b. Under a suitable low voltage, the PPy film is deposited at a nearly constant rate.

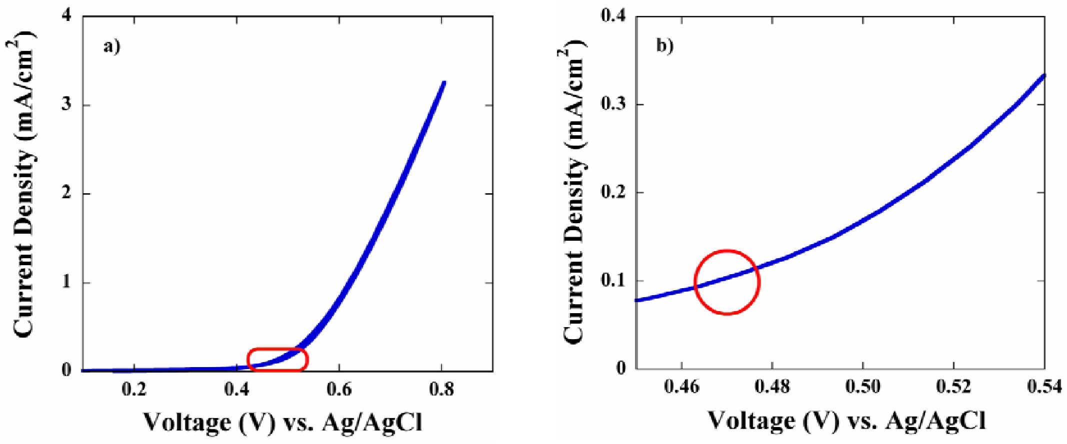

Figure 97. a) A voltage ramp vs. Ag/AgCl between 0 and -1 V at 0.05 V/s was applied and the corresponding current was recorded. The current rose between 0.4 and 0.5 V, as highlighted by an oval. b) A close view of the highlighted area in a). The voltage of 0.47 V was chosen as the optimal deposition voltage, as highlighted by a circle.

In order to obtain a PPy film with the desired thickness, the deposition time and the consumed charge were monitored. There is a linear relation between the charge per unit area and the thickness when the PPy film is thin (< 1 μm) [10]. If the deposition area is known, a specific thickness can be obtained by controlling the total charge applied. In addition, when the PPy layer on Au is thin, there are interference colors that correspond to different thicknesses [10]. An easy way to control PPy deposition thickness is to deposit PPy for a short time (such as 200 seconds), take out the sample, rinse and dry it, compare the color with a thickness-color chart [10], calculate the approximate deposition rate and time for the desired thickness, put the sample back to the solution, and continue the deposition.

Appendix B MicroTAS

MEMS technology is a necessary tool for developing μTAS. In μTAS, liquid transportation on the micro-scale is indispensable, which has to be fulfilled by using microfabricated channels, valves, and pumps [183]. New MEMS materials (such as PDMS [184]) and fabrication techniques (such as soft lithography [185-187]) have also been generated in response to the development of μTAS.

Fast progress in μTAS has been achieved since the early 1990s. Novel methods, such as micro-scale sample preparation (e.g. extraction and preconcentration), chromatography, and electrophoresis have provided new approaches to facilitate analytical chemistry [188, 189]. In addition, μTAS are becoming powerful and multi-purpose tools for biologists and life scientists. DNA and proteins are being investigated by using μTAS [190]. Moreover, there is a growing interest in monitoring cells with μTAS for potential applications in life sciences, pharmaceutical development, and environmental monitoring.

MicroTAS have been developed to facilitate cell sampling, trapping and sorting, treatment, and analysis; see [191] for a good review. Some μTAS products have appeared on the market, such as the flow cytometry chip (Figure 98) by Agilent Inc. (Palo Alto, CA) [192]. Currently, researchers are integrating existing microdevices such as pumps, valves, sensors, and actuators to form more advanced and multiple-purpose systems. Cells, not the composition of cells such as DNA and proteins, will be processed and analyzed.

Figure 98. Cell flow cytometry chip developed by Agilent Technologies, Inc. (Courtesy of Agilent [192].)

Different research groups have shown simple microsystems by forming a cell-culture area on a sensing chip. Brischwei [193, 194] and Baumann [67] randomly plated and cultured a large number of cells (e.g. 10,000 cells) on sensor arrays (area 20 mm^2). The sensor arrays included pH, oxygen, and temperature sensors for in parallel monitoring the cell culture medium, cell morphology, and cell action potential. The signals they obtained were the average of the cell population, however, not from single cells. Eversmann et al. reported culturing one neuron directly on a CMOS biosensor array (Figure 99) [126]. The surface area occupied by the neuron with extended processes was 0.01 mm^2. The culturing area was meso-scale, 30 mm^2. However, the ratio of the cell volume to the extracellular fluid volume in the in-vivo environment is always more than one [52]. Therefore, microstructures must be created in order to mimic an in-vivo environment.

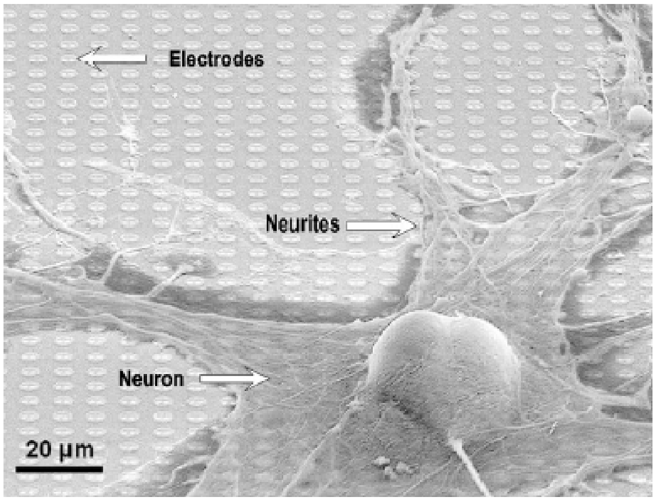

Figure 99. A snail neuron took processes when cultured on sensing electrode arrays. (Courtesy of Eversmann [126].)

Beebe's group constructed a platform comprising microfabricated channels, actuators, and valves to facilitate microsystem development [195, 196]. They are focusing on the effect of physical properties of microstructures on cell behaviors. They found cells cultured in micro-channels had different performance (e.g. proliferation) compared to those cultured in traditional flask [52, 53, 74]. Their research will benefit the design of microenvironment for cell study.

Quake's group has developed an externally actuated, multi-layer PDMS-based microfluidic system [197, 198], which enabled large-scale in-parallel cell processing and analyzing such as cell lysis [199]. Because the materials used to build the microstructures are transparent, it is easy to monitor the system by optical means [198] such as the fluorescence sensing [200]. Nothing has been reported about integrating this system with CMOS sensing.

Sandia National Laboratory is developing microsystems to immobilize cells and deliver molecules (such as DNA and fluorescent molecules) into cells. They demonstrated a micro-teeth (Figure 100a) [201] and a micro-port structure (Figure 100b) [202] for capturing cells. They proposed to integrate electrical, optical, and force sensors to analyze cells [202]. No progress has been reported so far.

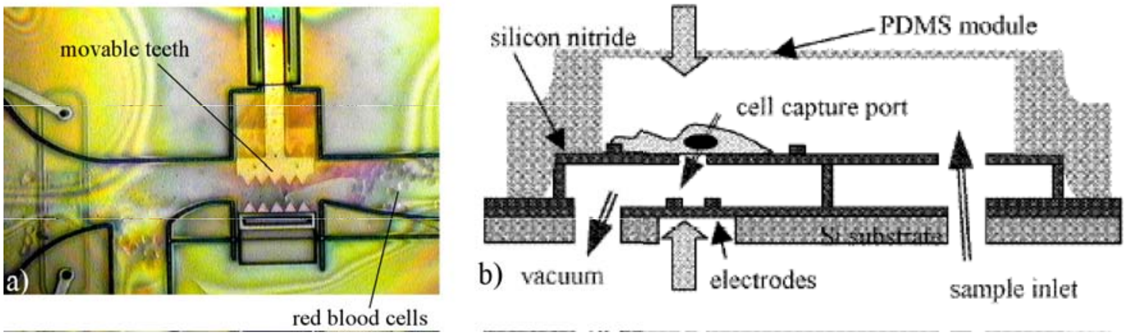

Figure 100. Microsystem for cell study developed by Sandia National Laboratory. a) A micro-teeth for capturing cells. (Courtesy of Okandan [203].) b) Cross-section of a proposed patch clamp array for holding and sensing cells. (Courtesy of Okandan [202].)

In addition to the properties of single cells, communication among cells is also an important topic for study [58]. Pine' group fabricated neuron cages on a silicon substrate (Figure 101) for neural network study [180]. They used a micropipette to place neurons into cages through a hole at the top of each cage [181]. When neurons became mature, their size was larger than the holes, so neurons were encaged. Their next step is to integrate the cages with electrodes for signal sensing [181].

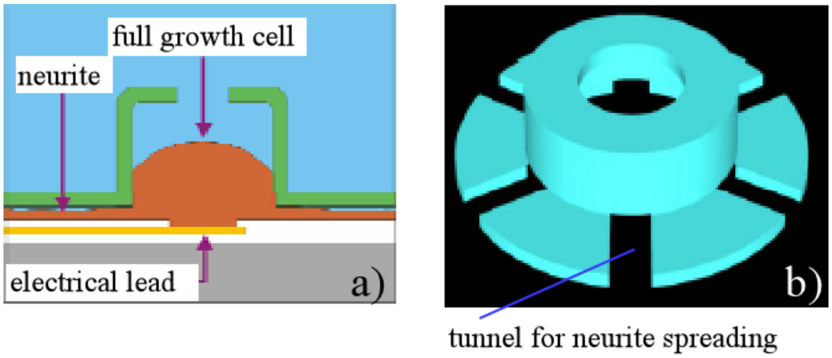

Figure 101. A "neurocage" developed by J. Pine et al. a) Cross-section view of the envisioned neurocage. A neuron is containing in the cage, sitting on the electrical lead for sensing. Neurites spread through the tunnels. b) 3D schematic of the cage. The tunnel was 4 μm wide and 1.5 μm high. (Courtesy of Tooker [181].)

Appendix C   Cell Clinics Fabrication Details

Fabrication of Cell-Clinics, Challenges

The design of the cell-clinics was complex, which made the fabrication difficult. The microsystem was composed of metals (Au and Al), non-metals (e.g. silicon and silicon oxide), and polymers (PPy and SU8). Compatibilities such as the adhesion between materials contacting each other have to be considered. In particular, all the materials must be compatible with cells. Another concern is the CMOS chip: the fabrication is required to be low temperature because high temperature processing damages the CMOS circuitry. Bulk micromachining should be avoided because the sensing electrodes are located on the chip surface. Furthermore, all the fabrication methods (such as baking and etching) and chemicals (such as photoresist, developer, and etchant) should not damage the molecular structure of PPy or affect its physical and chemical properties. (See Table 4 for reference.) In this section, my work of developing and improving the processes to fabricate microstructures on CMOS chips is described.

Table 4. Compatibility between MEMS processing and PPy [10].

Damaging	Use care, test first	Harmless
Cr etchant	acids	Au etchant
high temperature (> 120 °C)		hot plate at 100 °C
developer (KOH), bases	solvents	photoresist
resist stripper / remover		UV light in mask aligner

First-Generation Fabrication Process

The first generation fabrication process is shown in Figure 102. Figure 103 illustrates the differential adhesion method.

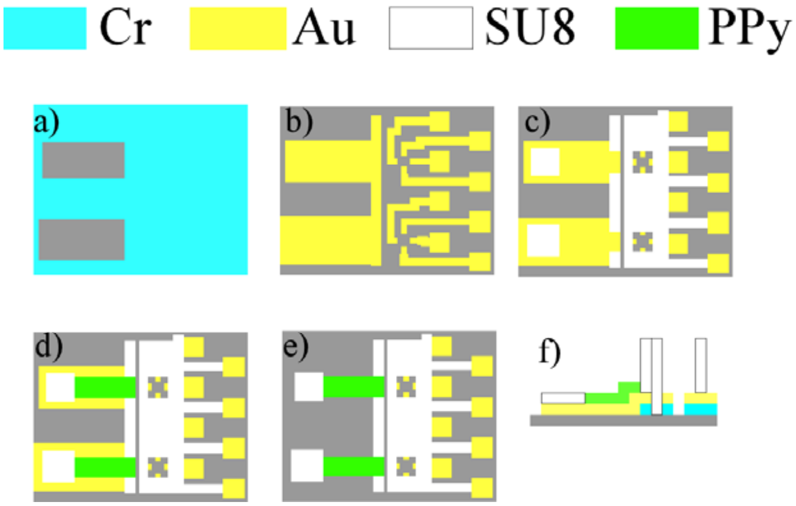

Figure 102. The first-generation fabrication process developed by Smela et al [124]. a) thermal evaporation and wet etching of Cr/Au to permit differential adhesion of Au structural layer, b) thermal evaporation of Au structural layer followed by wet etching to define electrodes, bilayers, and wires, c) deposition and patterning of SU-8 for lids, vials, and insulation of wires, d) electrodeposition of polypyrrole, e) final etching of adhered Au/Cr, f) cross-section of the microstructures. (Courtesy of Lauenstein.)

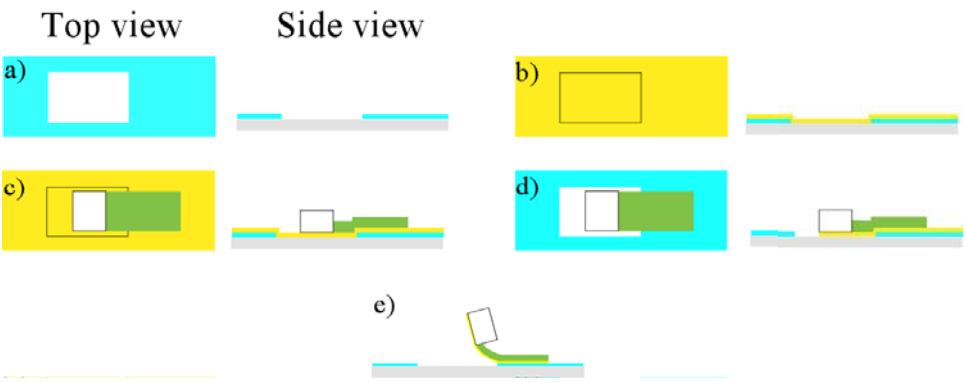

Figure 103. Schematic of the differential adhesion [204]. a) pattern Cr and Au, b) deposit structural Au, c) deposit and pattern other layers, such as PPy (green) and SU8 (white), d) etch away exposed Au, e) actuate structure for self-release. (Courtesy of Lauenstein.)

SU8 is a viscous photoresist; the patterning procedure is composed of several steps, including spinning, soft-baking, exposing, post-baking, developing, and descuming. The datasheet [205] from the manufacturer (Microchem Inc., Newton, MA) and the procedure described in the literature [45, 206] did not work in our clean room. With the help from Mr. Sheng Li of Prof. Ghodssi's group (Electrical and Computer Engineering, UMCP), a recipe was developed to pattern 10 μm thick SU8-5; see Appendix E for details.

The photoresist-pooling process is explained in Figure 104. Replacing SU8 by photoresist to form the anchor areas solved this problem (Figure 105). However, the nonplanarity still existed because the SU8 lids and vials were formed first, then photoresist was used to pattern the PPy. When more vials and lids were placed on a tiny CMOS chip and thicker SU8 structures were used to form deeper vials, this problem became more serious: the nonplanarity interfered with photoresist spreading and resulted in deformed and incomplete photoresist structures after spinning. In order to solve this problem, other methods were tested and the second-generation fabrication process was developed.

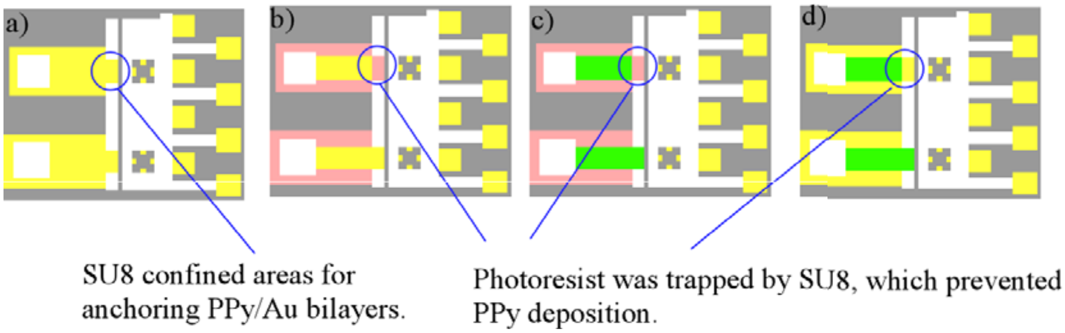

Figure 104. Pooled photoresist was generated by the nonplanarity of the surface. a) SU8 was patterned to form anchor areas on the electrode. b) Photoresist was patterned to form a template for PPy deposition. Note that photoresist was trapped by SU8 at one anchor. c) PPy was deposited on the bilayer and anchor areas. No PPy was deposited at the anchor occupied by photoresist. d) Photoresist was removed by ethanol. The bilayer without the anchor was easy to break.

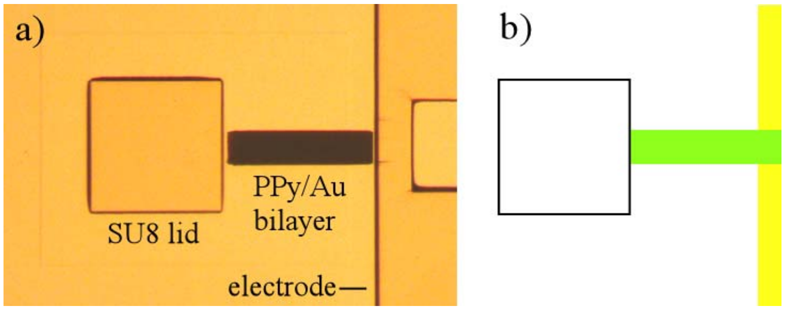

Figure 105. Before depositing PPy, the anchor areas were confined by photoresist instead of SU8. a) No photoresist pooled at the anchor area. b) A schematic of figure a).

Second-Generation Fabrication Process

One way to solve the problem is to use another method to pattern the PPy. Because PPy is primarily composed of carbon and hydrogen, it can be etched in an oxygen plasma [10]. Thus, RIE was used instead of a photoresist template to pattern the polymer. In the new process (called 2-A process, Figure 106), the first three steps (Figure 106a-c) are the same as that of the first-generation process. After patterning SU8, PPy was deposited everywhere on the structural-Au area (Figure 106d). A third layer of Au (named the mask-Au) was thermally evaporated and patterned to cover the PPy that would form the bilayers (Figure 106e). The sample was RIE etched to remove all the exposed PPy (Figure 106f). By employing a power of 200 W and a chamber pressure of 0.3 mtorr, an etch rate of 1.2 μm/minute was obtained. Finally, photoresist was patterned to protect bilayers and electrodes, and both the structural-Au and mask-Au were etched to release the bilayers (Figure 106g).

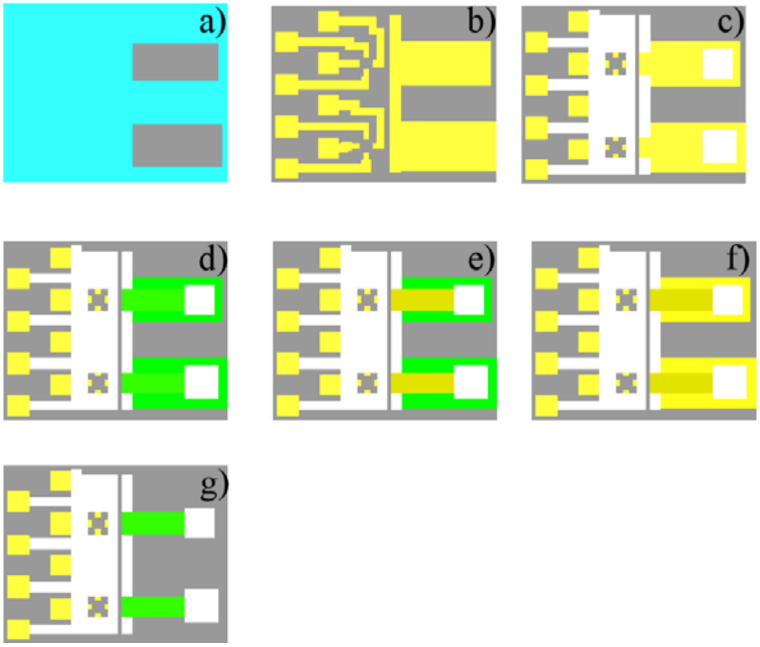

Figure 106. The 2-A process. Steps a) to c) were the same as those in the first-generation process. d) PPy was deposited on the structural-Au. e) The mask-Au was evaporated and patterned to protect PPy on bilayer areas. f) Exposed PPy was removed by oxygen plasma. g) Au was removed to release bilayers.

Successful bilayer bending was observed, which showed that the fabrication, especially the thermal evaporation of Au on PPy and the dry etching, did not damage PPy. However, the final Au etching became the drawback of this process. When the etching time was short, the mask-Au was not completely removed from the surface of the bilayers, which blocked ion transport and generated less bending. When the etching time was long, the Au beneath PPy in the bilayers was undercut, which resulted in the broken bilayers. It was hard to find a suitable etching time. As a result, using oxygen plasma to pattern PPy was feasible, but using another mask material to replace Au would make the fabrication easier.

Photoresist was used as the mask to replace Au during RIE. This process was called 2-B process, Figure 107. Because the photoresist is also a polymer, it has almost the same etch rate as PPy. Therefore, in order to protect PPy, the photoresist had to be thicker. Spinning Shipley® 1813 photoresist at 4000 rpm for 30 seconds generates a 1.5 μm thick layer. The PPy on the bilayers was typically 1 μm thick. By using RIE with 200 W power and 0.3 mtorr chamber pressure, PPy was etched away in one minute (Figure 107f). If thicker PPy was deposited on the bilayers, thicker photoresist had to be used. However, if RIE was longer than 2 minutes, SU8 became opaque (Figure 108) and developed bubbles on the lids (Figure 109). It is not clear what caused the bubbles. However, bubbles were not produced in the first-generation process in which RIE was not employed. Thus, it may be that the vacuum (0.3 mtorr equals to 4×10^{-7} atm) and temperature (around 60 °C) during RIE damaged the MEMS structures, which should thus be avoided in the fabrication.

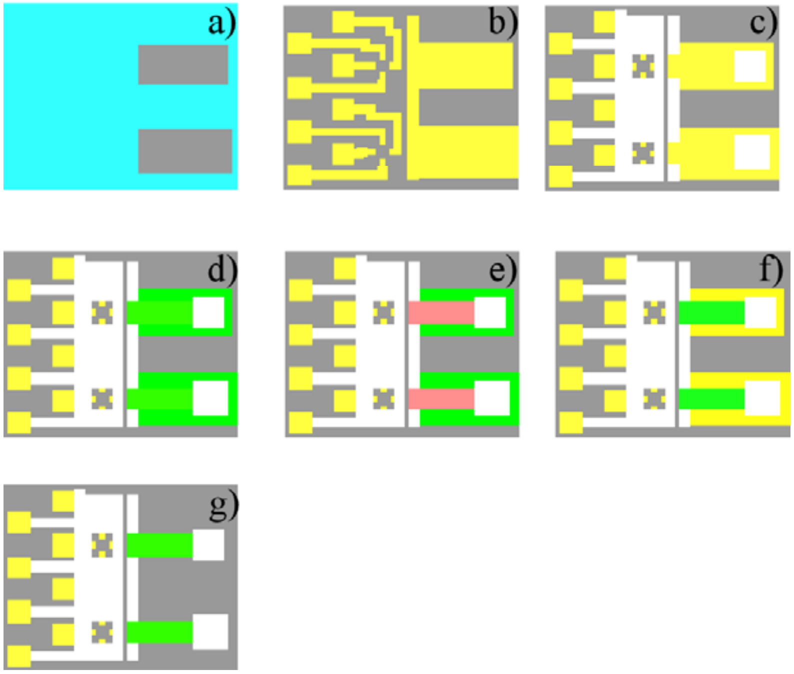

Figure 107. The 2-B fabrication process. Steps a) to d) were the same as those in the 2-A process (Figure 106). e) Photoresist was patterned to protect PPy on bilayer areas. f) Exposed PPy and photoresist was etched by oxygen plasma. After etching, remained photoresist was removed by ethanol. g) Au was removed to release bilayers.

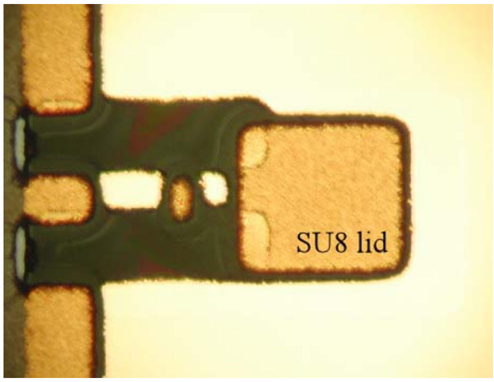

Figure 108. SU8 structures became opaque when staying in oxygen plasma (200 W, 0.3 mtorr) longer than 2 minutes.

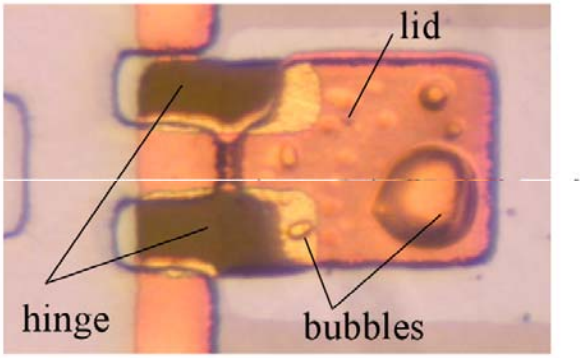

Figure 109. Bubbles were observed on the lids after RIE. The yellow area of the lid was covered by photoresist during RIE, and the orange area was exposed to oxygen plasma.

Third-Generation Fabrication Process

Another way to solve the problem is to pattern PPy first, and then create the SU8 structures (Figure 110). Successful bilayer actuation showed the process of forming SU8 such as developing and baking did not damage PPy.

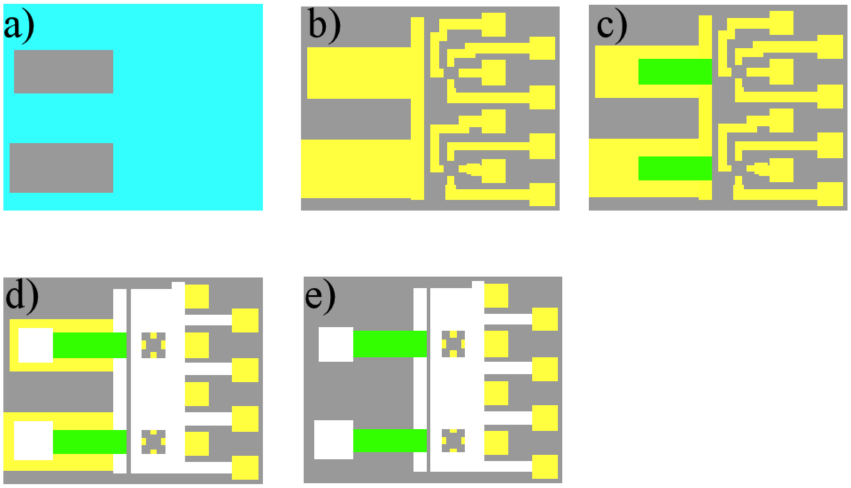

Figure 110. The 3rd generation fabrication process. a) Thermal evaporation and wet etching of Cr/Au to permit differential adhesion of Au structural layer. b) Thermal evaporation of Au structural layer followed by wet etching to define electrodes, bilayers, and wires. c) Patterning photoresist to form a template; PPy was deposited onto the open area of the template. Photoresist was removed by ethanol after PPy deposition. d) Patterning SU8 to form lids, vials, and wire insulation. e) Etching Au to release the bilayers.

Suggested Future Work

The MEMS fabrication process is being updated to accommodate the improved bio-amplifier chip, new sensing mechanisms (e.g. optical sensors), and further system integration. For example, in order to avoid damaging the released PPy/Au bilayers, wire bonding and packaging should be conducted before the final Au etching. However, the bond pads (made of Al, covered by electroless plated Au) were covered by photoresist as protection in the final Au etching; the photoresist had to be removed in order to do wire bonding. A stripper-soaked cotton bar was used to remove photoresist on the bond pads, while keeping photoresist on the other area untouched. The Au came off from some bond pads due to the rubbing, which furthermore led to the failure of the wire bonding. A suggested solution is to cover all the bond pads with photoresist before electroless plating the Au on the sensing electrodes. After plating Au and stripping the photoresist, the pad surface is still Al. (It was tested and verified that photoresist did not dissolve during the plating procedure.) As a result, it is not required to cover the bond pads with photoresist before the final Au etching because Au etchant does not etch Al. After wire bonding, the chip will be packaged that epoxy covers all the bond pads and wires to prevent shorting [47]; cells and the cell culture medium will not contact the Al surface of the bond pads, which avoid Al corrosion and other biocompatibility problems.

Because the cell-clinics is a complex microsystem, a lot of problems related to the fabrication and integration cannot be foreseen until we meet them during the practice. The MEMS process development is indeed a test-and-refine procedure, which not only provides us a suitable method to fabricate the microsystem, but also facilitates us to deeply understand the properties of the composing materials and the compatibility among them. Therefore, all the experiences gaining from the successful and failed samples are very precious and important for further development and improvement.

Appendix D Kapton Bulk-Micromachined Actuators

Introduction

The silicon bulk-micromachined actuators were firstly developed by Smela in 1993 [1]. The fabrication process includes forming the PPy/Au micro-scale bilayers by photolithography, wet etching, and electrochemical deposition, and releasing the bilayers by etching a sacrificial layer or “differential adhesion” [204]; see [10] for details. Based on her approach, self-folding boxes [2] and microrobot arms [43, 44] were demonstrated. The principal mechanism of these devices is that the bilayer bends under applied voltages and actuates a connected rigid plate (Figure 7).

A feature of these devices is that the bilayers locate on top of the silicon substrate. As a result, the movement of the bilayers and the rigid plates is limited to the upper side of the substrate. If the substrate becomes movable, more flexible and complex actuation could be realized, for example, automatic folding 2-dimensional structures into 3-D objects. Furthermore, a roll-to-roll MEMS processes can be enabled, which are potentially inexpensive and mass-produced.

In order to make the substrate to move, the bilayer and the substrate should form a hinge to actuate (Figure 111). In order to fulfill this task, the movable substrate is required:

1) it is rigid enough to be hold by using tweezers; 2) it has stable physical and chemical properties to go through the MEMS processes such as photolithography, etching, and metal deposition; 3) it is flexible enough to be actuated by the bilayers; 4) it can be easily etched through to form the hinges. Silicon and glass satisfy the first three requirements, whereas the through etching of either of them is not an easy task, requiring special equipment (e.g. DRIE for dry etching silicon, double-side aligner for wet etching silicon) or special protection on PPy to avoid damage from etchants (e.g. HF is used to etch glass). As a result, plastic was chosen as the substrate. Kapton® (HN200, 50 μm thick, Dupont Co., Circleville, OH) with the stable properties over a large temperature range [207] was used, which can be etched by using oxygen plasma.

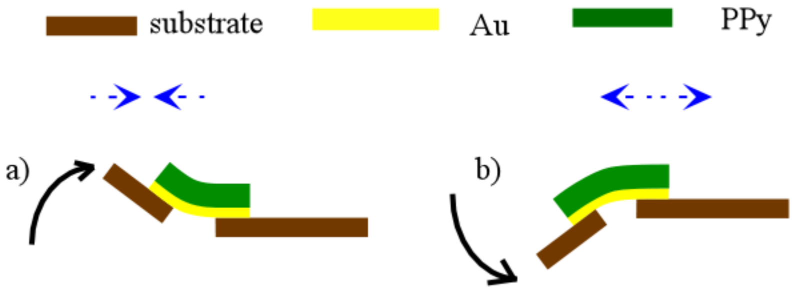

Figure 111. Schematic of a PPy/Au bilayer hinge with a movable substrate. a) When PPy contracts, the bilayer bends clockwise. b) When PPy expands, the bilayer bends counterclockwise. As a result, the bilayer can be controlled to conduct flexible and complex actuations. (Courtesy of Smela.)

The process of fabricating the bilayer-on-plastic is similar to that of fabricating bilayer-on-silicon [10], except etching through the substrate. Because of employing the new material (plastic) and new step (dry etching), however, careful attention has to be paid to the process, particularly to the interfaces between materials contacting each other.

First-Generation Process

The fabrication process is illustrated in Figure 112, primarily including the steps of creating PPy/Au bilayers on the substrate, etching through the substrate, and removing the etching protection to release the structures. Before using as the substrates, Kapton® sheets (HN200, 50 μm thick, Dupont Co., Circleville, OH) approximately 5×5 cm^2 were carefully cleaned with acetone, methanol, isopropanol, and deionized (DI) water; surface contamination prevented the deposited metals from adhering. A layer of gold (Au) was either e-beam or thermally evaporated (200 nm, 0.5 nm/sec, $<5\times10^{-6}$ Torr) onto one side, referred to as the front side. The Au acts as the electrode, as well as the structural layer of the bilayer. It is necessary that the electrodes be electrochemically inert; either Au or Pt can be used. The Au was patterned by photolithography and wet etching (Au etchant, Transene), Figure 112a. Then, polypyrrole (PPy) was electrochemically deposited onto the Au until the desired thickness was reached, Figure 112b.

Next, aluminum (Al) was deposited on the backside as an etching mask (Figure 112c). Just prior to that, the sample was rinsed in methanol and DI water to ensure the Al adhesion. The Al was either e-beam or thermally evaporated (200 nm, 0.5 nm/min, $<5\times10^{-6}$ Torr). This film was patterned photolithographically and wet etched (Al etchant, Transene). As a result, Kapton at some specific areas was exposed for forming the PPy/Au bilayer hinges (Figure 112d). Another 200 nm Al film was deposited on the front side to protect the PPy layer during the subsequent etching of Kapton (Figure 112e).

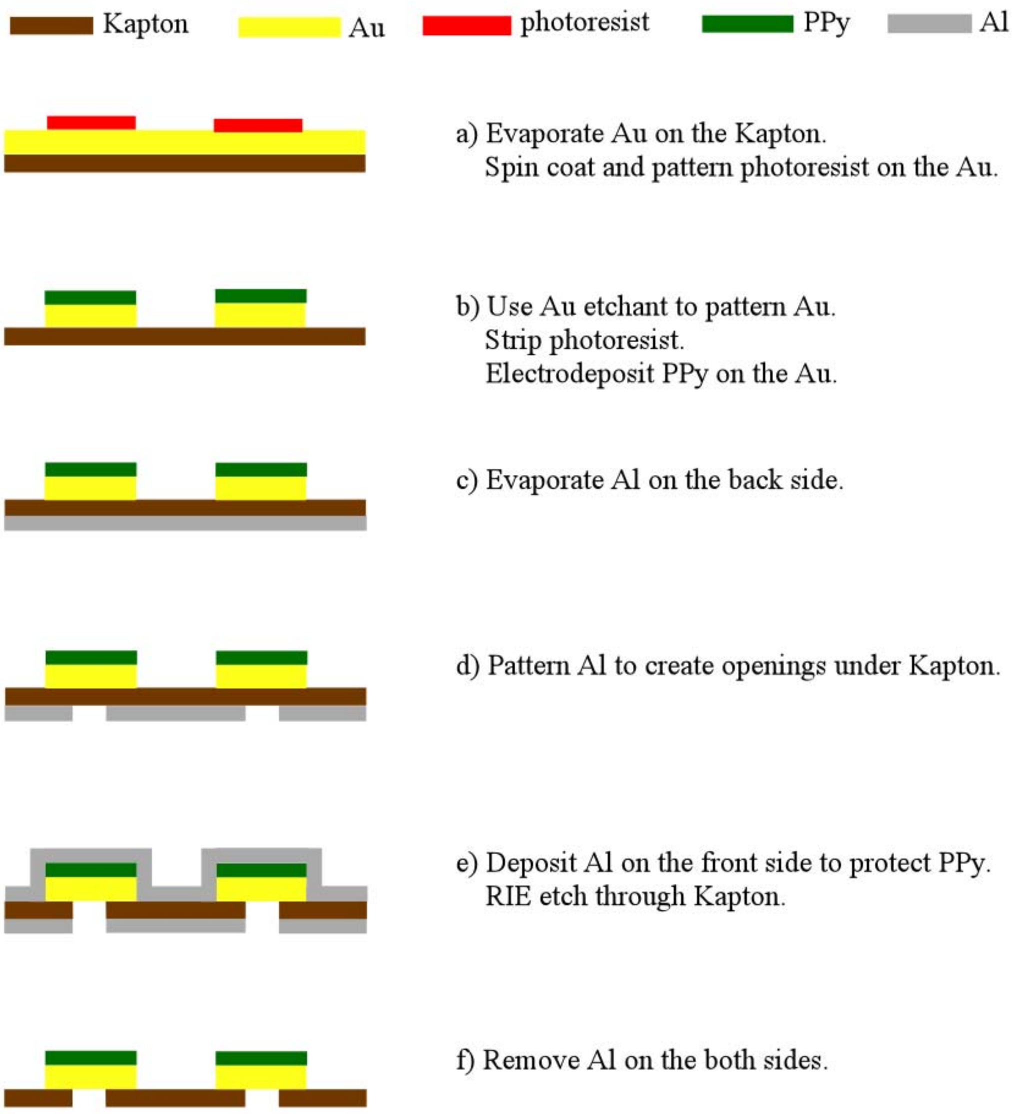

Figure 112. Schematic of the first-generation process to fabricate the bilayer-on-plastic. It is composed of creating PPy/Au bilayers (a-b), etching through the substrate to form bilayer hinges (c-e), and removing the etching protection to release structures (f).

The backside of the Kapton was etched by reactive ion etching **(**RIE) with an oxygen plasma (Jupiter III, March Instruments Inc., Concord, CA) to form the bilayer hinges

(Figure 112e). The chamber pressure and power during RIE were obviously important parameters. At higher chamber pressure, the etch rate for Kapton slowed (Figure 113) and the Al was damaged; 0.3 mTorr gave good results. At 290 W and 0.3 mTorr, the Kapton etch rate was approximately 0.9 μm/min. The last step was to remove the Al from the both sides by using the Al etchant, completing the devices (Figure 112f).

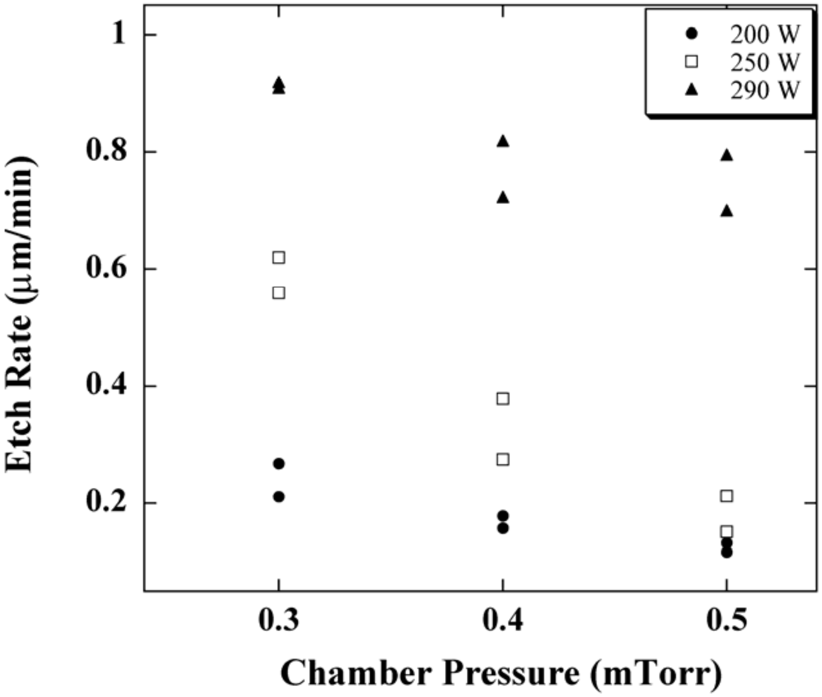

Figure 113. A chart of the chamber pressure vs. the etch rate of the oxygen plasma on the Kapton. The data show under a fixed power, the higher the chamber pressure is, the lower the etch rate is; the etch rate increases when the higher power is applied. All the data is based on the experiments conduced on the RIE at the ECE clean room of UMCP.

Based on this fabrication process, my groupmate L. Oh and I made several devices to demonstrate the bilayer-on-plastic. For example, I made a self-folding box (Figure 114). There were five PPy/Au bilayer hinges (1 mm long and 50 μm wide, Figure 114a) on this device. The PPy on the five bilayers was electrically connected by the Au on the backside of the Kapton (Figure 114b), so the hinges moved simultaneously under an applied voltage. When PPy was oxidized, its volume expanded. As a result, the bilayer hinges actuated 1×1 mm^2 Kapton "sidewalls" to compose a box (Figure 114c-f). When PPy was reduced, the bilayers bent backward to form another box (photographs not shown).

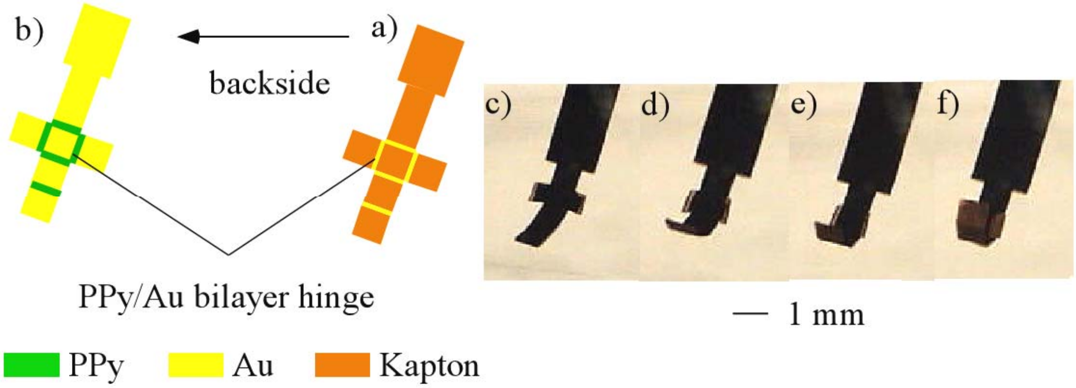

Figure 114. Demonstration of a bilayer-on-plastic based self-folding box. a-b) Schematic of the box's structure, including five bilayer hinges, 1 mm × 50 μm. c-f) Photographs show sidewalls were actuated by hinges to compose a box.

During testing the devices, we met a delamination problem: either the Au layer came off from the Kapton substrate, or PPy came off from the Au. The latter is discussed in Chapter 4 . The former was solved by another groupmate A. Daiub through adding an adhesion promoter layer of chrome (Cr); see [48] for details. As a result, the process was updated by evaporating Cr (10 nm, 0.3 nm/sec, $<5\times10^{-6}$ Torr) onto the substrate, and then evaporating Au without breaking the vacuum. During patterning metals into electrodes, Cr was also etched (chrome etchant, Transene). After the Cr etching, we found the etching residue remained on the sample surface, which resulted in PPy growing on the entire surface instead of on the electrodes (Figure 115). Therefore, before depositing PPy, the residue was removed in freshly mixed piranha solution (1 part sulfuric acid, 1 part hydrogen peroxide, and 5 parts water).

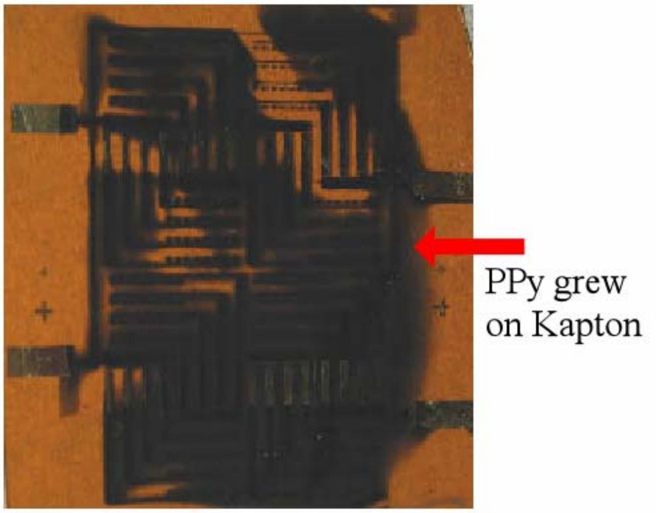

Figure 115. PPy grew on Kapton due to the Cr etching residue. This problem was solved by cleaning the sample surface in the piranha solution. (Courtesy of Oh.)

Based on the improved fabrication process, other groupmates are developing a micro-valve to be used to treat urinary incontinence without surgery (Figure 116); see [48] for details.

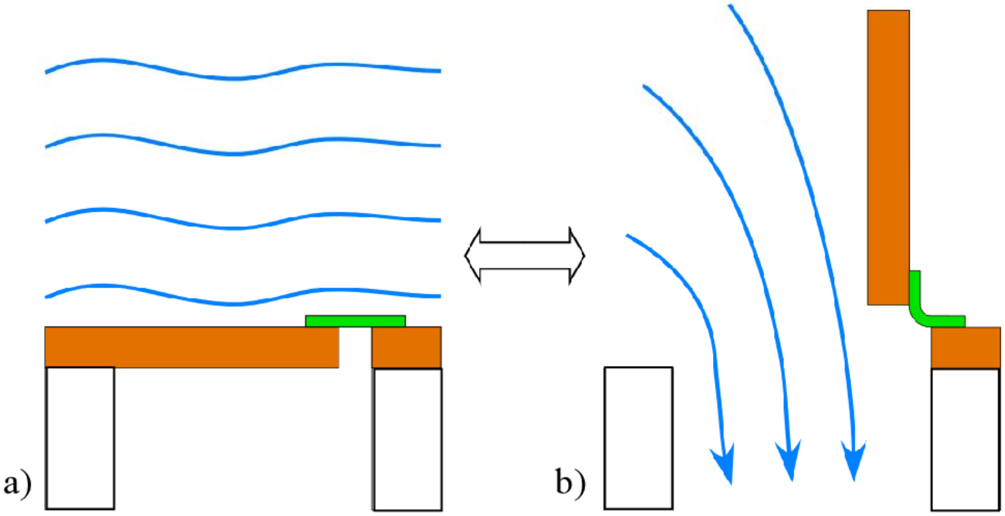

Figure 116. Schematic of the bilayer-on-plastic based micro-valve for urinary incontinence. The valve can be electrically controlled to a) close and b) open the bladder. (Courtesy of Oh.)

Second-Generation Process

In the first-generation process, the Al was evaporated on both Kapton and PPy (Figure 112e) to protect them during the oxygen plasma etching. There were no adhesion problema between PPy and Al. The next plan was to fabricate more complicated devices by placing PPy/Au bilayer hinges on both sides of the Kapton (Figure 117), for which a similar process was proposed (Figure 118). Compared to the first-generation process, the main difference was that Al was thermally evaporated on both sides of the sample to cover PPy (Figure 118c), and then patterned in the Al etchant, Figure 118d. When the sample was immersed into the Al etchant, however, the Al came off from the PPy (Figure 119). Al delamination was investigated, and a method to solve this problem was found.

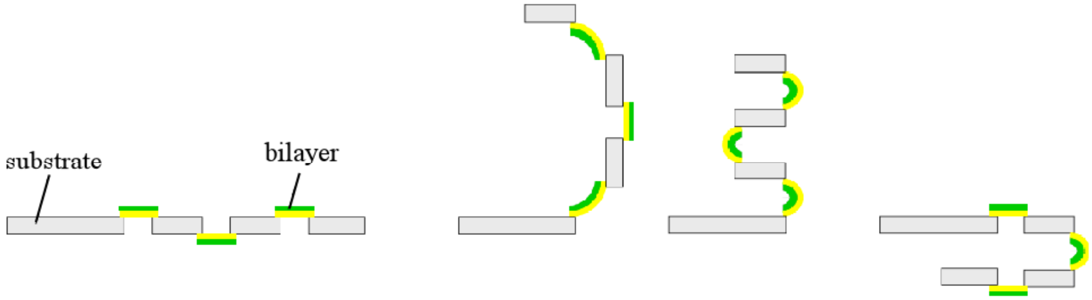

Figure 117. **Schematic of a microdevice that can realize more complicated folding by placing the PPy/Au bilayer hinges on the both sides of the substrate. (Courtesy of Smela.)**

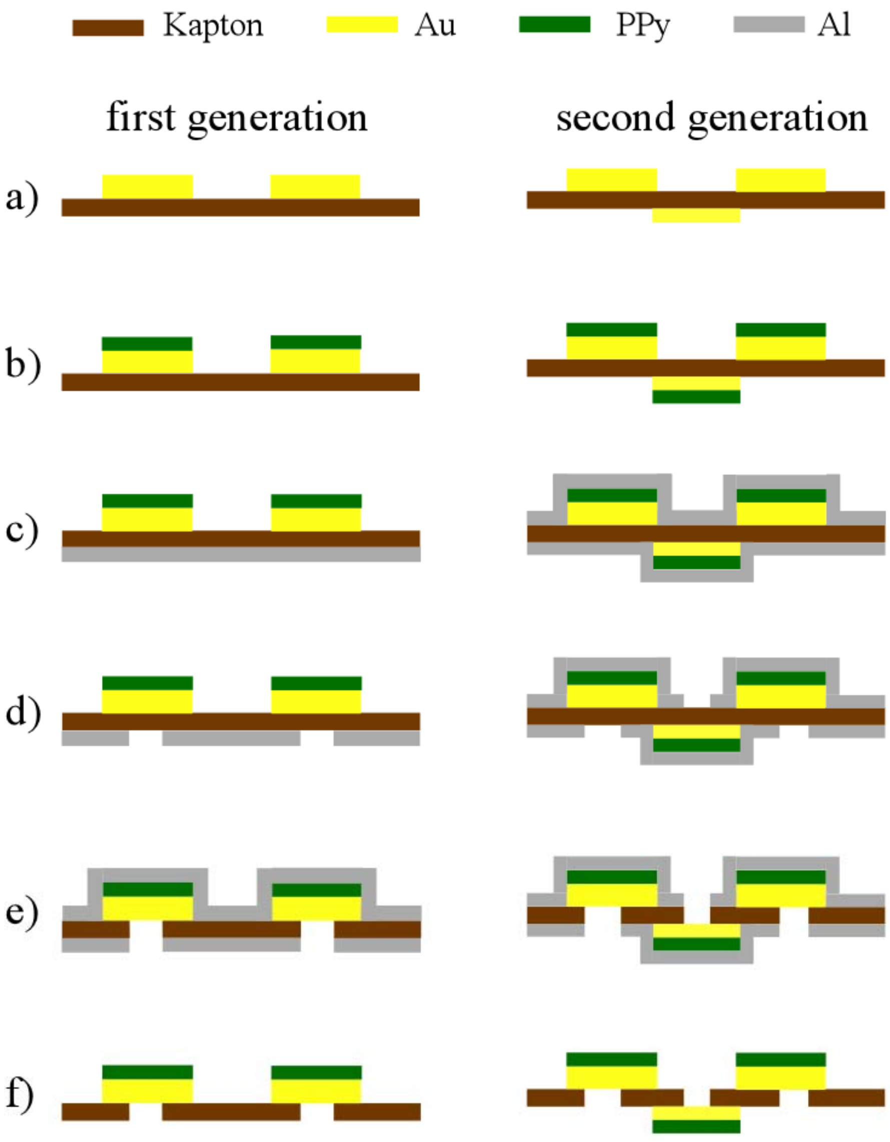

Figure 118. A comparison between the first- and the second-generation process. The primary difference is that the Al is evaporated and patterned on both sides of the substrate in the second-generation, whereas only the Al on the backside is patterned in the first-generation.

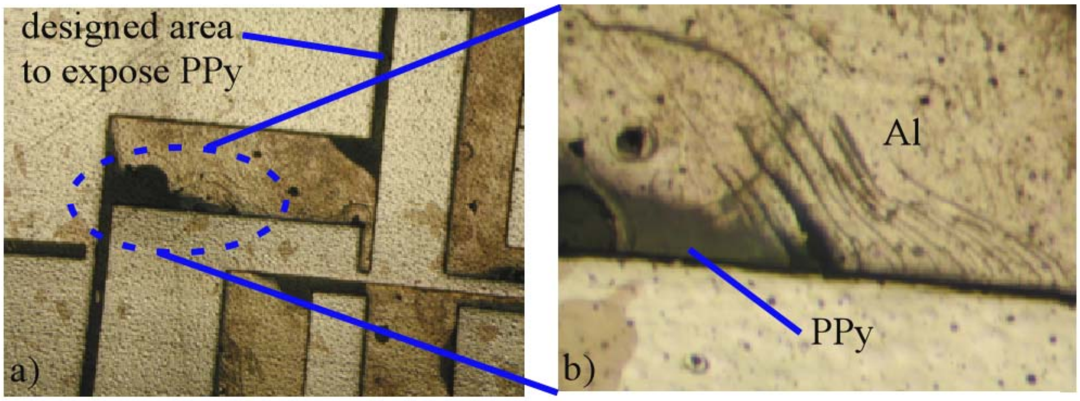

Figure 119. a) The photo shows the Al close to the exposed PPy came off during patterning. The close view b) shows the Al wrinkled and cracked, which implies the Al plastically deformed and then mechanically failed. The delamination may due to the swelling of PPy.

By carefully observing Figure 119, it can be seen that the Al wrinkled and cracked, which implies that plastic deformation and mechanical failure cause the delamination of the Al. In particular, the delamination took place close to the areas that were designed to expose PPy. Because Al was photolithographically patterned by immersing the sample into a photoresist developer (Shipley CD-30), and then the Al etchant, it is possible that there was an inconsistent swelling of Al and PPy due to absorbing solutions. Experiments were performed to verify this speculation.

In order to test PPy swelling, PPy was deposited onto a patterned Au layer. The thickness of PPy was measured by using a profilometer. After immersing samples into the photoresist developer for 30 seconds and the Al etchant for 5 minutes (5 samples of each test), the thickness of PPy was measured again. The operation time of 30 seconds and 5 minutes was the same as the time used in the real fabrication. The measured values are shown in Figure 120. PPy swelled ~ 30% after immersing in the Al etchant, which is beyond the ductility limit of Al [208]. In contrast, there was no obvious difference from the data of immersing Al in the photoresist developer. Hence, it was PPy swelling in the Al etchant that resulted in the Al delamination during patterning.

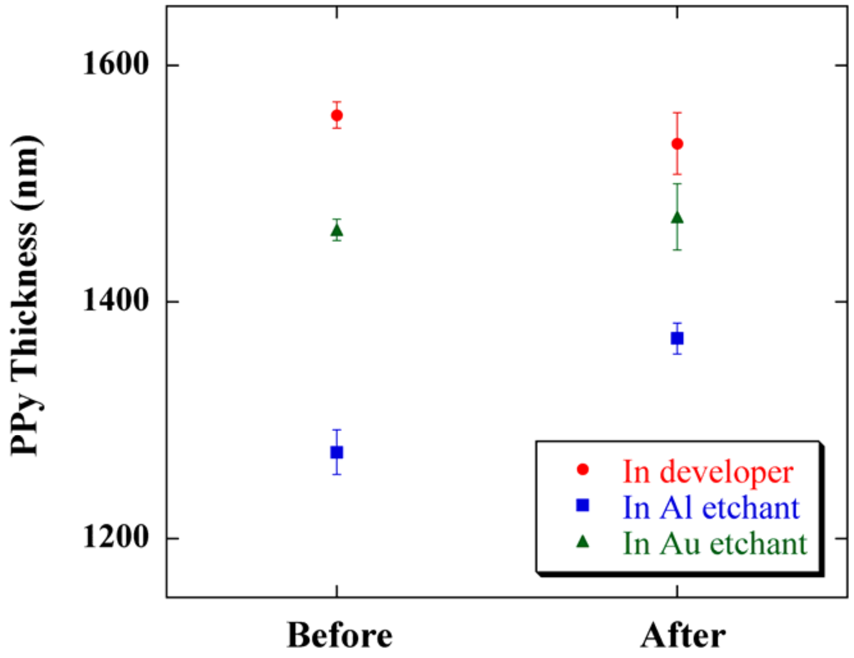

Figure 120. The thickness changing of PPy before and after immersing in the developer (circle), the Al etchant (square), and the Au etchant (triangle). The data show PPy swelled 30% in the Al etchant, which is the reason of Al coming off from PPy. There is almost no difference in the developer and Au etchant, so using Au as the RIE mask will not generate delamination.

In order to get rid of Al from the fabrication process, Au was used as the RIE mask material. Through the similar test as above, PPy only swelled a little in the Au etchant (Figure 120). As a result, Au replaced Al as the RIE mask in the second-generation process. During removing the Au on PPy after RIE, the structural Au in the bilayers was protected by the adhesion promoter Cr layer, so the bilayers were intact. Note that because the Cr layer was thin, 100 Å, the bending behavior of the PPy/Au bilayers was not affected. In summary, the second-generation process is illustrated in Figure 121.

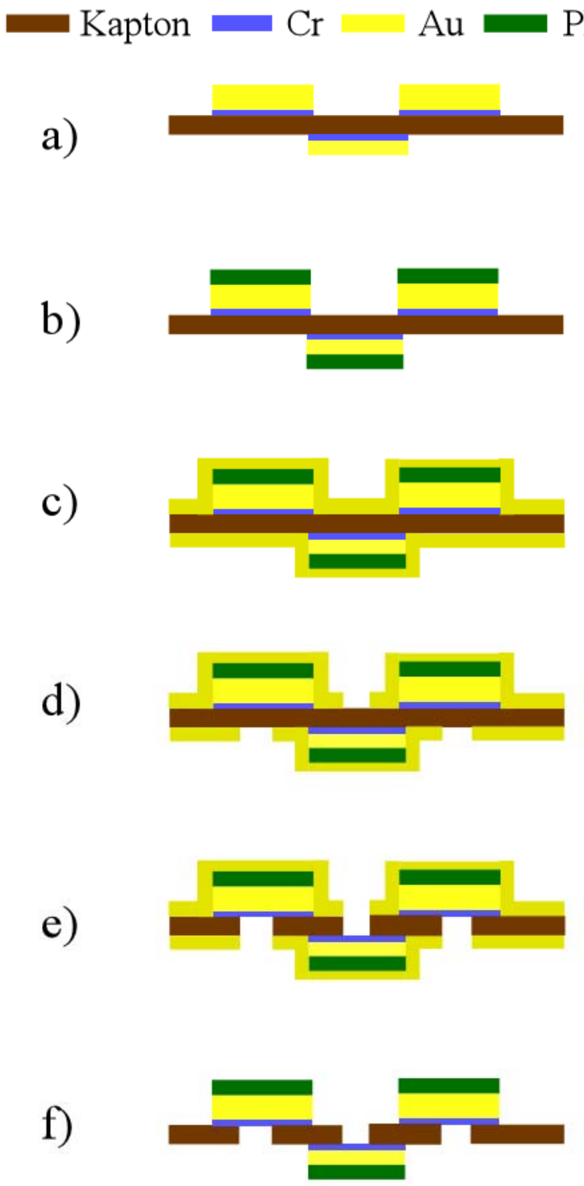

Figure 121. Schematic of the improved second-generation process. The improvement is illustrated at 1) deposit a Cr layer as the adhesion promoter between Au and PPy (a); 2) evaporate and pattern Au on the both sides of the substrate as the RIE mask (c-e).

Appendix E Patterning of SU8-5

The datasheet [205] from the manufacturer (Microchem Inc., Newton, MA, USA), and the processing procedure described in the literature ([45, 206]), did not work in our clean room. With the help from Mr. Sheng Li of Prof. Ghodssi's group (Electrical and Computer Engineering, UMCP), a recipe was obtained to pattern 10 μm thick SU8-5.

Table 5 compares my recipe with the company's datasheet. The key difference came from the coating thickness. The SU8-5 film was not 10 μm but 5 μm thick after spinning at 3000 rpm. Hence, the spinning speed was lowered for a thicker film, and the corresponding baking time, exposure dose, and developing time were increased. In order to reduce thermal stress, a ramping process was used to heat up and cool down SU8 during baking. The operation details are introduced below.

Table 5. A comparison between the company's datasheet and my recipe of patterning 10 μm thick SU8-5.

	Spin	**Soft Bake**	**Expose**	**Post Bake**	**Develop**
Microchem® Datasheet [205]	Ramp to 500 rpm over 5 seconds, then ramp to 3000 rpm over 8 seconds.	At 65 °C for 2 minutes, then at 95 °C for 5 minutes.	100 mJ/cm^2 at 365 nm	At 65 °C for 1 minute, then at 95 °C for 2 minutes.	2 minutes
My Recipe	Ramp to 500 rpm over 10 seconds, then ramp to 3000 rpm over 20 seconds.	Ramp to 95 °C with the ramp rate of 5 °C/min; keep 95 °C for 30 minutes.	250 mJ/cm^2 at 365 nm	Ramp to 95 °C with the ramp rate of 5 °C/min; keep 95 °C for 30 minutes.	5 minutes

Spin

Before spinning, SU8 was dropped, not sucked out, onto the substrate with a clean plastic pipette to avoid introducing air bubbles into the SU8. Since SU8-5 is viscous, it took about 1 minute for SU8 to flow around the substrate surface and the layer to become flat and even. In order to cover the whole surface of the substrate after spinning, SU8 should occupy at least 90% of the surface area.

In order to obtain a layer with uniform thickness, SU8 was not spun under a constant speed. The spinning procedure was composed of two steps: the spin rate was raised from 0 to 500 rounds per minute (rpm) over 10 seconds, and then raised to 1,500 rpm over 20 seconds. The first step was to drive SU8 to cover the whole surface area, and the second step was to cast off extra SU8 for a final thickness of 10 μm.

Soft Bake

After spinning, the sample was baked on a programmable hotplate (PMC DATAPLATE^{TM} 720, Barnstead International Inc., Dubuque, IA). The baking temperature rose from room temperature to 95 °C with a ramp rate of 5 °C/min. The sample was kept at 95 °C for 30 minutes, and then cooled down to room temperature in 30 minutes (Figure 122).

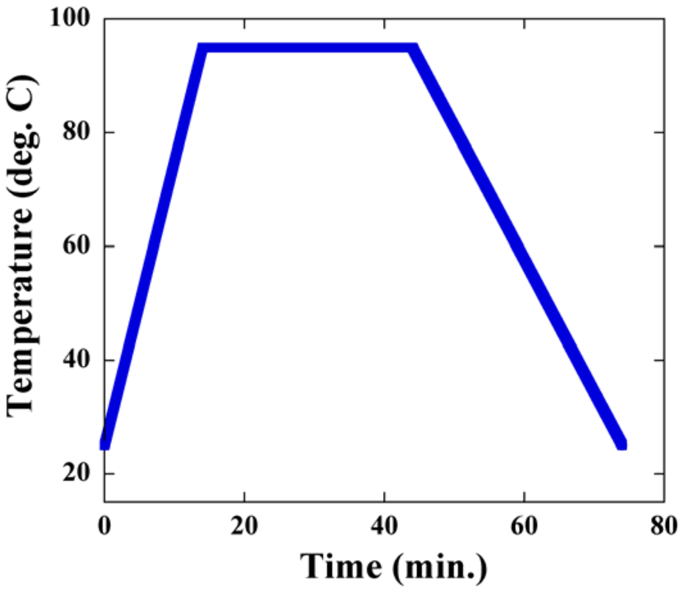

Figure 122. SU8-5 baking procedure. The sample was heated from room temperature to 95 °C, remained at 95 °C for 30 minutes, and then cooled.

Expose

The exposure dose was 250 mJ/cm^2 at 365 nm (Karl Suss MJB-3 mask aligner, SUSS MicroTec AG, Germany). A lower exposure dose resulted in incomplete crosslinking of SU8, while a higher does generated larger dimensions of the structures.

Post Bake

The procedure was the same as that of the soft bake.

Develop

The sample was developed in SU8 developer (Microchem Inc., MA, USA) for 5 minutes. After developing, the sample was dried under a stream of nitrogen.

Descum

A short oxygen plasma etch can remove the scum (leftover at the edges of SU8 structures after developing). I used RIE (Jupiter III, March Instruments Inc., Concord, CA) at 200 W of power and 0.3 mtorr of chamber pressure for 30 seconds.

Appendix F Photolithography Masks

During the microfabrication, two kinds of photolithography masks were used. One was a transparency mask; the other was a Cr/glass mask.

Transparency Mask

The software package Illustrator® (version 9.0, Adobe Inc., San Jose, CA) was used to draw the patterns for photolithography. The drawings were sent to R. G. M. Graphics Inc. (Bethesda, MD) to fabricate the transparency mask. The mask was inexpensive ($30 for a sheet of 8.5 inch × 11 inch) and fast to make (about half an hour). However, the minimum feature size to be resolved on the mask is about 30 μm; there always exists around 10 μm dimension error. Thus, the mask was only suitable for testing the design and fabrication of MEMS prototype.

Cr/Glass Mask

A Cr/glass mask was employed to fabricate microstructures that required high accuracy (such as the bilayers for characterizing bending performance in Chapter 5 Chapter 6) and tiny feature size (such as the microstructures on the CMOS chips). The Cr/glass mask can be designed by most CAD software such as AutoCAD® (Autodesk Inc., San

Rafael, CA). Since the microstructures were fabricated on CMOS chips, the mask had to be compatible with the chip layout (such as the position and size of sensing electrodes). Prof. Abshire's group designed the chip layout and circuitry by using a software called Cadence® (Cadence Design Systems Inc., San Jose, CA). Thus, Cadence® was used to draw the Cr/glass masks. The masks (minimum feature size 5 μm, dimension error ±1 μm) were fabricated by Photo Sciences Inc. (Torrance, CA).

Appendix G Electroless Plating of Au on Al

Plate Zn on Al

Zn was plated on Al surface as an intermediate layer. The volume of solutions listed below can accommodate samples with a total surface area up to 100 mm^2. If samples with the larger surface area are to be plated, the solution volume needs to increase by proportion.

- Put 30.0 mL DI H_2O into a beaker.
- Put 12.0 mL Techni EN Zincate solution into the beaker.
- Stir the mixture at 200 rpm for 5 minutes.
- Put in a chip for 30 seconds.
- Take out the chip, rinse with DI H_2O.

Zn of 50 Å was plated on top of Al.

Plate Ni on Zn

Ni was then plated on Zn surface as another intermediate layer.

- Put 31.6 mL DI H_2O into another beaker.
- Add 2.4 mL Techni EN 2600A solution.
- Add 6.0 mL Techni EN 2600B solution.
- Stir the mixture at ~200 rpm for 5 minutes.
- Measure pH by using a pH meter (Type 720, Thermo Orion Inc., Beverly, MA). The pH should be 4.9. If the measured value does not equal 4.9, use 50% ammonium hydroxide to raise or 25% sulfuric acid to lower pH.
- Cover the beaker, heat up to 190˚F (= 87.8˚C).
- Put in the chip; manually shake the beaker every 2 minutes. The plate rate was 0.3 μm/min. Usually, 5 μm thick Ni was plated on Zn for a good adhesion.
- Take out the chip, rinse with DI H_2O.

After this step, a layer of Ni was coated on Zn. Note the agitation (manual shaking) was necessary. Without the agitation, Ni connected electrodes.

Plate Au on Ni

Au was plated on the intermediate layer Ni.

- Put 23.4 mL DI H_2O into another beaker.
- Add 23.4 mL Oromerse SO part A solution.
- Add 3.3 mL Oromerse SO part B solution.
- Stir the mixture at 200 rpm for 5 minutes.
- Measure pH by using the pH meter. The pH should be among the range from 8.8 to 9. If the measured value is out of range, use 10% sodium hydroxide to raise or citric acid to lower pH.
- Cover the beaker, heat up to 158-164˚F (= 70-73˚C).
- Put in the chip; manually shake the beaker every 2 minutes. The plate rate was 0.2 μm/min. Usually, at least 2 μm thick Au was plated on Ni for a good

adhesion.

- Take out the chip, rinse with DI H_2O, dry with N_2.

References

[1] E. Smela, O. Inganäs, Q. Pei, and I. Lundström, "Electrochemical muscles: micromachining fingers and corkscrews," *Adv. Mat.*, vol. 5, pp. 630-632, 1993.

[2] E. Smela, O. Inganäs, and I. Lundström, "Controlled folding of micrometer-size structures," *Science*, vol. 268, pp. 1735-1738, 1995.

[3] E. Smela, "Conjugated polymer actuators for biomedical applications," *Adv. Mat.*, vol. 15, pp. 481-494, 2003.

[4] G. B. Street, "Polypyrrole, from powders to plastics," in *Handbook of Conducting Polymers*, vol. 1, T. A. Skotheim, Ed. New York: Marcel Dekker, Inc., 1986, pp. 265-291.

[5] J. R. Reynolds, "Electrically conductive polymers," in *Chemtech*, 1988, pp. 440-447.

[6] A. F. Diaz, K. K. Kanazawa, and G. P. Gardini, "Electrochemical polymerization of pyrrole," *J. Chem. Soc., Chem. Comm.*, vol. 14, pp. 635-636, 1979.

[7] J. P. Schaffer, A. Saxena, S. D. Antolovich, J. T. H. Sanders, and S. B. Warner, "Electrical conduction," in *The Science and Design of Engineering Materials, Second Ed.*: McGraw-Hill Inc., 1999, pp. 430.

[8] G. G. Wallace, G. M. Spinks, L. A. P. Kane-Maguire, and P. R. Teasdale,

"Assembly of polypyrrole," in *Conductive Electroactive Polymers: Intelligent Materials Systems, Second Ed.* Boca Raton, FL, USA: CRC Press LLC, 2003, pp. 51-88.

[9] A. F. Diaz and J. Bargon, "Electrochemical synthesis of conducting polymers," in *Handbook of Conducting Polymers*, vol. 1, T. A. Skotheim, Ed. New York: Marcel Dekker, Inc., 1986, pp. 81-115.

[10] E. Smela, "Microfabrication of PPy microactuators and other conjugated polymer devices," *J. Micromech. Microeng.*, vol. 9, pp. 1-18, 1999.

[11] Q. Pei and O. Inganäs, "Electrochemical applications of the bending beam method. 2. Electroshrinking and slow relaxation in polypyrrole," *J. Phys. Chem.*, vol. 97, pp. 6034-6041, 1993.

[12] K. B. Oldham and J. C. Myland, "Reference electrodes," in *Fundamentals of Electrochemical Science*. San Diego, CA, USA: Academic Press, Inc., 1994, pp. 116.

[13] X. Wang, B. Shapiro, and E. Smela, "Visualizing ion transport in conjugated polymers," *Adv. Mat.*, vol. 16, pp. 1605-1609, 2004.

[14] M. K. Song, M. S. Gong, and H. W. Rhee, "Anion movement in polypyrrole films prepared in lithium dodecylsulfate aqueous solutions," *Molecular Crystals and Liquid Crystals Science and Technology Section A - Molecular Crystals and Liquid Crystals*, vol. 280, pp. 145-150, 1996.

[15] R. C. D. Peres, M.-A. De Paoli, and R. M. Torresi, "The role of ion exchange in the redox processes of polypyrrole/dodecyl sulfate films as studied by

electrogravimetry using a quartz crystal microbalance," *Synth. Met.*, vol. 48, pp. 259, 1992.

[16] X. Wang, E. Smela, and B. Shapiro, "Understand Ion Transport in Conjugated Polymers," presented at SPIE 12th Annual International Symposium: Smart Structures and Materials, San Diego, California USA, 2005.

[17] Q. Pei and O. Inganäs, "Electrochemical applications of the bending beam method; a novel way to study ion transport in electroactive polymers," *Sol. State Ion.*, vol. 60, pp. 161-166, 1993.

[18] E. Smela, M. Kallenbach, and J. Holdenried, "Electrochemically driven polypyrrole bilayers for moving and positioning bulk micromachined silicon plates," *J. Microelectromech. Sys.*, vol. 8, pp. 373-383, 1999.

[19] Q. Pei and O. Inganäs, "Electrochemical applications of the bending beam method. 1. Mass transport and volume changes in polypyrrole during redox," *J. Phys. Chem.*, vol. 96, pp. 10507-10514, 1992.

[20] T. F. Otero, E. Angulo, J. Rodriguez, and C. Santamaria, "Electrochemomechanical properties from a bilayer: polypyrrole/non-conducting and flexible material -- artificial muscle," *J. Electroanal. Chem.*, vol. 341, pp. 369-375, 1992.

[21] J. Joo and M. Pyo, "Effects of cationic species on strain changes of polypyrrole doped with perchlorate ions," *Electrochem. Sol. State Lett.*, vol. 6, pp. E27-E29, 2003.

[22] P. Murray, G. M. Spinks, G. G. Wallace, and R. P. Burford, "Electrochemical

induced ductile-brittle transition in tosylate-doped (pTS) polypyrrole," *Synth. Met.*, vol. 97, pp. 117-121, 1998.

[23] L. Bay, N. Mogensen, S. Skaarup, P. Sommer-Larsen, M. Jorgensen, and K. West, "Polypyrrole doped with alkyl benzenesulfonates," *Macromole.*, vol. 35, pp. 9345-9351, 2002.

[24] A. F. Diaz and J. I. Castillo, "A polymer electrode with variable conductivity: polypyrrole," *J. C. S. Chem. Comm.*, vol. 9, pp. 397-398, 1980.

[25] S. B. Saidman, "Influence of anion and pH on the electrochemical behaviour of polypyrrole synthesised in alkaline media," *Electrochi. Acta*, vol. 48, pp. 1719-1726, 2003.

[26] S. Shimoda and E. Smela, "The effect of pH on polymerization and volume change in PPy(DBS)," *Electrochim. Acta*, vol. 44, pp. 219-238, 1998.

[27] J. F. Rusling and S. L. Suib, "Characterizing materials with cyclic voltammetry," *Adv. Mat.*, vol. 6, pp. 922, 1994.

[28] A. F. Diaz and J. Bargon, "Electroactivity and conductivity," in *Handbook of conducting Polymers, Vol. 1*. New York, USA: Marcel Dekker, Inc., 1986, pp. 95-97.

[29] S. W. Feldberg, "Reinterpretation of polypyrrole electrochemistry. Consideration of capactive currents in redox switching of conducting polymers," *J. Am. Chem. Soc.*, vol. 106, pp. 4671 - 4674, 1984.

[30] G. M. Spinks, D. Zhou, L. Liu, and G. G. Wallace, "The amounts per cycle of polypyrrole electromechanical actuators," *Smart Mater. Struct.*, vol. 12, 2003.

[31] J. Ding, L. Liu, G. M. Spinks, D. Zhou, G. G. Wallace, and J. Gillespie, "High performance conducting polymer actuators utilizing a tubular geometry and helical wire interconnects," *Synth. Met.*, vol. 138, pp. 391-398, 2003.

[32] S. Hara, T. Zama, A. Ametani, W. Takashima, and K. Kaneto, "Enhancement in electrochemical strain of a polypyrrole-metal composite film actuator," *J. Mater. Chem.*, vol. 14, pp. 2724-2725, 2004.

[33] Y. Berdichevsky and Y.-H. Lo, "Polymer microvalves based on anisotropic expansion of polypyrrole," presented at Materials Research Society 2004 Spring Meeting, San Francisco, CA, USA, 2004.

[34] A. Della Santa, D. De Rossi, and A. Mazzoldi, "Performances and work capacity of a polypyrrole conducting polymer linear actuator," *Synth. Met.*, vol. 90, pp. 93-100, 1997.

[35] G. G. Wallace, H. Zhao, C. O. Too, and C. J. Small, "Novel conducting polymer-polyelectrolyte composites," *Synth. Met.*, vol. 84, pp. 323-6, 1997.

[36] K. Kaneto, M. Kaneko, Y. Min, and A. G. MacDiarmid, ""Artificial muscle": electromechanical actuators using polyaniline films," *Synth. Met.*, vol. 71, pp. 2211, 1995.

[37] Q. Pei and O. Inganäs, "Conjugated polymers and the bending cantilever method: electrical muscles and smart devices," *Adv. Mat.*, vol. 4, pp. 277-278, 1992.

[38] H. Okuzaki, T. Kuwabara, and T. Kunugi, "Theoretical study of sorption-induced bending of polypyrrole films," *J. Polym. Sci.: B: Polym. Phy.*, vol. 36, pp. 2237-2246, 1998.

[39] H. Okuzaki and T. Kunugi, "Adsorption-induced bending of polypyrrole films and its applicaiton to a chemomechanical rotor," *J. Polym. Sci.: B: Polym. Phy.*, vol. 34, pp. 1747-1749, 1996.

[40] T. F. Otero and M. T. Cortes, "Artificial muscle: movement and position control," *Chem. Commun.*, pp. 284-285, 2004.

[41] T. F. Otero and M. T. Cortes Montanes, "Characterization of triple layers," presented at Proc. SPIE-Int. Soc. Opt. Eng., 2001.

[42] T. F. Otero and M. T. Cortés, "Artificial muscles with tactile sensitivity," *Adv. Mat.*, vol. 15, pp. 279-282, 2003.

[43] E. W. H. Jager, O. Inganas, and I. Lundstrom, "Microrobots for micrometer-size objects in aqueous media: potential tools for single-cell manipulation," *Science*, vol. 288, pp. 2335-2338, 2000.

[44] E. Smela, O. Inganäs, and I. Lundström, "Micro-robot controlled by conducting polymer muscles: multi-hinged, folding actuators," presented at International Symposium on Microsystems, Intelligent Materials, and Robots, Sendai, Japan, 1995.

[45] E. W. H. Jager, C. Immerstrand, K. H. Peterson, K. Magnusson, I. Lundstrom, and O. Inganas, "The cell clinic: closable microvials for single cell studies," *Biomed. Microdev.*, vol. 4, pp. 177-187, 2002.

[46] Y. Liu, E. Smela, N. M. Nelson, and P. Abshire, "Cell-lab on a chip: a CMOS-based microsystem for culturing and monitoring cells," presented at IEEE EMBC 2004: 26th Int'l Conf. IEEE Eng. Med. Bio. Soc., San Francisco, CA, USA, 2004.

[47] M. Urdaneta, Y. Liu, M. Christophersen, S. Prakash, P. Abshire, and E. Smela, "Integrating conjugated polymer microactuators with CMOS sensing circuitry for studying living cells," presented at SPIE's 12th Annual Int'l. Symposium on Smart Structures and Materials, EAPAD, San Diego, CA, 2005.

[48] L. H. Oh, "Development of micro-valves actuated by polypyrrole/gold bilayers," in *Mechanical Engineering*. College Park, Maryland, USA: University of Maryland, 2003.

[49] J. Park, S. Jung, Y. Kim, B. Kim, S. Lee, and J. Park, "Design and fabrication of an integrated cell processor for single embryo cell manipulation," *Lab Chip*, vol. 5, pp. 91-96, 2005.

[50] H. Tsai, H. Xu, J. Zoval, and M. Madou, "Bi-layer polypyrrole artificial muscle valves for drug delivery systems," presented at SPIE's 12th Annual Int'l. Symposium on Smart Structures and Materials, EAPAD, San Diego, CA, 2005.

[51] H. Andersson and A. v. d. Berg, "Microtechnologies and nanotechnologies for single-cell analysis," *Curr. Opin. Biotech*, vol. 15, pp. 44-49, 2004.

[52] G. M. Walker, H. C. Zeringue, and D. J. Beebe, "Microenvironment design considerations for cellular scale studies," *Lab Chip*, vol. 4, pp. 91-97, 2004.

[53] H. Yu, I. A. Shkel, and D. J. Beebe, "Effect of microchannel geometry on cell proliferation: experiments and interpretation," presented at MicroTAS 2004: 8th Int'l Conf. Micro Total Anal. Sys., Malmo, Sweden, 2004.

[54] S. Krawczyk, "Discussion on optical integration in Lab-on-a-Chip microsystems for medical diagnosis," *Phys. Stat. Sol. (c)*, pp. 998-1012, 2003.

[55] A. Manz, N. Graber, and H. M. Widmer, "Miniaturized total chemical analysis systems: a novel concept for chemical sensing," *Sens. Act. B*, vol. 1, pp. 244-248, 1990.

[56] E. Cukierman, R. Pankov, and K. M. Yamada, "Cell interactions with three-dimensional matrices," *Curr. Opin. Cell Bio.*, vol. 14, pp. 633-639, 2002.

[57] A. Abbott, "Biology's new dimension," *Nature*, vol. 424, pp. 870-872, 2003.

[58] B. Alberts, D. Bray, A. Johnson, J. Lewis, M. Raff, K. Roberts, and P. Walter, "Cell communication," in *Essential Cell Biology*. New York: Garland Publishing, Inc., 1998, pp. 481.

[59] H. Baltes, A. Koll, and D. Lange, "The CMOS MEMS nose - fact or fiction?," presented at ISIE 1997: IEEE Int'l Symp. Indus. Elec., Guimaraes, Portugal, 1997.

[60] E. L. Hines, E. Llobet, and J. W. Gardner, "Electronic noses: a review of signal processing techniques," *IEEE Proc. Cir. Dev. Sys.*, vol. 146, pp. 297 - 310, 1999.

[61] R. Gutierrez-Osuna, "Pattern analysis for machine olfaction: a review," *IEEE Sens. J.*, vol. 2, pp. 189 - 202, 2002.

[62] D. Harwood, "Something in the air," *IEEE Rev.*, vol. 47, pp. 10-14, 2001.

[63] E. Lauwers, J. Suls, W. Gumbrecht, D. Maes, G. Gielen, and W. Sansen, "A CMOS multiparameter biochemical microsensor with temperature control and signal interfacing," *IEEE J. Sol.-Sta. Cir.*, vol. 36, pp. 2030 - 2038, 2001.

[64] P. A. Hammond, D. Ali, and D. R. S. Cumming, "Design of a single-chip pH sensor using a conventional 0.6-μm CMOS process," *IEEE Sens. J.*, vol. 4, pp.

706 - 712, 2004.

[65] G. Lu, G. Guillaud, G. Sou, F. Devigny, M. Pitaval, and P. Morin, "Investigation of CMOS BDJ detector for fluorescence detection in microarray analysis," presented at IEEE EMBS '00: 1st Ann. Int'l Conf. Microtech. Med. Bio., Lyon, France, 2000.

[66] H.-C. Jiang and C.-Y. Wu, "The BJT-based silicon-retina sensory system for direction- and velocity-selective sensing," presented at IEEE ISCAS '98: Int'l Symp. Cir. Sys., Monterey, CA, 1998.

[67] W. H. Baumann, E. Schreiber, G. Krause, A. Podssun, S. Homma, R. Schrott, R. Ehret, I. Freund, and M. Lehmann, "Cell monitoring system with multiparametric CMOS sensorchips," presented at MicroTAS 2004: 8th Int'l Conf. Micro Total Anal. Sys., Malmo, Sweden, 2004.

[68] M. P. Maher, J. Pine, J. Wright, and Y.-C. Tai, "The neurochip: a new multielectrode device for stimulating and recording from cultured neurons," *J. Neuro. Meth.*, vol. 87, pp. 45-56, 1999.

[69] D. G. Grier, "A revolution in optical manipulation," *Nature*, vol. 424, pp. 810-816, 2003.

[70] G. Medoro, N. Manaresi, A. Leonardi, L. Altomare, M. Tartagni, and R. Guerrieri, "A lab-on-a-chip for cell detection and manipulation," *IEEE Sens. J.*, vol. 3, pp. 317-325, 2003.

[71] C. R. Keese and I. Giaever, "A biosensor that monitors cell morphology with electrical fields," *IEEE Eng. Med. Bio.*, vol. 13, pp. 402-408, 1994.

[72] G. Fuhr, T. Muller, T. Schnelle, H. Glasser, J. Gimsa, U. Hofmann, and B. Wagner, "Handling and investigation of adherently growing cells and viruses of medical relevance in three-dimensional micro-structures," presented at IEEE MEMS'97, Hotel Nagoya Castle, Japan, 1997.

[73] R. I. Freshney, "Biology of cultured cells," in *Culture of Animal Cells: a Manual of Basic Technique*, Fourth ed. New York: Wiley-Liss, 2000, pp. 9.

[74] G. M. Walker, M. S. Ozers, and D. J. Beebe, "Insect cell culture in microfluic channels," *Biomed. Microdev.*, vol. 4, pp. 161-166, 2002.

[75] B. Alberts, D. Bray, A. Johnson, J. Lewis, M. Raff, K. Roberts, and P. Walter, "Cell division," in *Essential Cell Biology*. New York: Garland Publishing, Inc., 1998, pp. 549.

[76] R. I. Freshney, "Routine maintenance," in *Culture of Animal Cells: a Manual of Basic Technique*, Fourth ed. New York: Wiley-Liss, 2000, pp. 181.

[77] R. S. Muller, T. I. Kamins, and M. Chan, "Junction breakdown," in *Device Electronics for Integrated Circuits*. New York: John Wiley & Sons, Inc., 2003, pp. 203-212.

[78] R. I. Freshney, "Media," in *Culture of Animal Cells: a Manual of Basic Technique*, Fourth ed. New York: Wiley-Liss, 2000, pp. 92.

[79] W. C. Tang, H. Nguyen, and M. W. Judy, "Electrostatic-comb drive of lateral polysilicon resonators," *Sens. Act. A*, vol. 21, pp. 328-331, 1990.

[80] H. Ahmed and W. A. Moussa, "Optimizing the performance of electrostatic comb-drive actuators using neural networks," presented at ICMENS 2003: IEEE

Int'l Conf. MEMS, NANO, Smart Sys., Banff, Alberta, Canada, 2003.

[81] G. T. A. Kovacs, "Piezoelectric Effect," in *Micromachined Transducers Sourcebook*. Boston: WCB McGraw-Hill, 1998, pp. 215.

[82] Y. Haddab, N. Chaillet, and A. Bourjault, "A microgripper using smart piezoelectric actuators," presented at IROS 2000: IEEE Int'l Conf. Intel. Robots & Sys., Takamatsu, Japan, 2000.

[83] W. Riethmuller and W. Benecke, "Thermally excited silicon microactuators," *IEEE Trans. Elec. Dev.*, vol. 35, pp. 758-763, 1988.

[84] P. Krulevitch, A. P. Lee, P. B. Ramsey, J. C. Trevino, J. Hamilton, and M. A. Northrup, "Thin film shape memory alloy microactuators," *J. Microelectromech. Sys.*, vol. 5, pp. 270-282, 1996.

[85] J. M. Maloney, D. S. Schreiber, and D. L. DeVoe, "Large-force electrothermal linear micromotors," *J. Micromech. Microeng.*, vol. 14, pp. 226-234, 2004.

[86] M. M. I. Bhuiyan, Y. Haga, and M. Esashi, "Large displacement optical switching mechanism using SMA microactuator and magnetic latch," presented at MEMS 2004: 17th IEEE Int'l Conf. MEMS, Maastricht, Netherlands, 2004.

[87] J. W. Suh, C. W. Storment, and G. T. A. Kovacs, "Characterization of multi-segment organic thermal actuators," presented at Transducers'95: 8th Int'l Conf. Solid-State Sens. Actua., Stockholm, Sweden, 1995.

[88] A. P. Lee, D. R. Ciarlo, P. A. Krulevitch, S. Lehew, J. Trevino, and M. A. Northrup, "A practical microgripper by fine alignment, eutectic bonding and SMA actuation," presented at Transducers'95: 8th Int'l Conf. Solid-State Sens.

Actua., Stockholm, Sweden, 1995.

[89] J. W. Judy and R. S. Muller, "Magnetically actuated, addressable microstructures," *IEEE J. MEMS*, vol. 6, pp. 249 - 256, 1997.

[90] J. W. Judy and R. S. Muller, "Magnetic microactuation of torsional polysilicon structures," *Sens. Act. A*, vol. 53, pp. 392-396, 1996.

[91] A. E. English, T. Tanaka, and E. R. Edelman, "Equilibrium and non-equilibrium phase transitions in copolymer polyelectrolyte hydrogels," *J. Chem. Phys.*, vol. 107, pp. 1645-1654, 1997.

[92] T. Tanaka, I. Nishio, S. Sun, and S. Ueno-Nishio, "Collapse of gels in an electric field," *Science*, vol. 218, pp. 467-469, 1982.

[93] A. Suzuki and T. Tanaka, "Phase transition in polymer gels induced by visible light," *Nature*, vol. 346, pp. 345-347, 1990.

[94] Z. Hu, X. Zhang, and Y. Li, "Synthesis and application of modulated polymer gels," *Science*, vol. 269, pp. 525-527, 1995.

[95] M. Annaka and T. Tanaka, "Multiple phases of polymer gels," *Nature*, vol. 355, pp. 430-432, 1992.

[96] K. Kataoka, H. Miyazaki, M. Bunya, T. Okano, and Y. Sakurai, "Totally synthetic polymer gels responding to external glucose concentration: their preparation and application to on-off regulation of insulin release," *J. Ame. Chem. Soc.*, vol. 120, pp. 12694-12695, 1998.

[97] T. Miyata, N. Asami, and T. Uragami, "A reversibly antigen-responsive hydrogel," *Nature*, vol. 399, pp. 766-769, 1999.

[98] N. A. Peppas and R. Langer, "New challenges in biomaterials," *Science*, vol. 263, pp. 1715-1720, 1994.

[99] R. H. Liu, Q. Yu, and D. J. Beebe, "Fabrication and characterization of hydrogel-based microvalves," *IEEE J. MEMS*, vol. 11, pp. 45-53, 2002.

[100] S. K. De, N. R. Aluru, B. Johnson, W. C. Crone, D. J. Beebe, and J. Moore, "Equilibrium swelling and kinetics of pH-responsive hydrogels: models, experiments, and simulations," *IEEE J. MEMS*, vol. 11, pp. 544 - 555, 2002.

[101] D. J. Beebe, J. S. Moore, J. M. Bauer, Q. Yu, R. H. Liu, C. Devadoss, and B. H. Jo, "Functional hydrogel structures for autonomous flow control inside microfluidic channels," *Nature*, vol. 404, pp. 588-590, 2000.

[102] M. Lei, A. Salim, R. A. Siegel, and B. Ziaie, "A hydrogel-actuated microvalve for smart flow control," presented at IEEE EMBC 2004: 26th Int'l Conf. IEEE Eng. Med. Bio. Soc., San Francisco, CA, USA, 2004.

[103] A. Baldi, Y. Gu, P. Loftness, R. A. Siegel, and B. Ziaie, "A hydrogel-actuated environmentally sensitive microvalve for active flow control," *J. Microelectromech. Sys.*, vol. 12, pp. 613-621, 2003.

[104] R. I. Freshney, "Physicochemical properties: pH," in *Culture of Animal Cells: a Manual of Basic Technique*, Fourth ed. New York: Wiley-Liss, 2000, pp. 89.

[105] R. B. Kaner and A. G. MacDiarmid, "Plastics that conduct electricity," in *Sci. Amer.*, 1988, pp. 60-65.

[106] X. Cui and D. C. Martin, "Fuzzy gold electrodes for lowering impedance and improving adhesion with electrodeposited conducting polymer films," *Sens. Act.*

A, vol. 102, pp. 384-394, 2003.

[107] M. Pyo, C. C. Bohn, E. Smela, J. R. Reynolds, and A. B. Brennan, "Direct strain measurement of polypyrrole actuators controlled by the polymer/gold interface," *Chem. Mater.*, vol. 15, pp. 916-922, 2003.

[108] E. W. H. Jager, E. Smela, and O. Inganäs, "Microfabricating conjugated polymer actuators," *Science*, vol. 290, pp. 1540-1545, 2000.

[109] Y. Liu and B. Hwang, "Mechanism of conductivity decay of polypyrrole exposed to water and enhancement of conductivity stability of copper(I)-modified polypyrrole," *J. Electroanal. Chem.*, vol. 501, pp. 100-106, 2001.

[110] K. G. Neoh, K. K. S. Lau, V. V. T. Wong, and E. T. Kang, "Structure and degradation behavior of polypyrrole doped with sulfonate anions of different sizes subjected to undoping-redoping cycles," *Chem. Mater.*, vol. 8, pp. 167-172, 1996.

[111] W. Lu, A. G. Fadeev, B. Qi, E. Smela, B. R. Mattes, J. Ding, G. M. Spinks, J. Mazurkiewicz, D. Zhou, G. G. Wallace, D. R. MacFarlane, S. A. Forsyth, and M. Forsyth, "Use of ionic liquids for Pi-conjugated polymer electrochemical devices," *Science*, vol. 297, pp. 983-987, 2002.

[112] J. Ding, D. Zhou, G. M. Spinks, G. G. Wallace, S. Forsyth, M. Forsyth, and D. MacFarlane, "Use of ionic liquids as electrolytes in electromechanical actuator systems based on inherently conducting polymers," *Chem. Mater.*, vol. 15, pp. 2392-2398, 2003.

[113] J. Fuller, A. C. Breda, and R. T. Carlin, "Ionic liquid-polymer gel electrolytes from hydrophilic and hydrophobic ionic liquids," *J. Electroanal. Chem.*, vol. 459,

pp. 29-34, 1998.

[114] R. H. Baughman, "Conducting polymer artificial muscles," *Synth. Met.*, vol. 78, pp. 339-353, 1996.

[115] J. D. Madden, R. A. Cush, T. S. Kanigan, and I. W. Hunter, "Fast contracting polypyrrole actuators," *Synth. Met.*, vol. 113, pp. 185-192, 2000.

[116] T. F. Otero and J. M. Sansiñena, "Bilayer dimensions and movement in artificial muscles," *Bioelectrochem. Bioenerg.*, vol. 42, pp. 117-122, 1997.

[117] A. Della Santa, D. De Rossi, and A. Mazzoldi, "Characterization and modelling of a conducting polymer muscle-like linear actuator," *Smart Mater. Struct.*, vol. 6, pp. 23-34, 1997.

[118] G. M. Spinks, B. Xi, D. Zhou, V.-T. Truong, and G. G. Wallace, "Enhanced control and stability of polypyrrole electromechanical actuators," *Synth. Met.*, vol. 140, pp. 273-280, 2004.

[119] Y. Sonoda, W. Takashima, and K. Kaneto, "Characteristics of soft actuators based on polypyrrole films," *Synth. Met.*, vol. 119, pp. 267-268, 2001.

[120] M. Benslimane, P. Gravesen, K. West, S. Skaarup, and P. S. Larsen, "Performance of polymer based actuators: the three-layer model," presented at Proc. SPIE-Int. Soc. Opt. Eng.: Smart Structures and Materials, Newport Beach, CA, 1999.

[121] K. Naoi, Y. Oura, M. Maeda, and S. Nakamura, "Electrochemistry of surfactant-doped polypyrrole film(I) -- formation of columnar structure by electropolymerization," *J. Electrochem. Soc.*, vol. 142, pp. 417, 1995.

[122] I. W. Hunter and S. Lafontaine, "A comparison of muscle with artificial actuators," presented at IEEE Sol.-Sta. Sen. Act. Workshop, Hilton Head Island, SC, 1992.

[123] S. G. Wax and R. R. Sands, "Electroactive polymer actuators and devices," presented at Proc. SPIE's 6th Int. Symp. Smart Struc. Mater., Electroactive Polymer Actuators and Devices (EAPAD), Newport Beach, CA, 1999.

[124] E. W. H. Jager, E. Smela, O. Inganäs, and I. Lundström, "Applications of polypyrrole microactuators," presented at EAPAD 1999: SPIE's 6th Int. Symp. Smart Struc. Mater., Electroact. Poly. Actu. Dev., Newport Beach, CA, USA, 1999.

[125] A. C. R. Grayson, R. S. Shawgo, A. M. Johnson, N. T. Flynn, Y. Li, M. J. Cima, and R. Langer, "A bioMEMS review: MEMS technology for physiologically integrated devices," *Proc. IEEE*, vol. 92, pp. 6-21, 2004.

[126] B. Eversmann, M. Jenkner, F. Hofmann, C. Paulus, R. Brederlow, B. Holzapfl, P. Fromherz, M. Merz, M. Brenner, M. Schreiter, R. Gabl, K. Plehnert, M. Steinhauser, G. Eckstein, D. Schmitt-Landsiedel, and R. Thewes, "A 128X128 CMOS biosensor array for extracellular recording of neural activity," *IEEE J. Solid-State Cir.*, vol. 38, pp. 2306-2317, 2003.

[127] B. Alberts, D. Bray, A. Johnson, J. Lewis, M. Raff, K. Roberts, and P. Walter, "Introduction to cells," in *Essential Cell Biology*. New York: Garland Publishing, Inc., 1998, pp. 1.

[128] R. R. Harrison and C. Charles, "A low-power low noise CMOS amplifier for

neural recording applications," *IEEE J. Solid-State Cir.*, vol. 38, pp. 958-965, 2003.

[129] N. Reeves, Y. Liu, N. M. Nelson, S. Malhotra, M. Loganathan, J.-M. Lauenstein, J. Chaiyupatumpa, E. Smela, and P. A. Abshire, "Integrated MEMS structures and CMOS circuits for bioelectronic interface with single cells," presented at IEEE ISCAS 2004: Int'l Symp. Cir. Sys., Vancouver, Canada, 2004.

[130] G. T. A. Kovacs, *Micromachined transducers sourcebook.* Boston: WCB McGraw-Hill, 1998.

[131] G. Voskerician, M. S. Shive, R. S. Shawgo, H. v. Recum, J. M. Anderson, M. J. Cima, and R. Langer, "Biocompatibility and biofouling of MEMS drug delivery devices," *Biomater.*, vol. 24, pp. 1959-1967, 2003.

[132] E. Smela and N. Gadegaard, "Volume change in polypyrrole studied by atomic force microscopy," *J. Phys. Chem. B*, vol. 105, pp. 9395-9405, 2001.

[133] M. D. Thouless, "Cracking and delamination of coatings," *J. Vac. Sci. Technol. A*, vol. 9, pp. 2510-2515, 1991.

[134] C. Immerstrand, K. Holmgren-Peterson, K. E. Magnusson, E. Jager, M. Krogh, M. Skoglund, A. Selbing, and O. Inganas, "Conjugated-polymer micro- and milliactuators for biological applications," *MRS Bull.*, vol. 27, pp. 461-464, 2002.

[135] G. G. Wallace, G. M. Spinks, L. A. P. Kane-Maguire, and P. R. Teasdale, "Introduction," in *Conductive electroactive polymers: intelligent materials systems*. Boca Raton, FL, USA: CRC Press LLC, 2003.

[136] E. Smela, G. Zuccarello, H. Kariis, and B. Liedberg, "Thiol modified pyrrole

monomers: 1. Synthesis, characterization, and polymerization of 1-(2-thioethyl)-pyrrole and 3-(2-thioethyl)-pyrrole," *Langmuir*, vol. 14, pp. 2970-2975, 1998.

[137] E. Smela, H. Kariis, Z. Yang, K. Uvdal, G. Zuccarello, and B. Liedberg, "Thiol modified pyrrole monomers: 2. as-deposited monolayers of 1-(2-thioethyl)-pyrrole and 3-(2-thioethyl)-pyrrole," *Langmuir*, vol. 14, pp. 2976-2983, 1998.

[138] E. Smela, H. Kariis, Z. Yang, M. Mecklenburg, and B. Liedberg, "Thiol modified pyrrole monomers: 3. electrochemistry of 1-(2-thioethyl)-pyrrole and 3-(2-thioethyl)-pyrrole monolayers in propylene carbonate," *Langmuir*, vol. 14, pp. 2984-2995, 1998.

[139] E. Smela, "Thiol modified pyrrole monomers: 4. electrochemical deposition of polypyrrole over 1-(2-thioethyl)-pyrrole monolayers," *Langmuir*, vol. 14, pp. 2996-3002, 1998.

[140] D. M. Collard and C. N. Sayre, "Self-assembled monolayers of 3-(ω-mercaptoalkyl)pyrroles on gold," *J. Electroanal. Chem.*, vol. 375, pp. 367-370, 1994.

[141] I. Rubinstein, J. Rishpon, E. Sabatani, A. Redondo, and S. Gottesfeld, "Morphology control in electrochemically grown conducting polymer films. 1. Precoating the metal substrate with an organic monolayer," *J. Am. Chem. Soc.*, vol. 112, pp. 6135-6136, 1990.

[142] R. J. Willicut and R. L. McCarley, "Electrochemically polymerizable self-assembled monolayers," *Adv. Mat.*, vol. 7, pp. 759-762, 1995.

[143] E. P. Plueddemann, "The chemical bonding theory," in *Silane Coupling Agents*.

New York: Plenum Press Inc., 1982, pp. 17.

[144] A. Guiseppi-Elie, A. M. Wilson, J. M. Tour, T. W. Brockmann, P. Zhang, and D. L. Allara, "Specific immobilization of electropolymerized polypyrrole thin films onto interdigitated microsensor electrode arrays," *Langmuir*, vol. 11, pp. 1768-1776, 1995.

[145] ASTM, "D 3359-02: Standard test methods for measuring adhesion by tape test," 2002.

[146] L. W. Crane and C. L. Hamermesh, "Adhesion of thin plasma polymer films to plastics," in *Adhesion Measurement of Thin Films, Thick Films, and Bulk Coatings*, vol. ASTM STP 640, K. L. Mittal, Ed.: America Society for Testing and Materials, 1978, pp. 101.

[147] T. T. Hitch, "Adhesion measurements on thick-film conductors," in *Adhesion Measurement of Thin Films, Thick Films, and Bulk Coatings*, vol. ASTM STP 640, K. L. Mittal, Ed.: America Society for Testing and Materials, 1978, pp. 211.

[148] K. L. Mittal, "Adhesion measurement of thin films," *Electrocomp. Sci. Tech.*, vol. 3, pp. 21-42, 1976.

[149] I. Kondo, O. Takenaka, T. Kamiya, K. Hayakawa, and A. Kinbara, "Adhesion measurement of Ti thin films on Si substrate using internal stress in overcoated Ni films," *J. Vac. Sci. Technol. A*, vol. 12, pp. 169-173, 1994.

[150] Y. Liu, Q. Gan, S. Baig, and E. Smela, "Preventing delamination of conjugated polymers due to electrochemical cycling," *in preparation*, 2005.

[151] G. Mura, M. Vanzi, M. Stangoni, M. Ciappa, and W. Fichtner, "On the behaviour

of the selective iodine-based gold etch for the failure analysis of aged optoelectronic devices," *Microele. Relia.*, vol. 43, pp. 1771-1776, 2003.

[152] M. J. Liew, S. Roy, and K. Scott, "Development of a non-toxic electrolyte for soft gold electrodeposition: an overview of work at Univeristy of Newcastle upon Tyne," *Green Chem.*, vol. 5, pp. 376-381, 2003.

[153] R. J. Morrissey, "A versatile non-cyanide gold plating system," *Plat. Surf. Finish.*, vol. 80, pp. 75-79, 1993.

[154] H. C. Liu and S. P. Murarka, "Elastic and viscoelastic analysis of stress in thin films," *J. Appl. Phys.*, vol. 72, pp. 3458-3463, 1992.

[155] Y. G. Li, W. Chrzanowski, and A. Lasia, "Nucleation and crystal growth in gold electrodeposition from acid solution," *J. Appl. Electrochem.*, vol. 26, pp. 843-852, 1996.

[156] T. Watanabe, "Surface morphology change with increasing film thickness," in *Nano-Plating: Microstructure Control Theory of Plated Film and Data Base of Plated Film Microstructure*. Oxford, UK: Elsevier Ltd., 2004, pp. 14-24.

[157] ASTM, "E 112-96: Standard test methods for determining average grain size (reapproved 2004)," 2004.

[158] J. D. Madden, B. Schmid, M. Hechinger, S. R. Lafontaine, P. G. A. Madden, F. S. Hover, R. Kimball, and I. W. Hunter, "Application of polypyrrole actuators: feasibility of variable camber foils," *IEEE J. Ocean. Eng.*, vol. 29, pp. 738-749, 2004.

[159] E. Smela, Y. Kaminorz, O. Inganäs, and L. Brehmer, "Planar microfabricated

polymer light emitting diodes," *Semicond. Sci. Tech.*, vol. 13, pp. 433, 1998.

[160] A. L. Holt, J. M. Leger, and S. A. Carter, "Solid-state electrochromic devices based on poly (phenylene vinylene) polymers," *Appl. Phys. Lett.*, vol. 86, pp. 123504-123506, 2005.

[161] P. Novak, K. Muller, K. S. V. Santhanam, and O. Haas, "Electrochemically Active Polymers for Rechargeable Batteries," *Chem. Rev.*, vol. 97, pp. 207-281, 1997.

[162] M. Mastragostino, C. Arbizzani, R. Paraventi, and A. Zanelli, "Polymer selection and cell design for electric-vehicle supercapacitors," *J. Electrochem. Soc.*, vol. 147, pp. 407-412, 2000.

[163] P. Soudan, H. A. Ho, L. Breau, and D. Belanger, "Chemical synthesis and electrochemical properties of poly(cyano-substituted-diheteroareneethylene) as conducting polymers for electrochemical supercapacitors," *J. Electrochem. Soc.*, vol. 148, pp. A775-A782, 2001.

[164] S. Timoshenko, "Analysis of bi-metal thermostats," *J. Opt. Soc. Am.*, vol. 11, pp. 233-256, 1925.

[165] Y. Liu, L. Oh, S. Fanning, B. Shapiro, and E. Smela, "Fabrication of folding microstructures actuated by polypyrrole/gold bilayer," presented at Transducers '03: 12th Int'l Conf. Sol. Sta. Sens. Act. Microsys., Boston, MA, USA, 2003.

[166] H. A. Kuhn, "Uniaxial compression testing," in *ASM Handbook: Vol. 8, Mechanical Testing and Evaluation*, H. Kuhn and D. Medlin, Eds. Materials Park, OH: ASM International, 2000, pp. 143.

[167] H. D. Espinosa, B. C. Prorok, and M. Fischer, "A methodology for determining mechanical properties of freestanding thin films and MEMS materials," *J. Mech. Phy. Sol.*, vol. 51, pp. 47-67, 2003.

[168] H. D. Espinosa, B. C. Prorok, and B. Peng, "Plasticity size effects in free-standing submicron polycrystalline FCC films subjected to pure tension," *J. Mech. Phy. Sol.*, vol. 52, pp. 667-689, 2004.

[169] V. K. Pamula, A. Jog, and R. B. Fair, "Mechanical property measurement of thin-film gold using thermally actuated bimetallic cantilever beams," *Nanotech*, vol. 1, pp. 410 - 413, 2001.

[170] E. Smela, "A microfabricated movable electrochromic "pixel" based on polypyrrole," *Adv. Mat.*, vol. 11, pp. 1343-45, 1999.

[171] M. Christophersen, B. Shapiro, and E. Smela, "Characterization and modeling of PPy bilayer microactuators. Part 1: Curvature," *in preparation*, 2005.

[172] C. S. Chen, X. Jiang, and G. M. Whitesides, "Microengineering the environment of mammalian cells in culture," *MRS Bull.*, vol. 30, pp. 194-201, 2005.

[173] S. Fanning, Y. Liu, M. Christophersen, M. Düerkop, and E. Smela, "Polypyrrole/gold bilayer characterization," presented at SPIE's 12th Annual Int'l. Symposium on Smart Structures and Materials, EAPAD, San Diego, CA, 2005.

[174] Aurora, "User's manual of type 406 A force transducer by Aurora Scientific, Inc.," 2003.

[175] G. Lin, R. E. Palmer, K. S. J. Pister, and K. P. Roos, "Miniature heart cell force transducer system implemented in MEMS technology," *IEEE Trans. Biomed.*

Eng., vol. 48, pp. 996-1006, 2001.

[176] G. Lin, K. S. J. Pister, and K. P. Roos, "Surface micromachined polysilicon heart cell force transducer," *J. Microelectromech. Syst.*, vol. 9, pp. 9-17, 2000.

[177] G. Lin, R. E. Palmer, K. S. J. Pister, and K. P. Roos, "Single heart cell force measured in standard CMOS," presented at Transducers '97: 9th Int'l Conf. Sol. Sta. Sens. Act. Microsys., Chicago, IL, USA, 1997.

[178] J. L. Tan, J. Tien, D. M. Pirone, D. S. Gray, K. Bhadriraju, and C. S. Chen, "Cells lying on a bed of microneedles: an approach to isolate mechanical force," *PNAS*, vol. 100, pp. 1484-1489, 2003.

[179] C. G. Galbraith and M. P. Sheetz, "A micromachined device provides a new bend on fibroblast traction forces," *PNAS*, vol. 94, pp. 9114-9118, 1997.

[180] Q. He, E. Meng, Y.-C. Tai, C. M. Rutherglen, J. Erickson, and J. Pine, "Parylene neuro-cage for live neural networks study," presented at Transducers '03: 12th Int'l Conf. Sol. Sta. Sens. Act. Microsys., Boston, MA, USA, 2003.

[181] A. Tooker, E. Meng, J. Erickson, Y.-C. Tai, and J. Pine, "Development of biocompatible parylene neurocages," presented at EMBC 2004: 26th Int'l Conf. IEEE Eng. Med. Bio. Soc., San Francisco, CA, USA, 2004.

[182] Y. Liu, Q. Gan, S. Baig, and E. Smela, "Improving adhesion of polypyrrole on Au for long-term actuation," presented at SPIE's 12th Annual Int'l. Symposium on Smart Structures and Materials, EAPAD, San Diego, CA, 2005.

[183] E. Verpoorte and N. F. D. Rooij, "Microfluidics meets MEMS," *Proc. IEEE*, vol. 91, pp. 930-953, 2003.

[184] J. C. McDonald, D. C. Duffy, J. R. Anderson, D. T. Chiu, H. Wu, O. J. A. Schueller, and G. M. Whitesides, "Fabrication of microfluidic systems in poly(dimethylsiloxane)," *Electrophoresis*, vol. 21, pp. 27-40, 2000.

[185] X. Zhao, Y. Xia, and G. M. Whitesides, "Soft lithographic methods for nano-fabrication," *J. Mater. Chem.*, vol. 7, pp. 1069-1074, 1997.

[186] Y. Xia and G. M. Whitesides, "Soft lithography," *Annu. Rev. Mater. Sci.*, vol. 28, pp. 153-184, 1998.

[187] M. A. Unger, H.-P. Chou, T. Thorsen, A. Scherer, and S. R. Quake, "Monolithic microfabricated valves and pumps by multilayer soft lithography," *Science*, vol. 288, pp. 113-116, 2000.

[188] D. R. Reyes, D. Iossifidis, P.-A. Auroux, and A. Manz, "Micro total analysis systems. 1. introduction, theory, and technology," *Anal. Chem*, vol. 74, pp. 2623-2636, 2002.

[189] P.-A. Auroux, D. Iossifidis, D. R. Reyes, and A. Manz, "Micro total analysis systems. 2. analytical standard operations and applications," *Anal. Chem*, vol. 74, pp. 2637-2652, 2002.

[190] K. Huikko, R. Kostiainen, and T. Kotiaho, "Introduction to micro-analyticalsystems: bioanalytical and pharmaceutical applications," *Eur. J. Pharm. Sci.*, vol. 20, pp. 149-171, 2003.

[191] H. Andersson and A. v. d. Berg, "Microfluidic devices for cellomics: a review," *Sens. Act. B*, vol. 92, pp. 315-325, 2003.

[192] Agilent, "Flow cytometry chip,"

http://www.chem.agilent.com/Scripts/PDS.asp?lPage=3380, 2004.

[193] M. Brischwein, E. R. Motrescu, E. Cabala, A. M. Otto, H. Grothe, and B. Wolf, "Functional cellular assays with multiparametric silicon sensor chips," *Lab Chip*, vol. 3, pp. 234-240, 2003.

[194] M. Lehmann, W. Baumann, M. Brischwein, H. Gahle, I. Freund, R. Ehret, S. Drechsler, H. Palzer, M. Kleintges, U. Sieben, and B. Wolf, "Simultaneous measurement of cellular respiration and acidification with a single CMOS ISFET," *Biosen. Bioelec.*, vol. 16, pp. 195-203, 2001.

[195] D. Beebe, J. Moore, Q. Yu, R. Liu, M. Kraft, B. Jo, and C. Devadoss, "Microfluidic tectonics: a comprehensive construction platform for microfluidic systems," *PNAS*, vol. 97, pp. 13488-13493, 2000.

[196] D. J. Beebe, "Microfabricated fluidic devices for single-cell handling and analysis," in *Emerging Tools for Single-Cell Analysis*, G. Durack and J. P. Robinson, Eds. New York: Wiley-Liss, Inc., 2000, pp. 95-113.

[197] S. Quake, "Biological large scale integration," presented at MicroTAS 2003: 7th Int'l Conf. Mini. Chem. Biochem. Anal. Sys., Squaw Valley, CA, USA, 2003.

[198] T. Thorsen, S. J. Maerkl, and S. R. Quake, "Microfluidic large-scale integration," *Science*, vol. 298, pp. 580-584, 2002.

[199] J. W. Hong and S. R. Quake, "Integrated nanoliter systems," *Nature Biotech.*, vol. 21, pp. 1179-1183, 2003.

[200] J. Liu, C. Hansen, and S. R. Quake, "Solving the "world-to-chip" interface problem with a microfluidic matrix," *Anal. Chem*, vol. 75, pp. 4718-4723, 2003.

[201] M. Okandan, P. Galambos, S. Mani, and J. Jakubczak, "Development of surface micromachining technologies for microfluidics and bioMEMS," presented at SPIE Micromachin. Microfab., San Francisco, CA, USA, 2001.

[202] M. Okandan, C. James, S. S. Mani, and B. L. Draper, "Patch-clamp array with on-chip electronics, optics, flow control and mechanical actuation," presented at MicroTAS 2003: 7th Int'l Conf. Mini. Chem. Biochem. Anal. Sys., Squaw Valley, CA, USA, 2003.

[203] M. Okandan, P. Galambos, S. Mani, and J. Jakubczak, "Surface micromachined cell manipulation device for transfection and sample preparation," presented at MicroTAS 2001: 5th Int'l Conf. Mini. Chem. Biochem. Anal. Sys., Monterey, CA, USA, 2001.

[204] E. Smela, O. Inganäs, and I. Lundström, "Differential adhesion method for microstructure release: an alternative to the sacrificial layer," presented at Transducers '95, Eurosensors IX, Stockholm, Sweden, 1995.

[205] Microchem, "NANO^{TM} SU8 negative tone photoresist formulations 2-25," http://www.microchem.com/products/pdf/SU8_2-25.pdf, 2002.

[206] E. W. H. Jager, E. Smela, O. Inganäs, and I. Lundström, "Polypyrrole microactuators," *Synth. Met.*, vol. 102, pp. 1309-10, 1999.

[207] duPont, "E. I. du Pont de Nemours and Company. General Specification KAPTON® Polyimide Film.," <http://www.kapton-dupont.com/daten2.htm>, 1998.

[208] ASM, "Properties of pure metals," in *Metals Handbook, 9th Ed., Vol.2, Properties*

and Selection: Nonferrous Alloys and Pure Metals. Metals Park, OH, USA: American Society for Metals, 1979, pp. 715.